The Dissertation Committee for Lindsay Erin Pell Certifies that this is the approved version of the following dissertation:

Controlled Synthesis and Characterization of Silicon Nanocrystals

Committee:

Brian A. Korgel, Supervisor

C. Grant Willson

John G. Ekerdt

Paul F. Barbara

Christopher B. Murray

Controlled Synthesis and Characterization of Silicon Nanocrystals

by

Lindsay Erin Pell, B. Ch.E.

Dissertation

Presented to the Faculty of the Graduate School of

The University of Texas at Austin

in Partial Fulfillment

of the Requirements

for the Degree of

Doctor of Philosophy

The University of Texas at Austin

May, 2004

dedicated to my loved ones

Acknowledgements

There are many people who assisted in my graduate experience. First, I would like to thank everyone in the Korgel Group (and its adopted members), especially Tobias Hanrath who provided intellectual assistance as well as much comic relief.

As a member of the Korgel Group during the "early years" I am thankful to the many research groups who shared their time and equipment with me. Those groups include, but are not limited to Dr. Johnston's, Dr. Bard's, Dr. Barbara's, Dr. Willson's and Dr. Koro's. I would specifically like to thank Dr. Bard and Dr. Barbara for our collaborations outside my research group as well as Dr. Murray at IBM who provided me with an educational internship at IBM Yorktown.

One of the more important aspects of nanotechnology research is TEM characterization, and on that note, I would like to thank Dr. Zhou, Dr. Rabenberg and Dr. Mendenhall for their characterization assistance.

I also thank my committee members - Dr. C. Grant Willson, Dr. John G. Ekerdt, Dr. Paul F. Barbara and Dr. Christopher B. Murray for all of their advice and suggestions. And of course, thanks to my advisor, Brian Korgel, who embarked on his journey as a professor shortly before I embarked on mine toward my doctorate degree.

Finally, I received support from my family and friends and especially Sean who expands the frontiers of science everyday.

Controlled Synthesis and Characterization of Silicon Nanocrystals

Publication No._____

Lindsay Erin Pell, Ph.D.

The University of Texas at Austin, 2004

Supervisor: Brian A. Korgel

In response to the demand for shrinking feature sizes and faster electronics, many resources have been dedicated to the research of nanotechnology. At present, silicon is undoubtedly the building block and key to the microelectronics world. In its bulk form, silicon is an inefficient emitter in the infrared, but as its dimensions shrink to the nanoscale, silicon exhibits unique optical and electrical properties such as size tunable photoluminescence. The more successful methods of the synthesis of silicon nanocrystals include laser ablation and silane pyrolysis; however these methods offer little in the way of particle stabilization which would prevent oxidation and allow for manipulation through dispersion in organic solvents.

A novel supercritical fluid synthesis is investigated with respect to various silicon precursors such as diphenylsilane, silicon tetrachloride and trisilane. The electrochemical and luminescent properties of silicon nanocrystals, synthesized via the thermal decomposition of diphenylsilane, were studied. Differential pulse voltammetry of silicon nanocrystals in DMF and acetonitrile exhibit quantized double layer charging as previously reported for Au and CdS nanocrystals. Additionally, electron transfer reactions between positively and negatively charged nanocrystals (or between charged nanocrystals and molecular redox-active coreactants) occurred that led to electron and hole annihilation, producing visible light. The electrogenerated chemiluminescence spectra exhibited a peak red shifted from the photoluminescence maximum.

Single nanocrystal photoluminescence was investigated via Argon laser excitation and confocal microscopy. The single nanocrystals demonstrate stochastic single-step "blinking" behavior and size-dependent PL spectra with line widths approximately only three times greater than those measured for CdSe nanocrystals at room temperature.

Investigation of trisilane as a viable silicon precursor in a supercritical fluid synthesis led to the formation of well formed, sub-micron, amorphous silicon colloids in high yield. Manipulation of temperature, pressure and precursor concentration allowed for the synthesis of amorphous silicon particles 60-400 nm in diameter. Polydisperse samples exhibited two dimensional, long-

range orientational order in the absence of translational order which has been compared to the Reverse Brazil Nut Effect. Additionally, metal induced crystallization was observed in amorphous silicon particles annealed in a vacuum evaporator.

Table of Contents

List of Tables

List of Figures

Chapter 1: Introduction

1.1 Nanocrystal Background

1.1.1 Nanocrystal Properties

Metals and semiconductors in the nanometer size range may exhibit different properties, electrical and optical, than those found on a molecular scale or in the bulk. These properties are strongly coupled to the size of the nanocrystal.[1] In reference to semiconductor materials, one such property that changes with size is the band gap. As the dimensions shrink to the nanoscale in a semiconductor material its band gap increases relative to the band gap of the bulk material. This effect has been measured experimentally[2] and can be modeled theoretically by taking into account the Coulombic attraction of the electron-hole pair and modeling the nanocrystal/electron-hole pair as a particle in a box.[3]

1.1.2 Nanocrystal Formation and Stabilization

Often nanocrystals are manipulated either as powders or in solution. Colloidal suspensions of nanocrystals are possible through the steric stabilization of the surface nanocrystal atoms using a variety of organic molecules such as long chain thiols, alcohols, acids and oxides. Such stabilizers (capping ligands) must be present during the growth of the nanocrystals to prevent aggregation and precipitation while in solution. Capping ligands not only serve as stabilizers but

can help control the growth of the nanocrystals and in semiconductors the ligands can passivate surface electronic states through binding or adsorption to the nanocrystal surface. Appropriate choice of stabilizers allows suspension of nanocrystals in organic or aqueous solvents and helps determine the solubility of the nanocrystals in solution.[1] Figure 1.1 depicts a Si nanocrystal, showing various capping ligand molecules.

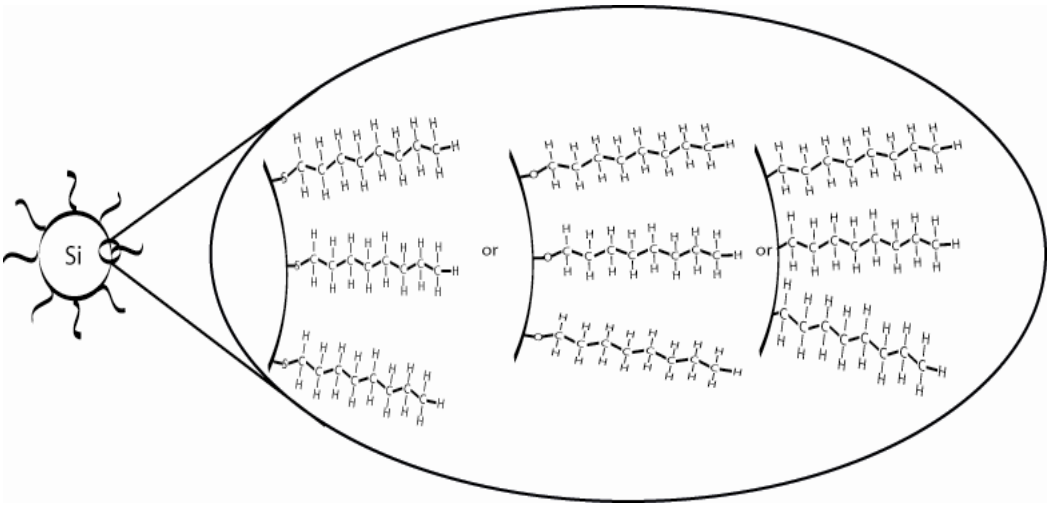

Figure 1.1 Diagram of a single Si nanocrystal depicting the different types of steric stabilizers (octane thiol, octanol, octene) employed to cap the particle.

It is advantageous, but often difficult to synthesize size monodisperse nanocrystals for use in self assembled structures. After much study, controlled benchtop syntheses of nanocrystals has been achieved for such systems as Co[4], CdSe[5,6] and CdS;[7] however, such improvements have not been accomplished in all metal and semiconductor systems. In lieu of a direct synthesis of size monodisperse crystals, there are several methods employed to separate

polydisperse samples of crystals into fractions of monodisperse crystals. One such popular method is size selective precipitation; this method involves the slow titration of antisolvent into a nanocrystal solution. Aggregation of the larger nanocrystals occurs first as they have the greatest van der Waals forces. If partial flocculation is permitted followed by centrifugation, the large particles will precipitate out of solution, separating themselves from the smaller nanocrystals. Alternating titration and centrifugation will produce size monodisperse fractions of nanocrystals.[1]

Nanocrystal synthesis is performed in many ways including two phase arrested development, laser ablation, simple reduction chemistry or thermal decomposition.[8-11] Synthesis of some nanocrystals requires special consideration. For the case of silicon certain precursors are air or moisture sensitive (silicon halides and silanes); therefore; syntheses must be carried out in a controlled inert gas environment.

1.1.3 Nanocrystal Superlattices

As the body of research in the nanotechnology field has increased exponentially over the past decade[§] the ability to synthesize nanocrystals is no longer novel. Rather there is greater emphasis on the ability to synthesize monodisperse particles for their collective characterization and application as

[§] A literature search produced 91 "nanocrystal" articles published in 1990, 1214 articles in 1995 and 3688 articles in 2002.

monolayers and superlattices as shown in Figure 1.2. Metal and semiconductor nanocrystals are being incorporated in light emitting devices, nanotransistors and chemical catalysts. Arrangement of nanocrystals into monolayers or superlattices is directed by spontaneous positioning or self-assembly.

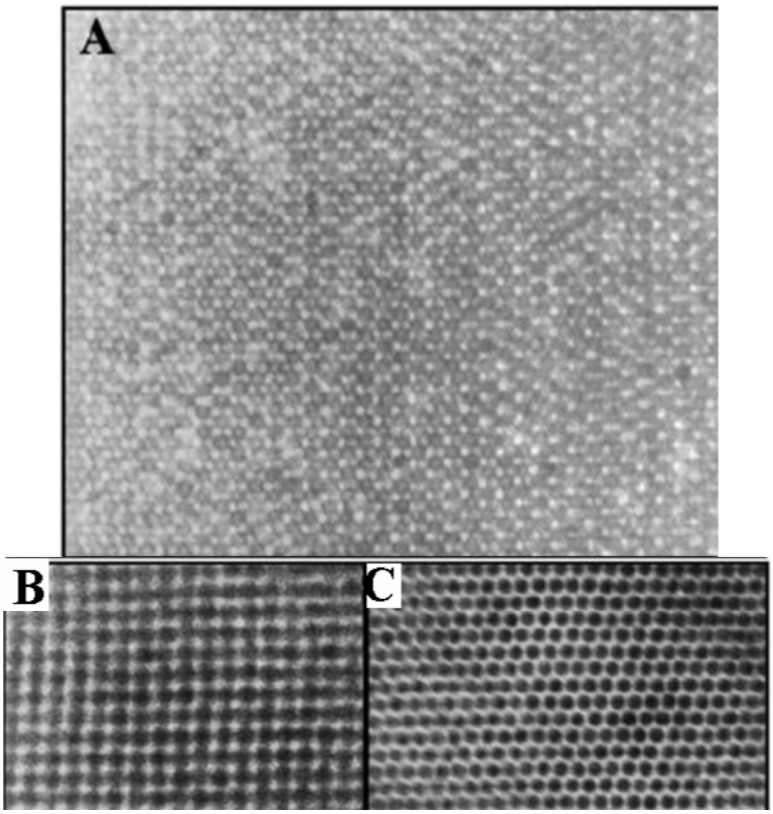

Figure 1.2 (A) and (B) TEM images of a three-dimensional superlattice of 48 Å CdSe nanocrystals; (C) TEM image of an fcc superlattice of 64 Å CdSe nanocrystals.[1]

The packing of the nanocrystals is affected by the core and capping material as well as the superlattice preparation. Narrow size distributions ($\sigma \leq$

5%)[1] and weakly interacting particles are essential for self assembly into superlattices.[12] Lattice formations comprised of covalently bound particles (bound through their ligands) form irreversible cross-linkages which are more stable than the lattices formed through weak dispersion attractions; however, the covalently bound lattices do not achieve long range order.[12] Gold nanocrystal passivation using thiols of varying chain lengths has been investigated experimentally as well as through simulation. Experimentally, gold nanocrystals were stabilized with thiol molecules containing 3 to 24 carbon atoms. The shorter chain thiols resulted in disordered lattices while the longer chain thiols resulted in ordered superlattice structures.[13] Simulations of gold nanocrystal superlattices have shown how the ligand length affects ordering. Short chain thiols result in bcc structures while longer chain thiols resulted in fcc structures.[14]

Preparation of a good superlattice is usually achieved by slow solvent evaporation of monodisperse particles onto a substrate. The particles need sufficient time to diffuse to the growing surface; however, if too many particles are simultaneously available for deposition then an amorphous solid is formed. In the case of CdSe a superlattice formation has been demonstrated by evaporating from a solvent solution comprised of 95% octane and 5% octanol. Octane solvates the particles, but as it evaporates, increasing the octanol concentration, the particle dispersion becomes unstable and the CdSe nanocrystals slowly precipitate to the surface.[1]

1.1.4 Colloidal Crystals

Long range ordering of superlattices (on the micron scale) result in colloidal crystals which homogeneously nucleate in solution.[1] One sought after application of colloidal crystals is the formation of a 3D photonic crystal. A true photonic crystal would mean obtaining a complete photonic band gap, allowing for the manipulation of light through the inhibition of unwanted emission. It has been and continues to be experimentally challenging to make a 3D photonic crystal as there are several criteria to be filled. The material must have a band gap in the optical wavelengths, a refractive index greater than 2.8 and the structure must be ~ 80% porous. Semiconductor materials such as GaP, GaAs, InP, Si and Ge show promise in this application as they have high refractive indexes and on the nanoscale they emit at optical wavelengths. However, close packing of nanoscale semiconductors will not achieve the required porosity.[15]

In order to make use of the favorable semiconductor properties, opals are often used as a template for colloidal crystals. Monodisperse submicron particles of polystyrene or silica are deposited to form a colloidal crystal. Semiconductor material is inserted into the template (in the interstitial spaces of the opals) via nanocrystal sintering, electrodeposition or chemical vapor deposition. Once the semiconductor is deposited, the opals are removed from the template by etching, thus leaving holes behind giving the new structure the desired porosity. While

advances have been made in this area, there are still issues to be addressed in order to achieve good deposition of the semiconductor.[15]

1.1.5 Polydisperse Ordering

A large body of theoretical research has been conducted by Stephenson *et al.* in the area of circle packing which is defined as a configuration of circles having a prescribed pattern of tangencies.[16-20] Monodisperse as well as polydisperse groupings of circles have been investigated under myriad conditions. Of particular interest to experimentalists is the regular 7-degree (heptagonal) circle packing illustrated in Figure 1.3. This particular packing is infinite but hyperbolic.[18]

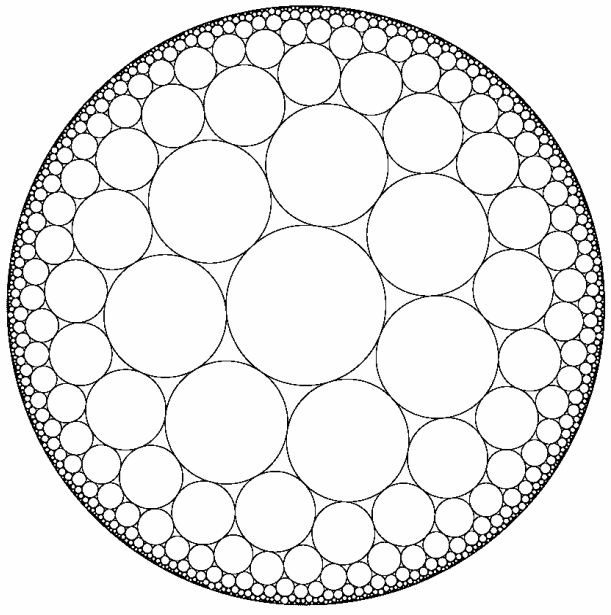

Figure 1.3 Heptagonal infinite circle packing.[18]

These two dimensional simulations are wonderful comparisons to transmission electron microscope images of nanocrystals. There has been little experimental work published on these structures where the larger particles (circles) are concentrated in the center of the formation while the smaller particles (circles) which are in abundance, surround the larger core. Such structures are referred to as "Zenon" clusters and their deposition has been demonstrated through the slow evaporation of polydisperse polystyrene microgels (5-50 nm) in a toluene solution. Quenched hexagonal arrangements are formed where the degree of hyperbolic distortion is directly coupled to the polydispersity.[21]

Such formations have also been shown to occur in gold nanocrystals. The "Zenon" cluster formation process is driven by interparticle attractions. The van der Waals forces dominate over the entropic effects but are small enough to allow these equilibrium configurations during solvent evaporation. Examining the van der Waals attractions as:

$$V(D) = \frac{A}{6}\left[\frac{2R_AR_B}{D^2 + 2D(R_A + R_B)} + \frac{2R_AR_B}{D^2 + 2D(R_A + R_B) + 4R_AR_B} + \ln\left(\frac{D^2 + 2D(R_A + R_B)}{D^2 + 2D(R_A + R_B) + 4R_AR_B}\right)\right] \quad (1.1)$$

where A is the Hamaker constant, R_A and R_B are the radii of hard spheres and D is the distance of closest approach. At D << R the attractions become linear (-AR/D) with respect to particle radius. At D >> R the attractions are 6^{th} power dependent on particle radius ($-AR_A^2R_B^2/D^6$). These interactions account for the cluster formation where the larger particles are more strongly attracted and form

the center of the sphere. The next tier of smaller particles "wet" the cluster formed by the larger particles rather than forming their own cluster, and the "Zenon" cluster grows.[22] From this early work, long range ordering of polydisperse samples should be possible.

1.2 Supercritical Fluids

Research into the uses of supercritical fluids (SCFs) has been driven on many fronts from extraction and separation[23-26] to dyeing of synthetic materials.[27] The properties of SCFs which make them desirable over traditional solvents include high compressibility near the critical point and viscosity and diffusivity that are gas and liquid-like. The former causes significant density changes with minor temperature and pressure adjustment affecting solubility, while the latter properties increase reaction rates that are diffusion limited in the liquid regime.[28]

Carbon dioxide and water are the most commonly used SCFs due to their relative non-flammability, non-toxicity and abundance.[28] In recent years, use of SCFs has expanded to include synthesis and dispersion of nanocrystal systems in this media. Supercritical water has demonstrated to be a favorable media for the formation of copper and copper oxide nanocrystals of various morphologies.[29] Gold and silver nanocrystals (with the appropriate stabilizers) can be synthesized in SC ethane and size selected by density tuning.[30] Silver, iridium and platinum nanocrystal systems can be synthesized (and growth mechanism studied at low temperatures) in SC carbon dioxide.[31,32] Less utilized supercritical solvents such

as acetone and hexane have been used to synthesize nanocrystals and nanowires. Supercritical fluid reprecipitation in acetone yields 50 nm titanyl phthalocyanine and 40 nm carbon nanocrystals.[33] Supercritical hexane is the media used to synthesize Si and Ge nanowires by the SFLS (supercritical fluid-liquid-solid) method.[8,34] Use of supercritical fluids in the nano-sciences is certain to increase just as the research in nano-sciences has accelerated.

1.3 Electron Transport

1.3.1 Electrochemistry

Electrochemical behavior given by current-potential curves from cyclic voltammetry (CV) and differential pulse voltammetry (DPV) of metallic NCs have previously been studied and show quantized double layer charging effects (also known as Coulomb blockade or quantized capacitance charging).[35,36] Electrochemical quantized capacitance charging occurs when particle molecules behave as diffusive nanoelectrodes in solution and the discrete charging to the particle double layer results in the appearance of electrochemical analogues of Coulomb staircase charging.[37] CV and DPV experiments have been preformed on organically stabilized gold nanocrystals at platinum electrodes. The larger nanocrystals (d = 1.9 nm) exhibited double layer capacitive charging while the smaller NCs (d = 1.1 nm) exhibited molecular redox-like behavior.[38]

To date, little attention has been focused on the electrochemical responses of semiconductor nanocrystals. CV measurements on PbS nanoparticles seemingly exhibited Coulomb blockade behavior, but on further inspection it was determined that the peaks in question corresponded to cathodic reduction reactions of PbS nanoparticles and anodic stripping of surface accumulated lead.[37] Had the nanoparticles benn more stable in solution, irreversible quantized double layer charging would be expected. CdS NCs provide a more stable solution for electrochemical studies. CV measurements on a CdS NC solution result in oxidation and reduction peaks corresponding to electron transfer at the HOMO and LUMO, respectively. Additionally, it is qualitatively verified that the optical band gap is a function of particle size; the CV peak separations decrease with increasing particle size.[39] As capping chemistry of nanocrystals improves to create more stable solutions, electrochemical measurements of nanocrystals will diversify to include many metallic and semiconductor systems.

1.3.2 Electrogenerated Chemiluminescence

Electrogenerated chemiluminescence (ECL) has been used to study the nature and mechanism of an emitting state, electron transfer theory and the mechanism of organic reactions involving radicals.[40-42] A review of electrogenerated chemiluminescence involving nanocrystals resulted in a surprisingly small body of work. Mallouk *et al*. report electrogenerated chemiluminescence from self-assembled diode junctions prepared from ruthenium

tris(bipyridyl) [$Ru(bpy)_3$)] polymer, n-type TiO_2 nanoparticles and graphite oxide sheets. Although it is unconventional to refer to ECL in a film, in this case there is a charge recombination reaction between Ru^{III} and $Ru^{I}[Ru(bpy)_3)]$ centers resulting in ECL due to emissive metal-to-ligand charge transfer excited state of the RuII form is generated within the film.[43]

ECL from nanocrystals in solution requires reactants to be energetic enough to generate light and also be moderately stable. Compound semiconductor NCs are typically chemically unstable upon electron transfer, but ECL has recently been reported by Bard *et al.* for CdSe nanocrystals. Electrogenerated chemiluminescence was induced when excited states occurred through electron transfer annihilation of electrogenerated anion and cation radicals:

$$R^{\cdot -} + R^{\cdot +} \rightarrow R^* + R \qquad (1.2)$$

$$R^* \rightarrow R + \eta\nu \qquad (1.3)$$

The anion and cation radicals are electrogenerated at the platinum surface. The resulting ECL spectrum was sufficiently red-shifted compared to the photoluminescence spectrum which suggests that surface states were the predominant factor of emission. Use of CdSe NCs in a core/shell system would decrease/eliminate the surface and ECL could be measured solely from the core of the nanocrystal.[44]

1.4 Single Nanocrystal Spectroscopy

With the technological improvements in optical spectroscopy, single molecule spectroscopy has been made possible. Interesting properties can be explored on this level such as the lifetime dependence on spectral shift and dipole orientation as well as the frequency dependence of spontaneous emission.[45] It follows that there would be interest in the study of single nanocrystals as many interesting properties can be observed on an individual level which are obscured by particle ensembles such as spectral diffusion, fluorescence intermittency, photobleaching effects.[46] Single nanocrystal spectroscopy experiments have been reported for such compound semiconductor systems as InP[47] and CdSe[48-50] as well as the core/shell systems CdSe/CdS[51] and CdSe/ZnS.[46]

Typical single nanocrystal optical measurements were made using a scanning confocal microscope and laser excitation of the sample.[46] Dilute solutions of nanocrystals (and polymer) were deposited on a slip cover via drop casting or spin-coating.[50] Optical measurements revealed spectral diffusion in single nanocrystals depicted in Figure 1.4. The photoluminescence spectra blue shifts with increasing excitation time. Such diffusion is attributed to the irreversible photooxidation of the nanocrystal.[46]

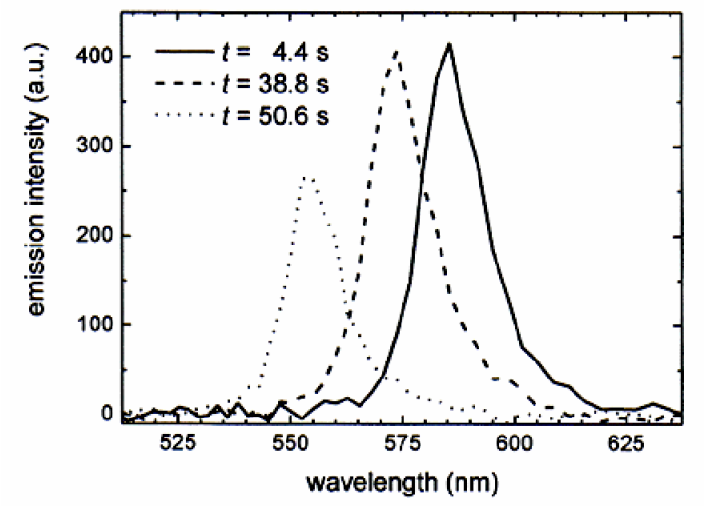

Figure 1.4 Spectral diffusion of a single CdSe/ZnS nanocrystal. Photoluminescence emission measured after different lengths of laser excitation.[46]

Fluorescence intermittency is another property exhibited by nanocrystals which can only be measured on an individual nanocrystal basis. Fluorescence intermittency can be observed when the emission spectrum of a single nanocrystal is punctuated with periods of "darkness" and periods of "brightness" (also referred to as on/off states). Figure 1.5 illustrates the phenomena for a single nanocrystal by plotting the emission intensity vs. time. Initially the nanocrystal is not emitting light ("dark") when the laser is off; when the laser is turned on, the nanocrystal emits light of an arbitrary intensity and is said to be in an "on" state or in a period of brightness. While the laser still excites the nanocrystal, it may go into an "off" or "dark" state for a period of time before emitting again. This cycle continues until the nanocrystal photobleaches.[49]

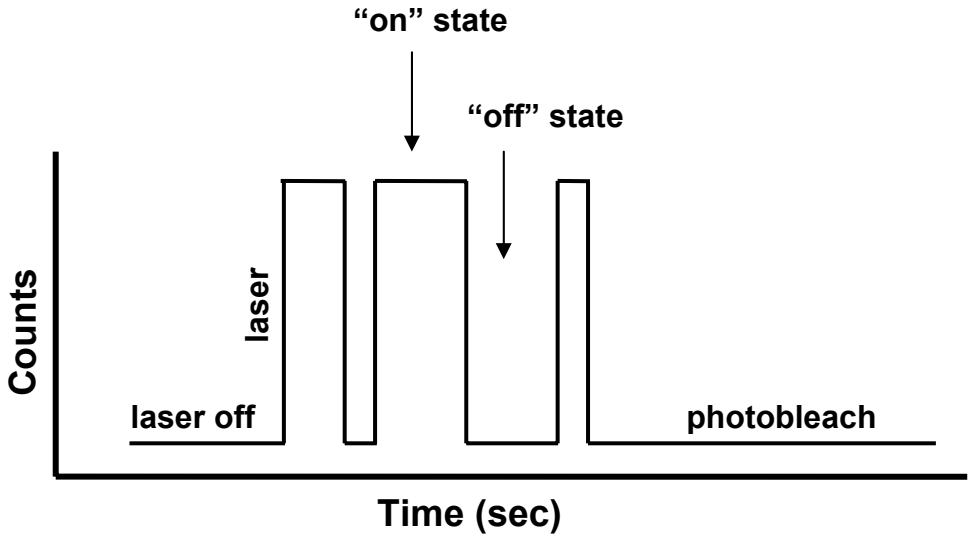

Figure 1.5 Illustration of fluorescence intermittency in a single nanocrystal via intensity vs. time curve.

The “on” states in this spectrum are the result of radiative recombinations of electron-hole pairs, while the “off” states are the result of non-radiative electron-hole pair recombinations. Figure 1.6 illustrates the radiative recombination of an electron-hole pair as well as two possible non-radiative recombination routes: thermally activated trapping and Auger photoionization. Thermally activated trapped, exhibited in Figure 1.6B, can lead to excess charge in traps on the surface of the particle. In the Auger process a photon is absorbed by the nanocrystal and before it can radiative recombine another photon is absorbed. One electron hole pair recombines but instead of emitting light the energy produced leads to the ejection of charge outside the nanocrystal. The light emission is quenched in the two aforementioned processes making them non-radiative recombinations. Single

nanocrystal spectroscopy of II-VI and III-V semiconductors has been well reported while group IV semiconductor reports are still lacking.

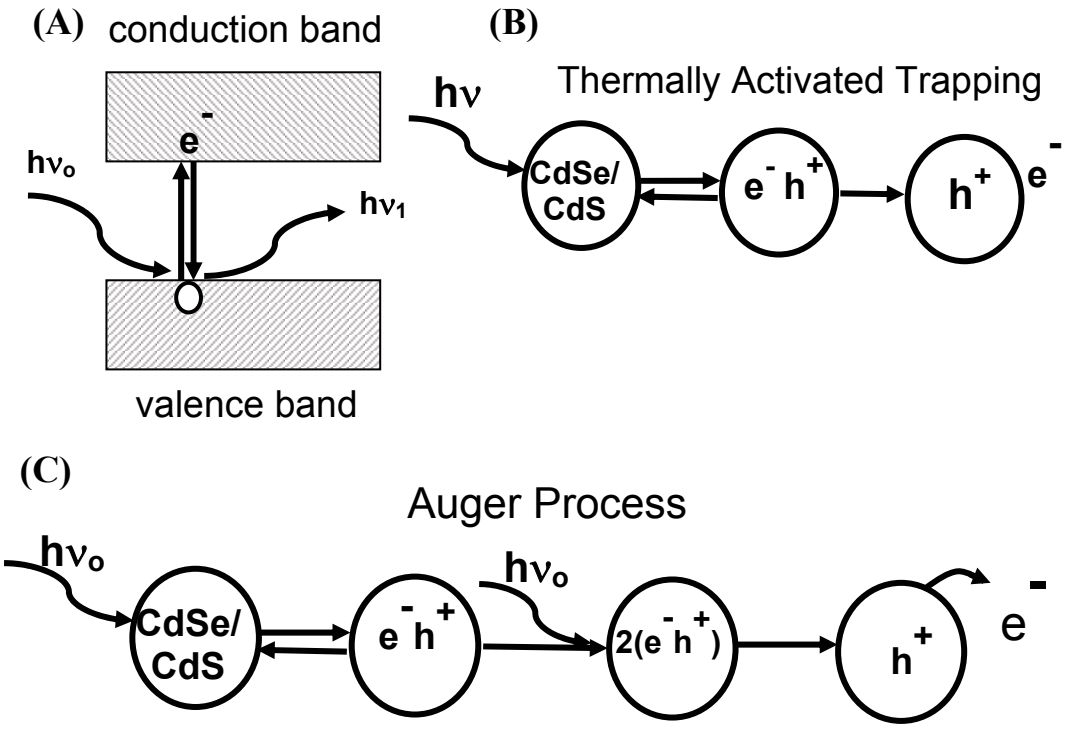

Figure 1.6 Illustration of radiative recombination of an electron-hole pair (A) and non-radiative recombination via thermally activated trapping (B) and Auger photoionization (C).[51]

1.5 Current Work and Organization of Dissertation

Interest in nanocrystal (NC) synthesis and characterization has increased tremendously during the past decade. Size monodisperse nanocrystals have many applications; the biotechnology and semiconductor industries are two areas interested in the electronic and size-tunable optical properties of nanostructures. Nanocrystal properties are correlated to their size. For example, quantum confinement effects change such properties as excitation and luminescence energies.

Silicon is arguably the most important material in the microelectronics industry. It is the substrate material of choice for fabrication of integrated circuits over germanium and gallium arsenide. Silicon has better hole mobility, good stability during thermal processing, it easily forms an insulating oxide, it is relatively inexpensive and has low defect densities[52]. Quantum confined silicon can be even more interesting because of its added optical properties. It is the goal of this project to understand the physical properties of nanostructured silicon through the study of nanocrystals 2-10 nm in size and the study of submicron crystals annealed from amorphous silicon lattices. Better understanding of the size control and surface chemistry are also necessary. The key to this study lies in understanding of the synthesis of silicon nanoparticles. The successes and challenges of silicon chemistry are discussed in Chapter 2 which details the work

completed on the synthesis of silicon nanocrystals (2-10 nm) from a variety of organic precursors.

In collaboration with Dr. Bard *et al*. at the University of Texas at Austin, Department of Chemistry and Biochemistry the electrochemical behavior of silicon NCs has been investigated in this work. As semiconductor nanocrystals have received little attention[53,54] and silicon NCs none in this regard there was interest in whether silicon would behave like metal NCs. Secondly, electrogenerated chemiluminescence (ECL) was measured and compared to photoluminescence of the Si NCs. Electrochemical behavior of silicon nanocrystals is reported in Chapter 3.

Single nanocrystal spectroscopy was completed in collaboration with Dr. Paul Barbara *et al*. at the University of Texas at Austin, Department of Chemistry and Biochemistry and the Center for Nano and Molecular Science and Technology. Single nanocrystal isolation was achieved by spin coating an extremely dilute solution of Si nanocrystals, dispersed in chloroform, on glass microscope slip covers. Single nanocrystal luminescence measurements were completed using scanning confocal microscopy and an Argon ion continuous wave laser (488, 514 or 543 nm excitation). The results of single silicon nanocrystal spectroscopy are reported in Chapter 4.

Submicron silicon crystals were formed via annealing of amorphous silicon particles in the size range of 60-400 nm. Amorphous silicon particles can be

synthesized in high yield via the degradation of trisilane in supercritical hexane. Trisilane forms thermodynamically stable amorphous silicon spheres that do not require any steric stabilization against agglomeration. Control of synthesis conditions allows for the formation of various sizes of particles with varying degrees of polydispersity. A design of experiments illustrates that the most favorable conditions for particle growth are high temperature, moderately high pressure, low concentration and a slow temperature ramp. Steric stabilization of the amorphous particles is also possible (*in situ* or post synthesis) and allows for enhanced control over the size distribution. Upon annealing, amorphous silicon yields highly crystalline submicron particles having 20 nm domains. The synthesis of amorphous silicon as well as its evolution to crystalline submicron particles is detailed in Chapter 5.

Another interesting aspect of the amorphous silicon is its ability to form self assembled, polydisperse, organized lattices. Amorphous particles of the appropriate polydispersity and concentration will form ordered arrays such that the larger particles form the center of the array in a hexagonal close packed pattern and the smaller particles "wet" the inner particles causing the array to grow. Such formations contain as few as 100 particles or over 1000 particles where the hexagonal packing is preserved over the majority of the structure. This polydisperse ordering is addressed in Chapter 6.

Chapter 7 briefly summarizes the research addressed in the dissertation and also provides suggestions for future work in the area of organically soluble nanoscale silicon.

1.6 References

(1) Murray, C. B.; Kagan, C. R.; Bawendi, M. G. *Annual Review of Materials Science* **2000**, *30*, Future.

(2) Vossmeyer, T.; Katsikas, L.; Giersig, M.; Popovic, I. G.; Diesner, K.; Chemseddine, A.; Eychmuller, A.; Weller, H. *The Journal of Physical Chemistry* **1994**, *98*, 7665-7673.

(3) Pell, L. E. "Quantum Confinement in Nanomaterials Explored Via Particle in a Box Theory," University of Texas at Austin, 2002.

(4) Sun, S. H.; Murray, C. B. *J. Appl. Phys.* **1999**, *85*, 4325-4330.

(5) Peng, Z. A.; X., P. *Journal of the American Chemical Society* **2001**, *123*, 1389-1395.

(6) Peng, Z. A.; Peng, X. G. *Journal of the American Chemical Society* **2002**, *124*, 3343-3353.

(7) Korgel, B. A.; Monbouquette, H. G. *J. Phys. Chem.* **1996**, *100*, 346-351.

(8) Lu, X.; Hanrath, T.; Johnston, K. P.; Korgel, B. A. *Nano Lett.* **2003**, *3*, 93-99.

(9) Brust, M.; Fink, J.; Bethell, D.; Shiffrin, D. J.; Kiely, C. *Journal of Chemistry Society, Chemical Communications* **1995**, 1655.

(10) Morales, A. M.; Lieber, C. M. *Science* **2000**, *279*, 5348.

(11) Yang, C.-S.; Bley, R. A.; Kauzlarich, S. M.; Lee, H. W. H.; Delgado, G. R. *Journal of the American Chemical Society* **1999**, *121*, 5191-5195.

(12) Collier, C. P.; Vossmeyer, T.; Heath, J. R. *Annual Review of Physical Chemistry* **1998**, *49*, 371-404.

(13) Hostetler, M. J.; Stokes, J. J.; Murray, R. W. *Langmuir* **1996**, *12*, 3604-3612.

(14) Luedtke, W. D.; Landman, U. *J. Phys. Chem.* **1996**, *100*, 13323-13329.

(15) Norris, D. J.; Vlasov, Y. A. *Advanced Materials* **2001**, *13*, 371-376.

(16) Beardon, A. F.; Stephenson, K. *Indiana Univ. Math. J.* **1990**, *39*, 1383-1425.

(17) Bowers, P. L.; Stephenson, K. *Math. Proc. Camb. Philos. Soc.* **1992**, *111*, 487-513.

(18) Dubejko, T.; Stephenson, K. In *Experimental Mathematics*; Jones and Bartlett Publishers: Boston, 1995; Vol. 4, pp 307-348.

(19) Dubejko, T.; Stephenson, K. *Mich. Math. J.* **1995**, *42*, 211-234.

(20) Collins, C. R.; Stephenson, K. *Comput. Geom.-Theory Appl.* **2003**, *25*, 233-256.

(21) Antonietti, M.; Hartmann, J.; Neese, M.; Seifert, U. *Langmuir* **2000**, *16*, 7634-7639.

(22) Ohara, P. C.; Leff, D. V.; Heath, J. R.; Gelbart, W. M. *Phys. Rev. Lett.* **1995**, *75*, 3466-3469.

(23) Santa-Maria Blanco, G.; Reglero Rada, G.; Tabera Galvan, J.; Blanch Manzano, G. P.; Pastor Pastor, J. In *Span.*; (Consejo Superior de Investigaciones Cientificas, Spain). Es, 2001, p 6 pp.

(24) Yang, S. *Zhongguo Zhongyao Zazhi* **2001**, *26*, 755-757.

(25) Lang, Q.; Cheng, I. F.; Wai, C. M.; Paszczynski, A.; Crawford, R. L.; Barnes, B.; Anderson, T. J.; Wells, R.; Corti, G.; Allenbach, L.; Erwin, D. P.; Assefi, T.; Mojarradi, M. *Analytical Biochemistry* **2002**, *301*, 225-234.

(26) Johannsen, M. *Journal of Chromatography, A* **2001**, *937*, 135-138.

(27) Knittel, D.; Saus, W.; Schollmeyer, E. *J. Text. Inst.* **1993**, *84*, 534-552.

(28) Savage, P. E.; Gopalan, S.; Mizan, T. I.; Martino, C. J.; Brock, E. E. *AIChE J.* **1995**, *41*, 1723-1778.

(29) Ziegler, K. J.; Doty, R. C.; Johnston, K. P.; Korgel, B. A. *Journal of the American Chemical Society* **2001**, *123*, 7797-7803.

(30) Shah, P. S.; Holmes, J. D.; Johnston, K. P.; Korgel, B. A. *Journal of Physical Chemistry B* **2002**, *106*, 2545-2551.

(31) Shah, P. S.; Husain, S.; Johnston, K. P.; Korgel, B. A. *Journal of Physical Chemistry B* **2001**, *105*, 9433-9440.

(32) Shah, P. S.; Husain, S.; Johnston, K. P.; Korgel, B. A. *Journal of Physical Chemistry B* **2002**, *106*, 12178-12185.

(33) Kasai, H.; Komai, Y.; Okazaki, S.; Okada, S.; Oikawa, H.; Adschiri, T.; Arai, K.; Nakanishi, H. *Kobunshi Ronbunshu* **2001**, *58*, 650-660.

(34) Hanrath, T.; Korgel, B. A. *Advanced Materials (Weinheim, Germany)* **2003**, *15*, 437-440.

(35) Chen, S.; Ingram, R. S.; Hostetler, M. J.; Pietron, J. J.; Murray, R. W.; Schaaff, T. G.; Khoury, J. T.; Alvarez, M. M.; Whetten, R. L. *Science* **1998**, *280*, 2098.

(36) Chen, S.; Murray, R. W.; Feldberg, S. W. *Journal of Physical Chemistry B* **1998**, *102*, 9898-9907.

(37) Chen, S. W.; Truax, L. A.; Sommers, J. M. *Chemistry of Materials* **2000**, *12*, 3864-3870.

(38) Chen, S. W.; Ingram, R. S.; Hostetler, M. J.; Pietron, J. J.; Murray, R. W.; Schaaff, T. G.; Khoury, J. T.; Alvarez, M. M.; Whetten, R. L. *Science* **1998**, *280*, 2098-2101.

(39) Haram, S. K.; Quinn, B. M.; Bard, A. J. *Journal of the American Chemical Society* **2001**, *123*, 8860-8861.

(40) Faulkner, L. R.; Bard, A. J. *Electroanalytical Chemistry*; Marcel Dekker: New York, 1977; Vol. 10.

(41) Faulkner, L. R.; Bard, A. J. In *Electroanalytical Chemistry*; Rubenstein, I., Ed.; Marcel Dekker: New York, 1998; Vol. 20, pp 1-95.

(42) Bard, A. J.; Debad, J. D.; Leland, J. K.; Sigal, G. B.; Wilbur, J. L.; Wohlstadter, J. N. In *Encyclopedia of Analytical Chemistry: Applications,*

Theory and Instrumentation; Meyers, R. A., Ed.; John Wiley & Sons: New York, 2000; Vol. 11, p 9842.

(43) Cassagneau, T.; Fendler, J. H.; Johnson, S. A.; Mallouk, T. E. *Advanced Materials (Weinheim, Germany)* **2000**, *12*, 1363-1366.

(44) Myung, N.; Ding, Z.; Bard, A. J. *Nano Letters* **2002**, *2*, 1315-1319.

(45) Macklin, J. J.; Trautman, J. K.; Harris, T. D.; Brus, L. E. *Science* **1996**, *272*, 255-258.

(46) van Sark, W.; Frederix, P.; Van den Heuvel, D. J.; Gerritsen, H. C.; Bol, A. A.; van Lingen, J. N. J.; Donega, C. D.; Meijerink, A. *Journal of Physical Chemistry B* **2001**, *105*, 8281-8284.

(47) Kuno, M.; Fromm, D. P.; Gallagher, A.; Nesbitt, D. J.; Micic, O. I.; Nozik, A. J. *Nano Lett.* **2001**, *1*, 557-564.

(48) Kuno, M.; Fromm, D. P.; Hamann, H. F.; Gallagher, A.; Nesbitt, D. J. *Journal of Chemical Physics* **2001**, *115*, 1028.

(49) Shimizu, K. T.; Neuhausser, R. G.; Leatherdale, C. A.; Empedocles, S. A.; Woo, W. K.; Bawendi, M. G. *Physical Review B* **2001**, *63*, 205316.

(50) Nirmal, M.; Dabbousi, B. O.; Bawendi, M. G.; Macklin, J. J.; Trautman, J. K.; Harris, T. D.; Brus, L. E. *Nature* **1996**, *383*, 802-804.

(51) Banin, U.; Bruchez, M.; Alivisatos, A. P.; Ha, T.; Weiss, S.; Chemla, D. S. *Journal of Chemical Physics* **1999**, *110*, 1195-1201.

(52) Campbell, S. A. *The Science and Engineering of Microelectronic Fabrication*; 2nd ed.; Oxford University Press, Inc.: New York, 2001.

(53) Chen, S.; Truax, L. A.; Sommers, J. M. *Chemistry of Materials* **2000**, *12*, 3864-3870.

(54) Haram, S., K.; Quinn, B. M.; Bard, A. J. *Journal of the American Chemical Society* **2001**, *123*, 8860-8861.

Chapter 2: Exploration of Various Silicon Precursors in Silicon Nanocrystal Synthesis

2.1 Silicon Nanocrystal Synthesis

2.1.1 Supercritical Fluid Synthesis Apparati

2.1.1.1 Supercritical Fluid Batch Reactor

Initial reactor designs for the supercritical decomposition of silicon precursors involved a simple batch reactor made of titanium (grade 2) or stainless steel. The reactors were designed to have a 10 mL inner volume with one closed end and one open end to be closed with a plug and gland as shown in Figure 2.1. The reactor could be mounted to a Unistrut frame and wrapped with high temperature heating tape and insulation to achieve temperatures up to 600°C. Temperature was controlled to $\pm$0.2°C using a thermocouple inserted into the wall of the reactor and an Omega temperature controller.

2.1.1.2 Supercritical Fluid Injection Apparatus

The 10 mL cylindrical titanium vessel described above was modified to be sealed with a reducer and a 3-way valve for semi-batch injection reactions as shown in Figure 2.2. High temperature heating tape for metal surfaces was still

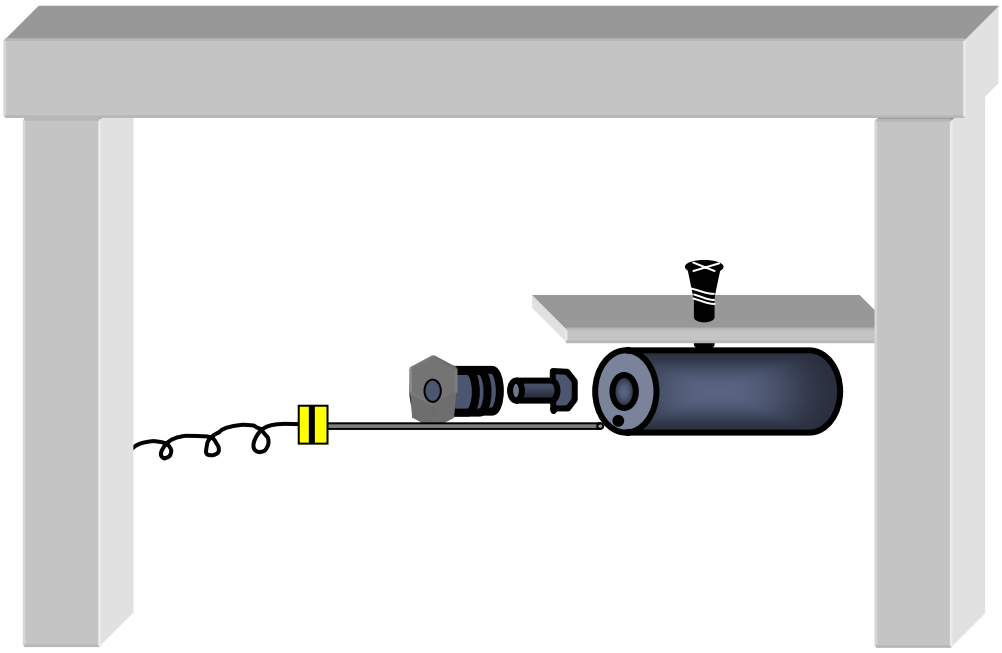

Figure 2.1 Batch reactor design, screw mounted to Unistrut assembly with thermocouple temperature monitoring and control.

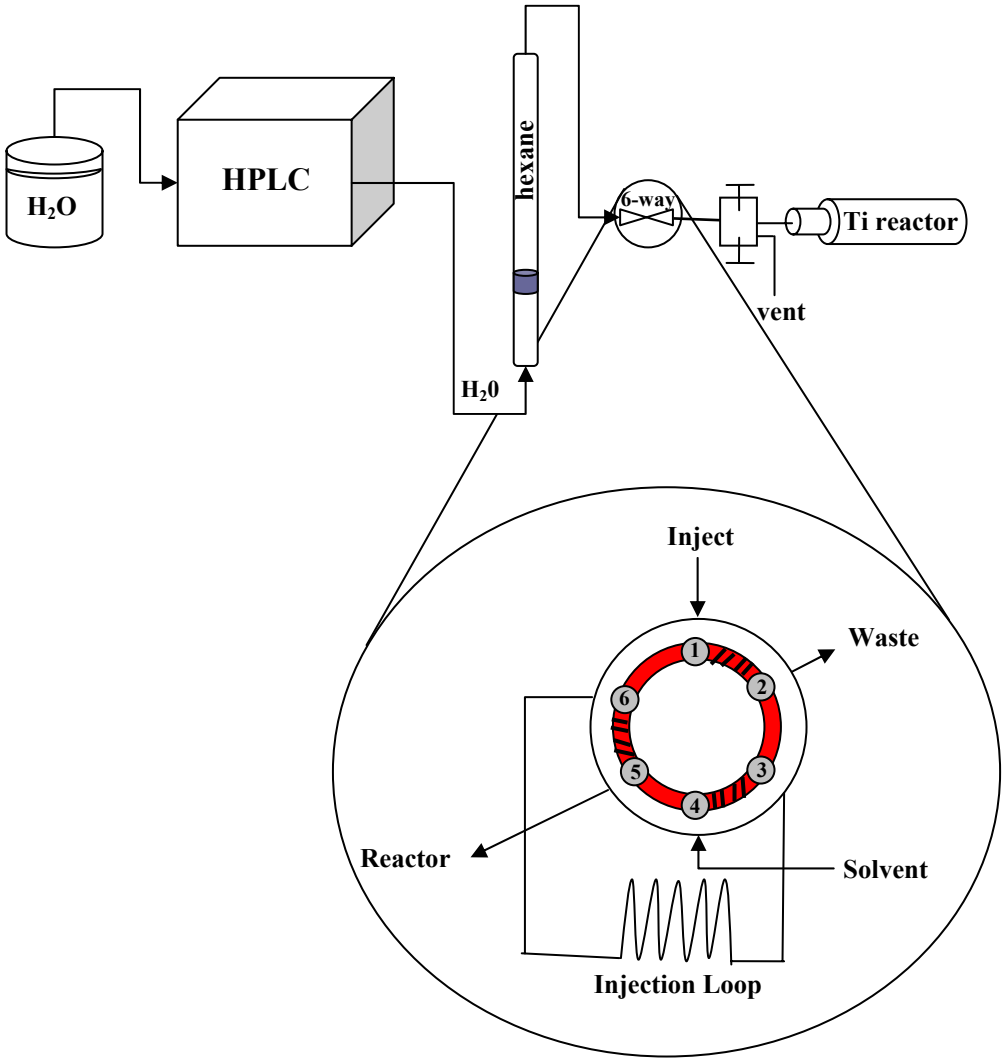

Figure 2.2 Diagram of semi-batch injection apparatus for supercritical synthesis nanocrystals.

used to heat the reactor and the temperature still controlled by an Omega temperature controller and thermocouple. Once the reactor reached the desired temperature, the 3-way valve was opened to the solvent line and the pressure was verified to be above the supercritical point (> 600 psi). Reaction pressure can be increased as needed and precursor solution injected by the solvent delivery system. A high pressure, stainless steel tube fitted with a piston coupled with an HPLC pump serves as the solvent delivery system. The HPLC pump delivers water into the back end of the tube driving the piston upward and delivering the solvent on the top side of the piston to the reactor. The precursor solution is simultaneously injected into the reactor via the 6-way valve during pressurization/solvent delivery. After precursor injection and the reaction pressure is reached, the 3-way valve is closed and the reaction was allowed to proceed for a period of time. The insulation and heating tape were removed as quickly as possible and the reactor was submerged in a water bath to cool, depressurize and quench the nanocrystal growth.

2.1.1.3 Brass Block Heater Modification to Apparatus

The brass block heating modification was implemented in an effort to decrease solvent decomposition and speed the preheating process. Under the aforementioned semi-batch process the reactor is filled with solvent while in the glove box then attached to the experimental apparatus for heating. The high temperature heating tape used on the titanium reactor takes approximately 1 hour

to heat the reactor to 500°C, allowing for solvent decomposition. Heating of the reactor to 500°C in a matter of minutes is possible using the brass block heaters shown in Figure 2.3. Essentially 2 brass blocks have a hollowed out region in the center to fit the reactor. The blocks are housed in custom designed, insulated, aluminum boxes, open at the top, that when fit together encase the reactor. The brass blocks will be preheated by 4 omega cartridge heaters such that the reactor is introduced when the block is 75°C above the desired reaction temperature. The reactor quickly heats up to the desired temperature and the block temperature decrease down to the reaction temperature. The solvent delivery and precursor injection aspects of the apparatus are the same as described in the semi-batch injection process.

2.1.2 Generic Description of Supercritical Fluid Synthesis

For the purposes of this section the reagent will generically be referred as the silicon precursor. Multiple silicon precursors will be discussed in later sections of Chapter 2. Although many silicon precursors are commercially available that can be used in a thermal decomposition to yield nanocrystals, most of these precursors decompose at elevated temperatures (above 350°C.[1-7]) Temperatures high enough to decompose these precursors are achievable at atmospheric pressure with high boiling point solvents such as squalane, trioctylamine, octyl ether or trioctylphosphine oxide; however, the boiling point of preferable capping ligands falls below the optimum reaction temperature.

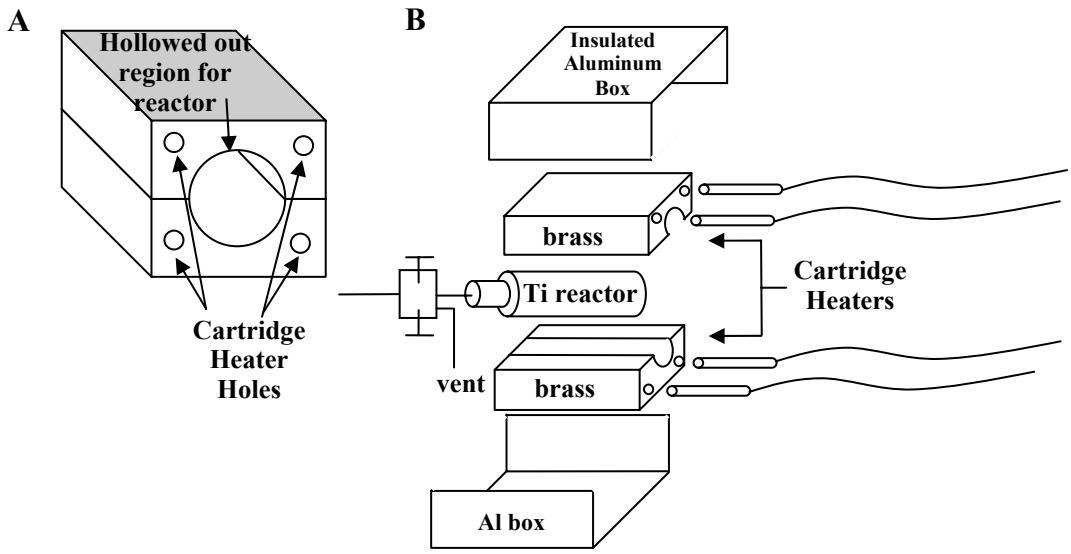

Figure 2.3 (A) Design for brass block heater. (B) Implementation of brass block heater into experimental setup.

Evaporation or decomposition of the certain capping ligands prevents synthesis of silicon nanocrystals (via thermal decomposition) in a wet chemistry or benchtop apparatus. Also it is difficult to separate silicon nanocrystals from high boiling point solvents as the crystals have an affinity for most organic solvents making precipitation difficult. Such experiments have been attempted but have failed to yield recoverable silicon nanocrystals. In addition to the precipitation and capping ligand issues, high temperature benchtop syntheses are undesirable due to the evaporation of silicon intermediates (such as silane) during the decomposition process. Carrying out the synthesis in supercritical anhydrous hexane under nitrogen allows for the degradation of silicon precursors and stabilization of the silicon nanocrystals before exposure to the environment.

All chemicals were either purchased as anhydrous or degassed via a freeze-pump-thaw method and stored in a nitrogen glove box. The method described below is for the injection method. The uncapped titanium reactor was loaded into the glove box, filled with ~3-4 mL of hexane and then sealed with the reducer and 3-way valve. A syringe was filled with a dilute solution (15 - 200 mM) of silicon precursor and capping ligand in hexane. The concentration of the organic ligand varies with different experiments from a 1:1 to a 1:10,000 molar ratio with the silicon precursor. The reactor and syringe were removed from the glove box and the reactor was attached to the experimental apparatus depicted in Figure 2.2. The reactor was heated by one of two methods, heating tape or brass

block, and allowed to heat up to reaction temperature (400 - 550°C). Once the reactor reached the desired temperature, the 3-way valve was opened to the solvent line, the precursor solution in the syringe was injected into the reactor via the 6-way valve and pressure in the reactor elevated to the desired point by back pressurizing with solvent using an HPLC pump. Once the reaction pressure (2000-6000 psi) was reached, the 3-way valve was closed and the reaction was allowed to proceed for a period of time (10-30 minutes). Post reaction, the reactor was submerged in a water bath to cool, depressurize and quench the nanocrystal growth. The contents were extracted and prepared for analysis.

2.2 Silicon Precursors

2.2.1 Decomposition Mechanism for Arylsilanes

The silicon precursor initially used in the synthesis was diphenylsilane (DPS) which undergoes a thermal decomposition to yield silicon atoms that are free to bond to one another forming silicon nanocrystals. Aerospace Research Laboratories (Coutant and Levy)[2,7] conducted a study in the late 1960's looking in to the stability and thermal decomposition of selected phenylsilanes. The results of this research have served as the guide for determination of the mechanism for silicon nanocrystal formation. There are a few notable differences between the aforementioned reaction conditions and those detailed in the Aerospace report; Coutant and Levy run the decomposition at temperatures between 350 and 425°C

and pressures much closer to atmospheric. There are several mechanisms that have been considered and some rejected. The decomposition of mono-, di-, and triphenylsilanes proceed via second-order bimolecular reactions:

$$2\phi_n SiH_{4-n} \rightarrow \phi_{n-1}SiH_{5-n} + \phi_{n+1}SiH_{3-n} \quad (2.1)$$

Tetraphenylsilane, with a reaction order best represented as 3/2, decomposes via a free radical type mechanism

$$\phi_4Si \rightarrow A + B \quad (2.2)$$

$$\phi_4Si + B \rightarrow \text{products} \quad (2.3)$$

where the main products are hydrogen, benzene, triphenylsilane, and ortho-, meta- and para-biphenylyltriphenylsilane.[2,7] Applying this information to the synthesis, one proposed mechanism for the silicon nanocrystal formation is:

$$2\phi_2SiH_2 \rightarrow \phi SiH_3 + \phi_3SiH \quad (2.4)$$

$$2\phi_3SiH \rightarrow \phi_2SiH_2 + \phi_4Si \quad (2.5)$$

$$\phi_4Si \rightarrow \text{free radicals} \rightarrow \text{Si dots} + \text{byproduct} \quad (2.6)$$

Experimentally, tetraphenylsilane production is observed from diphenylsilane but no decomposition. This was further investigated by attempting to form silicon nanocrystals directly from the decomposition of tetraphenylsilane in the same reaction conditions used with diphenylsilane. In this case no reaction takes place and the conclusion is that tetraphenylsilane is very stable and does not decompose in supercritical solvents. The next mechanism investigated was:

$$2\phi_2SiH_2 \rightarrow \phi SiH_3 + \phi_3SiH \quad (2.7)$$

$$2\phi_3SiH \rightarrow \phi_2SiH_2 + \phi_4Si \quad (2.8)$$

$$\phi SiH_3 \rightarrow \text{free radicals} \rightarrow \text{Si dots} + \text{byproduct} \quad (2.9)$$

where monophenylsilane theoretically decomposes to silicon and byproducts. Coutant and Levy's contention that monophenylsilane follows the decomposition detailed in Equation 2.1 is not in agreement with their observation that no benzene, hydrogen or silane is formed from the decomposition[2,7] In addition to this discrepancy, experimental observations led to the conclusion that the second proposed mechanism is also incorrect. It has been observed that drastically decreasing the initial concentration of diphenylsilane prevents the formation of tetraphenylsilane (because of the reduced bimolecular reactions) but does not prevent the formation of silicon nanocrystals. Based on the aforementioned observations, the current hypothesis for the mechanism of silicon nanocrystal formation is:

$$2\phi_2SiH_2 \rightarrow \text{free radicals} \rightarrow \text{Si dots} + \text{byproduct} \quad (2.10)$$

By reducing or eliminating the bimolecular interactions there is a drastic reduction in the formation of the phenylsilanes. The working hypothesis is that the diphenylsilane molecules break apart when injected (at ambient conditions) into the supercritical fluid freeing up silicon for the formation of nanocrystals. The silicon atoms may not completely dissociate from the hydrogen and phenyl groups and these groups may in fact help stabilize the particles in solution.[8]

The diphenylsilane decomposition reaction is concentration limited by the formation of tetraphenylsilane; therefore, monophenylsilane was investigated as a silicon precursor. If one assumes that monophenylsilane undergoes a bimolecular reaction, as described above, there is a possible 75% conversion to silane, a much greater yield than with diphenylsilane, which makes it an attractive precursor. Additionally, silane will thermally decompose to silicon under the supercritical reaction conditions.

Monophenylsilane (MPS) disproportionation reactions in the presence of alkoxides, alkyl compounds, amides or hydrides of alkali metals have been shown to increase the MPS conversion. Products of the disproportionation reaction are silane gas, di-,tri- and tetraphenylsilane. Arylsilane production can be limited by the choice of catalyst.[9,10] Disproportionation of MPS in supercritical hexane increased MPS conversion to silicon product (up to 40%); however, 80% of the silicon yield are poorly formed, micron sized, amorphous silicon particles. The potentially useful silicon nanocrystals are in solution with the substantial byproducts of the disproportionation reaction. The nanocrystal products of the MPS and DPS reactions face the same challenges; they are highly soluble in organic solvents; therefore, causing an inability to adequately clean the nanocrystal product.[11] While arylsilanes have succeeded as precursors in the synthesis of silicon nanocrystals, they have not proved to be advantageous with regard to yield and byproduct removal.

2.2.2 Characterization of Nanocrystals Synthesized from Diphenylsilane

Silicon NCs synthesized by the injection method described above have been characterized by UV-vis absorbance, photoluminescence (PL), photoluminescence excitation (PLE) and high resolution transmission electron microscopy (TEM). A 27 mM DPS and 27 mM octanol solution was injected into a high pressure reactor. The 25 minute reaction occurred at 450°C and 3000 psi to produce Sample A. Typical absorbance, PL and PLE spectra are shown in Figure 2.4.

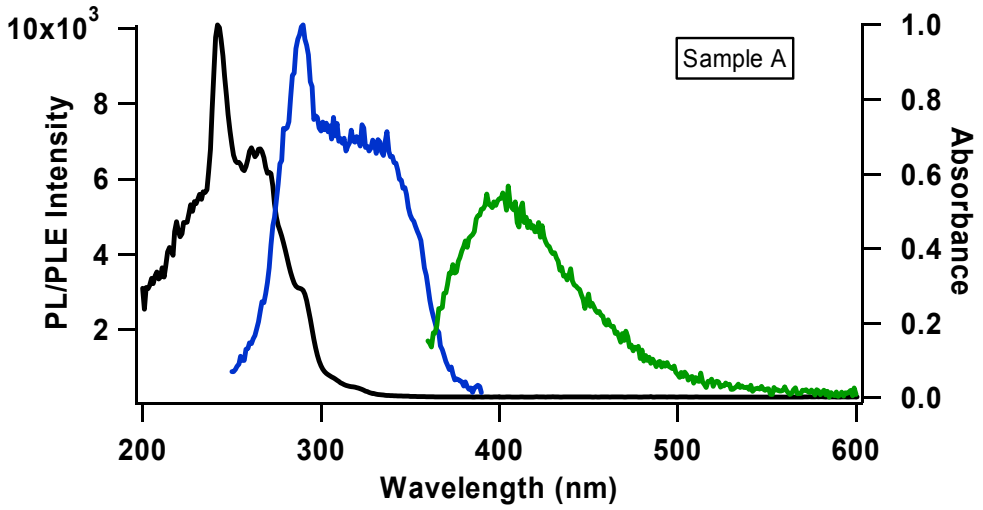

Figure 2.4 Absorbance (black), PL (green, λ_{ex} = 350 nm) and PLE (blue, λ_{em} = 400 nm) spectra of Si NCs synthesized at 450°C for 25 minutes and stabilized with octanol.

The broad, single band photoluminescence curve is typical of silicon nanocrystals, especially polydisperse samples. The photoluminescence excitation spectra should overlap the absorbance spectra for all luminescent species. This is

the case for the peak under 300 nm on each spectrum which is from a luminescent molecular species, unseparated from the Si NCs. The broad section of the PLE curve from ~300-350 nm overlaps the absorbance curve in the same region and this can be attributed to the nanocrystal emission. The peaks below ~290 nm on the absorbance spectra are nonluminescent species (hence their absence in the PLE spectra) which are byproducts/unreacted precursor from the DPS decomposition.

Photoluminescence peak positions are expected to shift blue or red with decreasing or increasing crystal size, respectively. This is demonstrated in Figure 2.5 with two Si NC samples of varying dispersity and size.

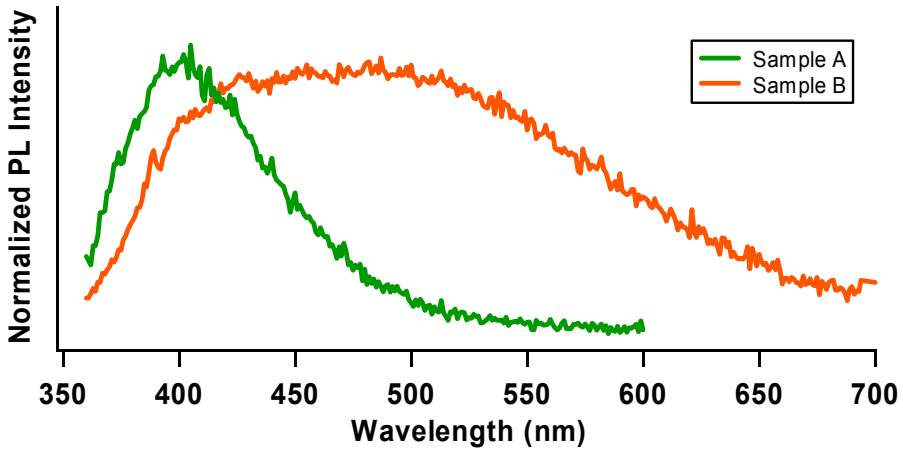

Figure 2.5 PL spectra of two Si NC samples of different sizes excited at 350 nm.

Sample B is a polydisperse sample, with crystal sizes of 4.6 $\pm$ 1.5 nm, which luminesces over a broad range of the visible spectrum. This sample was

synthesized in a batch reactor at 500°C, 1200 psi for 30 minutes from a 250 mM DPS and 25 mM octanethiol solution in hexane. Comparing the PL spectra of the samples, one would expect Sample A to be a less polydisperse sample of smaller sized crystals. This happens to be the case as Sample A is made up of ~ 2 $\pm$ 0.8 nm nanocrystals. Crystal sizes have been estimated using a Phillips 208 100kV transmission electron microscope for high contrast.

High resolution images have been obtained on a JEOL 2010 200kV TEM. Examples of octanol capped silicon nanocrystals are shown in Figure 2.6. Lattice resolution can be seen in the single crystal on the right, in the (220) orientation.

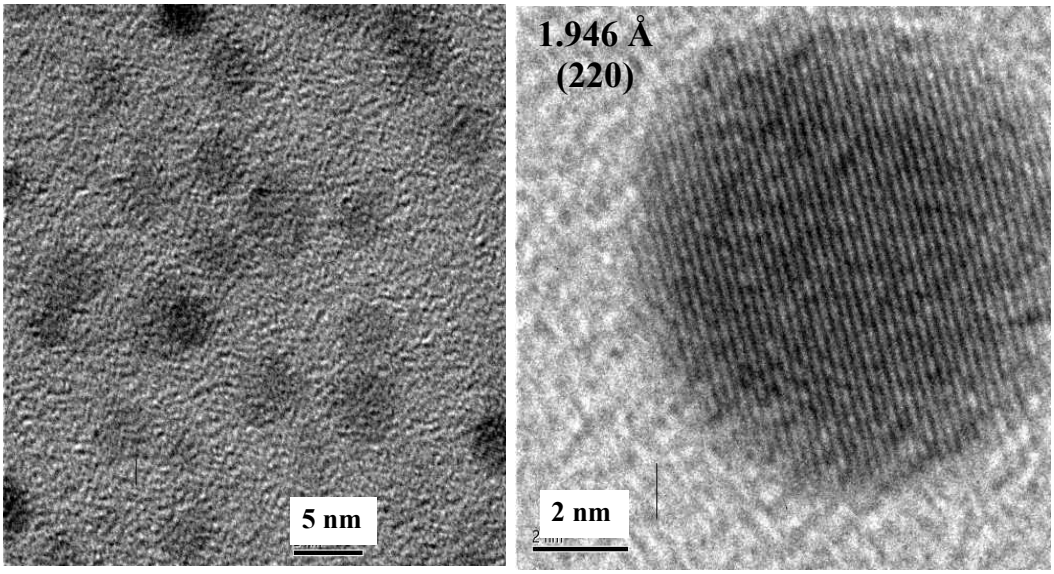

Figure 2.6 HRTEM image of Si NCs capped with octanol.

2.2.3 Decomposition Mechanism of Silicon Halides

In an effort to decrease byproduct formation and solvent decomposition and increase yield, silicon tetrachloride and silicon tetrabromide were examined as possible precursors for silicon nanocrystal growth in supercritical fluids. These precursors react similarly and yield essentially identical results; therefore, this section will deal the mechanism and products from the use of silicon tetrachloride. Three reactions were investigated and presented below using the reagents silicon tetrachloride, lithium aluminum hydride, lithium hydride and sodium borohydride.

$$SiCl_4 + LiAlH_4 \rightarrow SiH_4(g) + LiCl(s) + AlCl_3(s) \quad (2.11)$$

$$SiCl_4 + 4LiH \rightarrow SiH_4(g) + 4LiCl(s) \quad (2.12)$$

$$SiCl_4 + NaBH_4 \rightarrow SiH_4(g) + NaCl(s) + BCl_3(s) \quad (2.13)$$

$$SiH_4(g) \xrightarrow[\Delta]{} Si(s) + 2H_2(g) \quad (2.14)$$

The metathesis reactions 2.11-2.13 each result in the *in situ* formation of silane which decomposes to silicon under the supercritical reaction conditions. Additionally, a reaction of $SiCl_4$ with sodium metal to produce bulk silicon was also investigated. Batch reactions were carried out where the precursors and solvent were sealed in the reactor while inside the nitrogen glove box. No stearic stabilizers were used in the initial reactions as the goal was to form bulk, crystalline silicon in high yield.

2.2.4 Silicon Halide Reaction Products and Characterization

Batch reactions of $SiCl_4$ (0.87 M) with stoichiometric amounts of $LiAlH_4$, LiH, $NaBH_4$ or Na were carried out at temperatures above 350°C, pressures of ~5000 psi and time greater than 10 minutes. The reactions were quenched by the submersion of reactor in a water or ice bath. After cooling, the reactor contents were extracted and washed with water to remove the salt byproduct. The product was then filtered to recover any silicon product. Reactions of $SiCl_4$ with LiH, $NaBH_4$ or Na all resulted in a similar product of amorphous silicon as evidenced by X-ray diffraction and TEM in Figure 2.7. Only the reaction of $SiCl_4$ with $LiAlH_4$ resulted in bulk crystalline silicon formation as shown by Figure 2.8 which is consistent with the concept that aluminum aids in the crystallization of silicon.[12-15]

Once the silicon halide – lithium aluminum hydride combination were identified as promising precursors in a nanocrystal synthesis, the aforementioned batch reaction was repeated with the addition of a stabilizer such as a long chain alcohol or thiol. However, this reaction did not produce nanocrystals as desired; the yield was again bulk, crystalline silicon. A semi-batch injection reaction was completed next; a hexane solution of 120 mM $SiBr_4$ and 0.02 mM octanol was injected into a reactor at 450°C, pressurized to 5400 psi and reacted for 10 minutes. After cooling the product was extracted and washed with water.

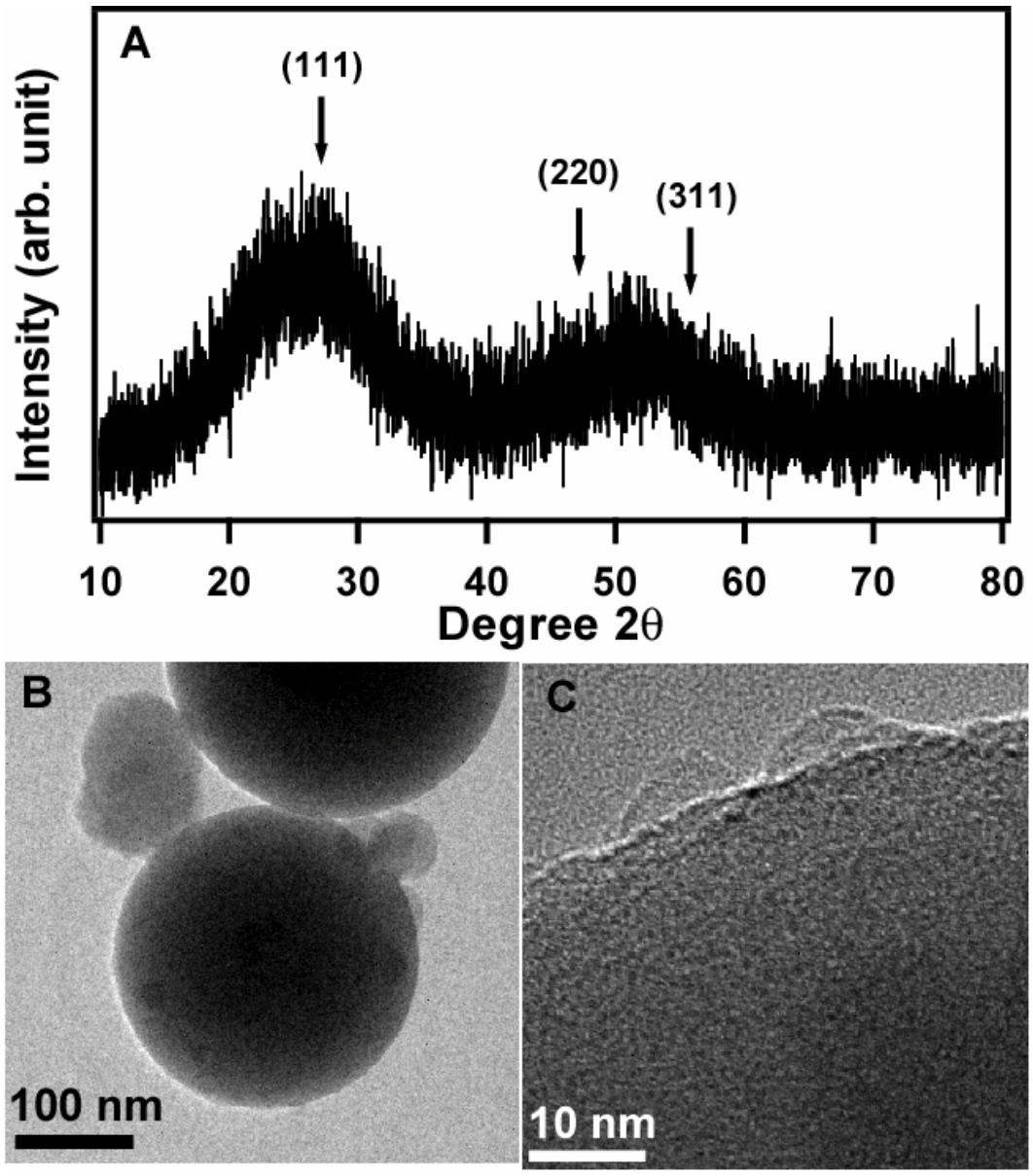

Figure 2.7 (A) XRD of amorphous silicon formed by reaction of $SiCl_4$ and sodium metal. The wide peak of Si (111) is visible and the compilation of Si (220) and (311) which forms a single broad peak. (B) and (C) are high resolution TEM images of amorphous silicon formed from the reaction of $SiCl_4$ and LiH.

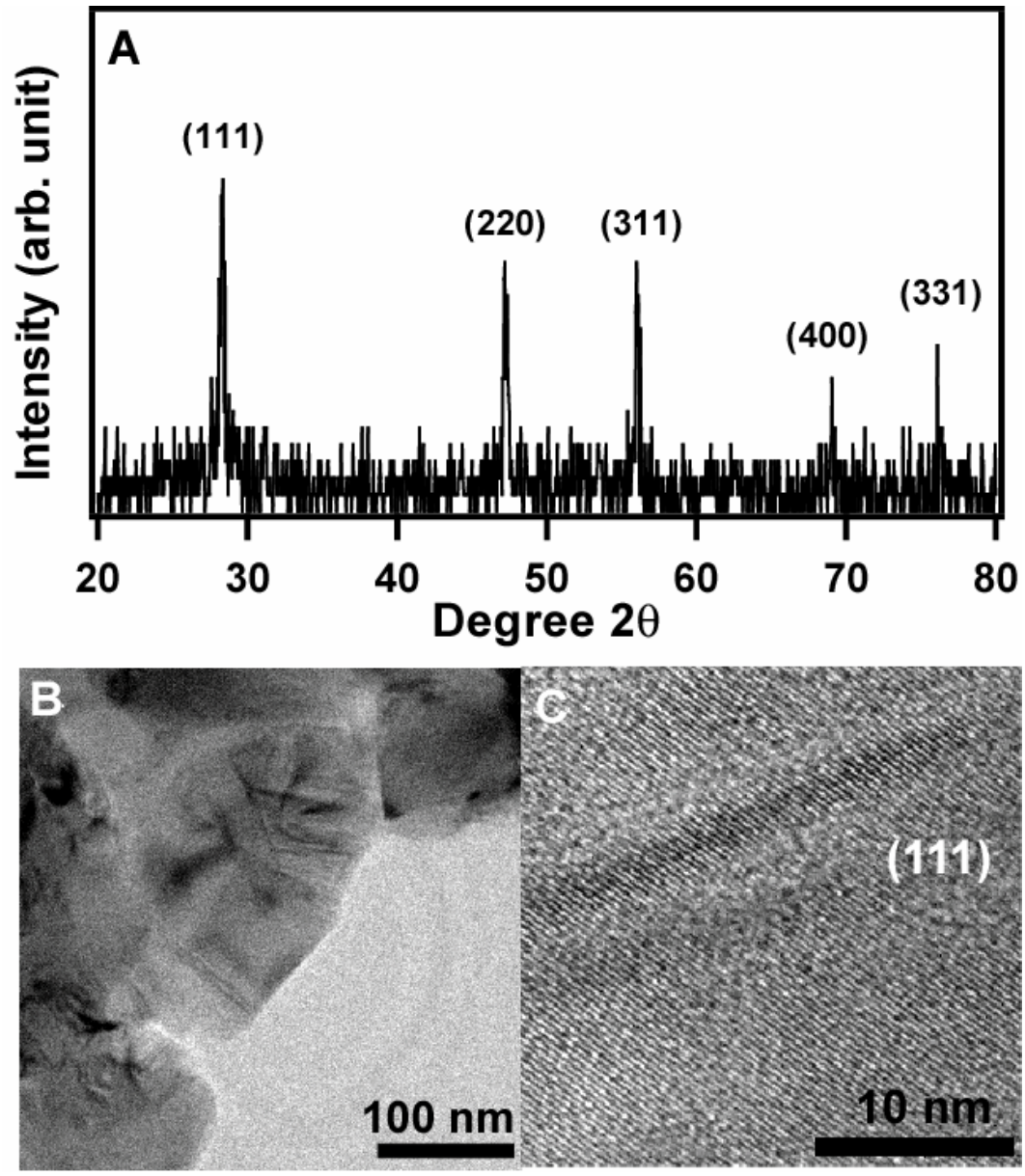

Figure 2.8 (A) XRD of bulk, crystalline silicon formed from the reaction of $SiCl_4$ and $LiAlH_4$. (B) and (C) High resolution TEM images of crystalline silicon; lattice fringes for Si (111) shown in (C).

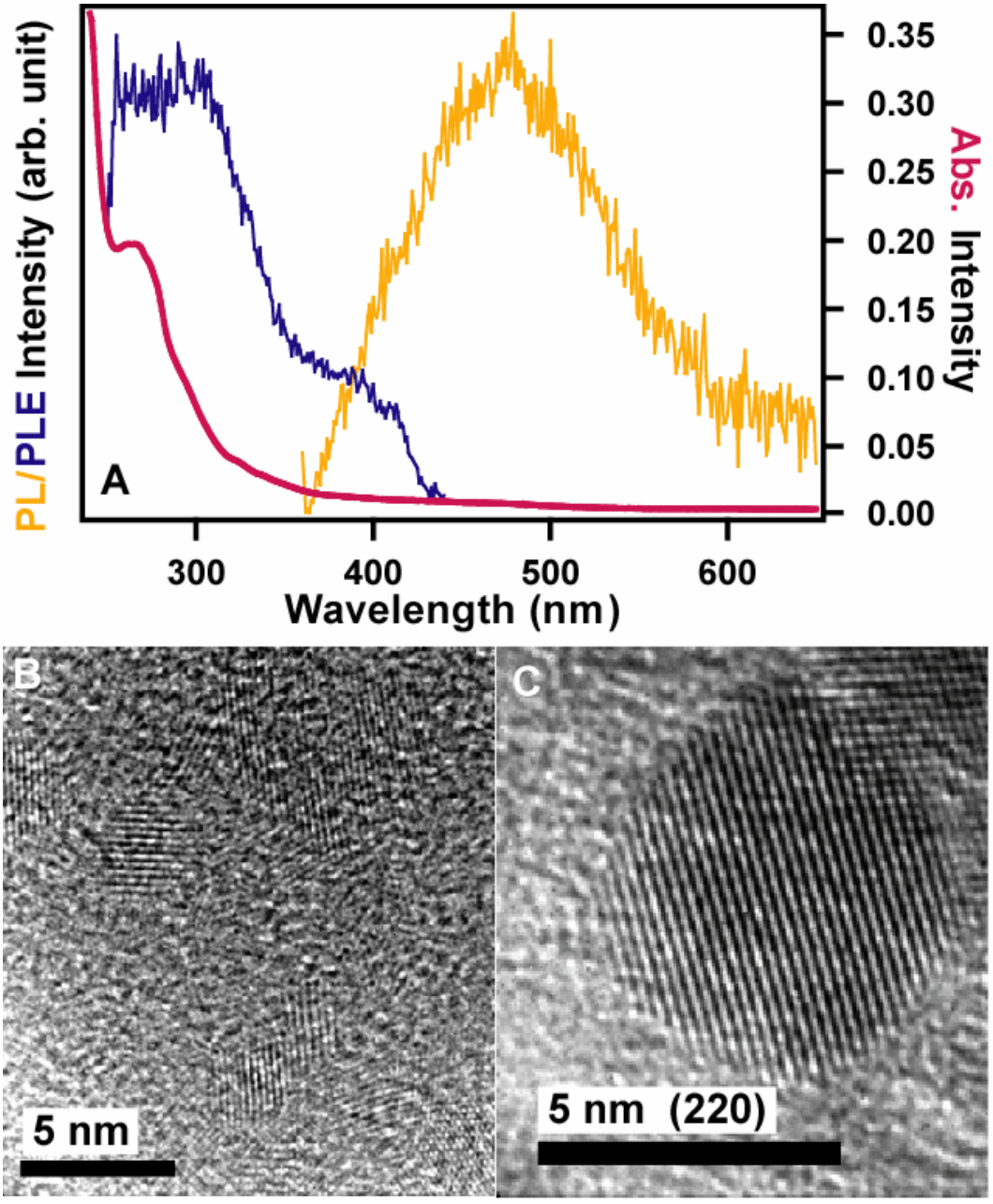

Figure 2.9 (A) Absorbance (red), PL (orange) and PLE (blue) of silicon nanocrystals synthesized with $SiBr_4$ and $LiAlH_4$ precursors via semi-batch injection. Crystallinity verified in (B) and (C) from HRTEM images.

This synthesis yielded a clean product, relative to the arylsilane reactions, which was crystalline and luminescent as evidenced in Figure 2.9.

The closed reactor system makes this synthesis possible because the *in situ* silane cannot escape as in a benchtop synthesis. Unfortunately, the silicon halides are extremely corrosive to metal in the presence of air. Although the semi-batch injection equipment allows the precursors minimal exposure to air, there is enough exposure to corrode the high pressure stainless steel tubing feeding the reactor and the 6-way valve. After 2 – 4 injections the metal has corroded/rusted to the point where no liquid can be pushed through. These lines also feed the 6-way valve, which is made of stainless steel, and it is rendered useless by the corrosive chemicals. Continuous replacement of high pressure tubing is marginally expensive and time consuming, but possible. Continuous replacement of the 6-way valve is not cost effective. Since the semi-batch injection reactions cannot be run in the nitrogen glove box, alternate silicon precursors (less corrosive) were investigated as well as some modifications to the experimental apparatus which would allow for truly oxygen free injection.

2.2.5 Alternate Silicon Precursors

Alternate silicon precursors such as tetramethylsilane, tetraethylsilane, hexamethyldisilane, 1,1,2,2-tetrachlorodimethyldisilane and trisilane were investigated.

Previous investigation of tetramethylsilane decomposition has shown that temperatures greater than 700°C are required for pyrolysis.[4] Temperatures above 600°C are not possible, or safe, in the supercritical fluid apparatus; additionally solvent decomposition would be severe. Attempts to decompose tetramethylsilane in supercritical hexane verified the literature results; there was no decomposition at 500°C.

Pyrolysis of tetraethylsilane has been carried out under helium at atmospheric pressures. The onset of decomposition occurs at 600°C and significant decomposition does not occur until at least 800°C.[16] Supercritical pyrolysis of tetraethylsilane has not been reported, but decomposition in supercritical hexane did not occur in temperatures up to 500°C.

Similarly, hexamethyldisilane has been reported to thermally decompose above 600°C.[3] A contradictory article by Sedgwick *et al*. reports a lower activation energy which predicts decomposition at temperatures achievable in the supercritical fluid apparatus.[1] However, Sedgwick *et al*. conducted experiments and observed reaction kinetics at temperatures in the range of 650-710°C. In our laboratory decomposition of hexamethyldisilane in supercritical solvents did not occur at temperatures up to 500°C.

Another potential precursor was investigated which would react similarly to the previously mentioned silicon halide precursors. 1,1,2,2-tetrachlorodimethyldisilane undergoes a metathesis reaction with lithium

aluminum hydride to form 1,2-dimethyldisilane which is volatile at low temperatures, around 40°C.[17] Thermal decomposition of dimethyldisilane under supercritical conditions should be a viable option for nanocrystal synthesis. Unfortunately, 1,1,2,2-tetrachlorodimethyldisilane possesses the same negative qualities as the other silicon halides; it is extremely corrosive. The same experimental modifications are required before 1,1,2,2-tetrachlorodimethyldisilane becomes a viable silicon precursor.

The last precursor investigated was trisilane; a pyrophoric liquid at room temperature. Trisilane decomposes at temperatures between 400-500°C and pressures between 2000-6000 psi. Trisilane is a very attractive silicon precursor, but it has not yielded *in situ* crystallized silicon. Its decomposition rate is very fast and it forms amorphous silicon particles of sizes 30-400 nm. Trisilane reaction products are discussed at length in Chapters 5 and 6.

2.3 Supercritical Solvents

Anhydrous hexane is the solvent of choice for the supercritical fluid synthesis. Hexane will thermally decompose as a supercritical fluid which is of concern to the silicon nanocrystal synthesis since the particles are difficult to precipitate out of solution. The solvent decomposition products may luminesce in the UV; therefore, it is important to minimize solvent decomposition. Minimization of temperature, pressure and the time hexane spends under supercritical conditions minimizes or prevents solvent decomposition. Alternate

anhydrous solvents were investigated such as cyclohexane, octanol, trimethylpentane, cyclopentane, benzene, toluene and methanol. Although a branched hydrocarbon such as trimethylpentane should be less likely to form cyclic byproducts and cyclopentane less likely to form aromatic compounds, all the solvents explored exhibited degradation at elevated temperatures and pressures. In the end, hexane is the better solvent for supercritical synthesis.

2.4 References

(1) Connor, J. A.; Haszeldine, R. N.; Leigh, G. J.; Sedgwick, R. D. *J. Chem. Soc. (A)* **1967**, *5*, 768-771.

(2) Coutant, R. W.; Levy, A. "A Kinetic Study of the Thermal Decomposition of Selected Cyclohexyl and Phenylsilanes," Aerospace Research Laboratories, 1969.

(3) Davidson, I. M. T.; Howard, A. B. *J. Chem. Soc., Chem. Commun.* **1973**, *9*, 323-324.

(4) Lee, Y. L.; Sanchez, J. M. *Journal of Crystal Growth* **1997**, *178*, 513-517.

(5) Walch, S. P.; Dateo, C. E. *Journal of Physical Chemistry A* **2001**, *105*, 2015-2022.

(6) Roenigk, K. F.; Jensen, K. F.; Carr, R. W. *J. Phys. Chem.* **1987**, *91*, 5732-5739.

(7) Levy, A.; Coutant, R. W.; Merryman, E. L.; Trent, D. E. "The Thermal Stability of Some Arylsilanes," Aerospace Research Laboratories, 1965.

(8) Pell, L. E.; Yu, Z.; English, D. S.; O'Connor, D.; Barbara, P. F.; Korgel, B. A. In *Materials Research Society Symposium*; Singh, R. K., M., M. P., Senna, M., Hofmann, H., Eds.: Boston, MA, 2001; Vol. 704.

(9) Itoh, M.; Inoue, K.; Ishikawa, J.; Iwata, K. *Journal of Organometallic Chemistry* **2001**, *629*, 1-6.

(10) Speier, J. L., Jr.; Zimmerman, R. E. *Journal of the American Chemical Society* **1955**, *77*, 6395-6396.

(11) *Work completed by Innovalight, Inc.*

(12) Gall, S.; Muske, M.; Sieber, I.; Nast, O.; Fuhs, W. *Journal of Non-Crystalline Solids* **2002**, *299*, 741-745.

(13) Saunderson, J. D.; Swanepoel, R. *Solar Energy Materials and Solar Cells* **1998**, *53*, 329-332.

(14) Al-Dhafiri, A. M. *Journal of Saudi Chemical Society* **2002**, *6*, 365-376.

(15) Reith, T. M.; Schick, J. D. *Applied Physics Letters* **1974**, *25*, 524-526.

(16) Amjoud, M. b.; Reynes, A.; Morancho, R.; Carles, R. *Journal of Materials Chemistry* **1992**, *2*, 1205-1208.

(17) Pinnow, M.; Wiacek, R.; Willson, C. G., For fruitful discussions about silane chemistry.

Chapter 3: Electrochemistry and Electrogenerated Chemiluminescence from Silicon Nanocrystal Quantum Dots[§]

3.1 Introduction

In a bulk semiconductor, electrons and holes move freely throughout the crystal. However, in a nanocrystal, confinement of the electrons and holes leads to a variety of optical and electronic consequences, including size dependent molecular-like optical properties, greater electron/hole overlap for enhanced photoluminescence (PL) efficiencies, and discrete single-electron/hole charging. Because of their enormous surface area–to–volume ratios, nanocrystals (NCs) are highly susceptible to heterogeneous redox chemistry with the surrounding environment. Depending on the semiconductor and the surface chemistry, this chemical reactivity can lead to either fatal chemical degradation or new useful properties, such as reversible photocatalytic and electrochromic properties and redox reactivity.

Semiconductor NCs have been prepared with narrow size distributions, controlled surface chemistry, and internal bulk crystal structure,[1,2] and adsorbed capping ligands are often used to control size and prevent irreversible aggregation. Although the electrochemical properties of monolayer-protected

[§] The contents of this chapter appear in *Science* vol. 296 p. 1293 **(2002)**.

metallic NCs have been well documented,[3,4] reports concerning the electrochemical properties of semiconductor NCs remain scarce.[5-9] Difficulties include the limited potential window available in aqueous solutions, the limited solubility of many NCs in nonaqueous solvents, and the need for highly pure, isolated, monodisperse dots. Compound semiconductor NCs, such as CdS, are also chemically unstable upon electron transfer. For example, CdS NCs are irreversibly oxidized and reduced when electron transfer occurs at an electrode.[7] Elemental semiconductor NCs, such as Si and Ge, should be more stable. Here we show that monolayer-protected Si NCs are chemically stable upon electron and hole injection; furthermore, electron/hole annihilation through electron transfer reactions between NCs, or NCs with redox-active coreactants, leads to visible light production [electrogenerated chemiluminescence (ECL)].

3.2 Experimental Section

3.2.1 Nanocrystal Preparation

We recently developed a new synthetic strategy to produce Si NCs terminated with a capping agent consisting of a combination of hydrogen and alkoxide, using solvents heated and pressurized above their critical points to temperatures between 350° and 500°C.[10] These NCs are efficient emitters of visible light, with quantum yields between 5 and 20% and size-tunable color that can range from blue to red, different from H- or oxide-terminated samples in the

same size range reported earlier. This efficiency is rather remarkable, given that the indirect band gap of bulk Si makes it a poor candidate for a light-emitting material. Although the precise origin of the light emission is still unknown,[11] quantum confinement in Si has led to efficient PL,[12,13] and radiative transitions have been observed[2] in a variety of Si nanostructures, including thin wires,[14] dots,[10] and porous Si.[2,15] For the experiments reported here, octanol-, octene- and octanethiol-capped Si NCs were prepared in supercritical cyclohexane according to the methods described in **(*10*).** The Si NCs are readily soluble in a variety of organic solvents, including those used here: *N*,*N*'-dimethylformamide (DMF) and acetonitrile (MeCN).

3.2.2 Characterization

The electrochemical properties of freely diffusing Si NCs dispersed in nonaqueous organic solvents were measured at a Pt electrode. General experiments for electrochemistry (such as cyclic voltammetry and differential pulse voltammetry) and ECL of Si nanoparticles were done as follows: A cylindrical Pyrex vial 1.2 cm in diameter was used as an electrochemical cell, where a 1- or 2-mm Pt disk, Pt coil, and silver wire served as working, counter, and reference electrodes, respectively. The ECL signal was recorded on a charge-coupled device camera. ECL could also be measured by a photomultiplier tube and recorded as cyclic voltammetric ECL or ECL transients.

3.3 Results and Discussion

3.3.1 Differential Pulse Voltammetry

Discrete steps associated with single-electron charging and a large central gap between the onset of oxidation and reduction, characteristic of the energy difference between the highest occupied and lowest unoccupied molecular orbitals (the HOMO- LUMO gap), were observed. Typical electrochemical responses for different solutions of Si NCs are given in Figure 3.1, with NC sizes of (i) 2.77 $\pm$ 0.37, (ii) 2.96 $\pm$ 0.91, and (iii) 1.74 $\pm$ 0.67 nm. For example, in Figure 3.1A, there are as many as five well-resolved differential pulse voltammetry (DPV) peaks between 0 and –2.1 V. These regularly spaced peaks are reversible and highly reproducible. The observed response was stable on repetitive potential cycling over long time periods, with no evidence of fouling or film formation on the Pt electrode surface.

This DPV response is analogous to that observed by Murray and co-workers[4] for thiol-capped metal clusters, who introduced the term quantized double-layer charging to differentiate this collective electrochemical response from Coulomb blockade phenomena observed for single-charge injection to isolated individual dots in scanning tunneling microscopy (STM) experiments, also called "addition spectra".[16] Unlike the electrical response measured by STM, the electrochemical response is limited by quantum dot diffusion to the electrode surface. Nonetheless, the charging energy μ_i required for electron or hole

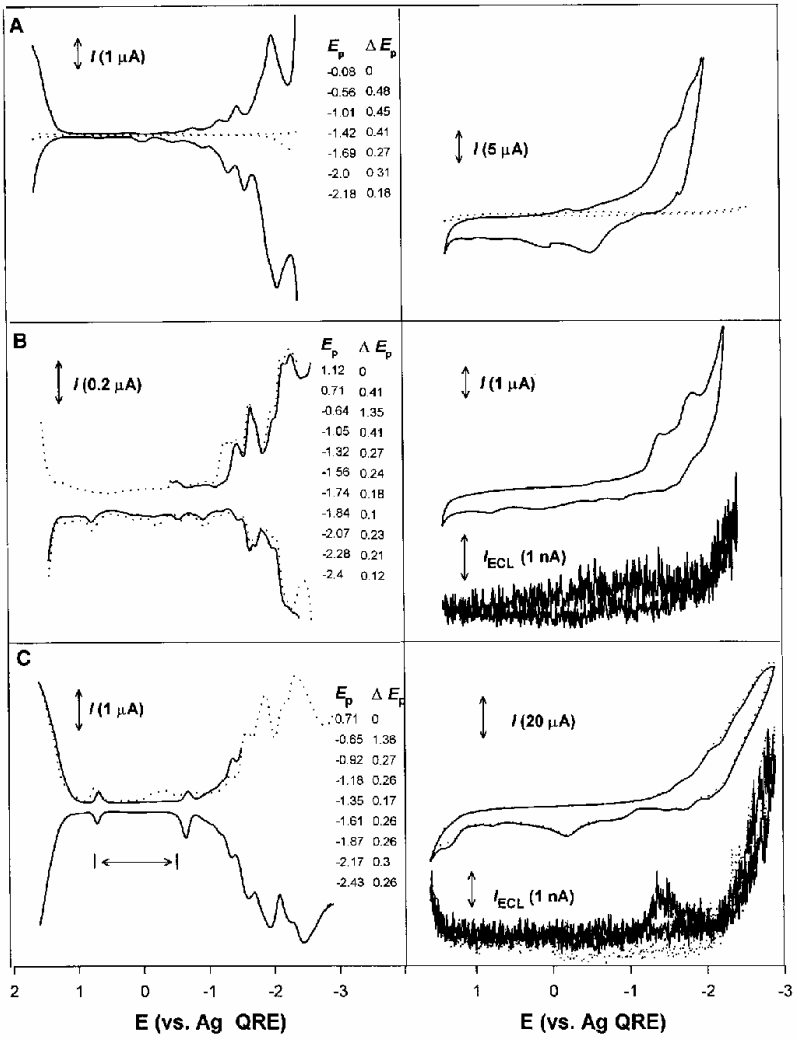

Figure 3.1 Cyclic voltammograms (right panels) and differential pulse voltammograms (left panels) for several batches of Si nanoparticles in 0.1 M tetrahexylammonium perchlorate (THAP) DMF solution. *I*, current; E_p, current peak potential, ΔE_p, potential difference between two succeeding peaks; IECL, ECL photocurrent from the photomultiplier tube; QRE, quasi-reference electrode. The NC's size and dispersion were (A) 2.77 + 0.37, (B) 2.96 + 0.91, and (C) 1.74 + 0.67 nm. Cyclic voltammetric ECL voltage curves are plotted in (B) and (C). The dotted curves in (A) represent the response of the blank supporting electrolyte solution. The dotted curves in (B) and (C) are the responses for different initial DPV scan potentials.

addition is the same for STM and DPV measurements. For example, we recently observed an electrochemical Coulomb staircase based on two nanometer-sized electrodes connected in series through a solution containing a redox couple.[17]

The small size of the NCs causes electron addition to be quantized. The charging energy required to add the first electron μ_1 equals the electron quasiparticle energy ε_{e1}, which depends on the size-dependent shift in the LUMO ε_{e1}^{0} and the electron "self-energy" Σ_{e1}, which results from its image charge in the surrounding dielectric media: $\varepsilon_{e1} = \varepsilon_{e1}^{0} + \Sigma_{e1}$. Calculated values of Σ_{e1} typically range from 0.2 to 0.5 eV for Si nanocrystals in the size range studied here.[18] A second electron must also overcome the electron-electron Coulomb interaction $J_{e1,e2}$ within the particle to add to a negatively charged NC, $\Delta_{1,2}^{(e)} = \mu_2 - \mu_1 = J_{e1,e2}$. For Si dots, the calculated ε_{e1} values are almost entirely determined by Coulomb energies, because the six lowest-energy conduction levels are very close in energy. A classical estimation of $J_{e1,e2} \approx e^2/2C_{NC}$ reveals that the sub-attofard (aF) capacitances for NCs give rise to $\Delta_{1,2}^{(e)} >> k_B T$ even at room temperature, leading to discrete charging events in the DPV scans.[4,8,17,19] If C_{NC} is independent of the number of electrons injected, consecutive charge injection should occur in regular potential steps, $\Delta V = e/C_{NC}$.[4,17] Although the DPV peaks in Figure 3.1 were not separated by exactly the same ΔV, the average $\Delta V \approx 0.4$ V corresponds to a capacitance of approximately 0.4 aF per cluster (Figure 3.1A); this is

comparable to the value reported for organic-capped noble metal clusters.[3] The ΔV compares favorably with values reported for organic-capped Au nanocrystals and with recent calculations by Franceschetti and Zunger[18] for Si quantum dots with $\Delta_{1,2}^{(e)}$ on the order of ~0.4 to 0.6 eV. With increasing NC charge, ΔV decreased measurably, perhaps because of multielectron effects or NC size dispersity, which can smear the observed responses shown in Figure 3.1A and B.[3] The electrochemical behavior seen in these figures was very sensitive to the NC size variation ($\pm$0.37 nm in Figure 3.1A and $\pm$0.91 nm in Figure 3.1B).

The DPV responses in Figure 3.1 are from differently sized NCs. Common features include the appearance of a large central gap ($\mu_1 - \mu_{-1} > 1.3$ V; the subscript "–1" refers to the hole chemical potential) and the general absence of DPV peaks in the positive potential region. This last feature was not a limitation of the available electrochemical window, as seen in Figure 3.1A, where the DPV response in the absence of Si NCs is given. Electron injection occurred as discrete charging events; however, NC oxidation (hole injection) was not generally quantized although calculations suggest that it should be,[18] and the DPV response was characterized by a continuous increase in current with potential indicative of multiple charge transfers. Nevertheless, the forward and reverse DPV scans are relatively symmetric, indicating that both single and multiple charge transfers are reversible. For comparable CdS and PbS NCs,[6,7] electrochemical electron and hole injection were irreversible and multielectron

transfer processes were proposed; that is, the injected charge was consumed by fast coupled chemical reactions due to cluster decomposition. The large size dependent central gap relates to the energetic difference (the HOMO-LUMO gap),[4] reflecting the quantized electronic structure of the semiconductor NC[18]: $\mu_1 - \mu_{-1} = \varepsilon_{e1}^{0} - \varepsilon_{h1}^{0} + \Sigma_{e1} + \Sigma_{h1}$. The optical gap ε_{gap}^{opt}, however, relates to ε_{e1}^{0}, ε_{h1}^{0} and the electron-hole Coulomb interaction $J_{e1,h1}$: $\varepsilon_{gap}^{opt} = \varepsilon_{e1}^{0} - \varepsilon_{h1}^{0} - J_{e1,h1}$. Therefore, $(\mu_1 - \mu_{-1}) - \varepsilon_{gap}^{opt} = \Sigma_{e1} + \Sigma_{h1} + J_{e1,h1}$. The HOMO-LUMO gap increases with decreasing NC size from 2.96 $\pm$ 0.91 nm in Figure 3.1B to 1.74 $\pm$ 0.67 nm in Figure 3.1C. However, this apparent electrochemical gap can be affected by the presence of nonpassivated surface states that can act as local traps for electrons and holes. We estimate that 30 to 50% of the surface of the NC may be ligand-free and coated with a mixture of H, Si–C = O and possibly a small amount of oxide.[10]

3.3.2 Electrogenerated Chemiluminescence

Light emission by charge injection, or ECL, into freely diffusing NCs occurred under repetitive electrode potential cycling (as in Figure 3.1B and C) or pulsing (Figure 3.2) between NC oxidation and reduction. In ECL experiments, electron-transfer annihilation of electrogenerated anion and cation radicals results in the production of excited states[19,20]

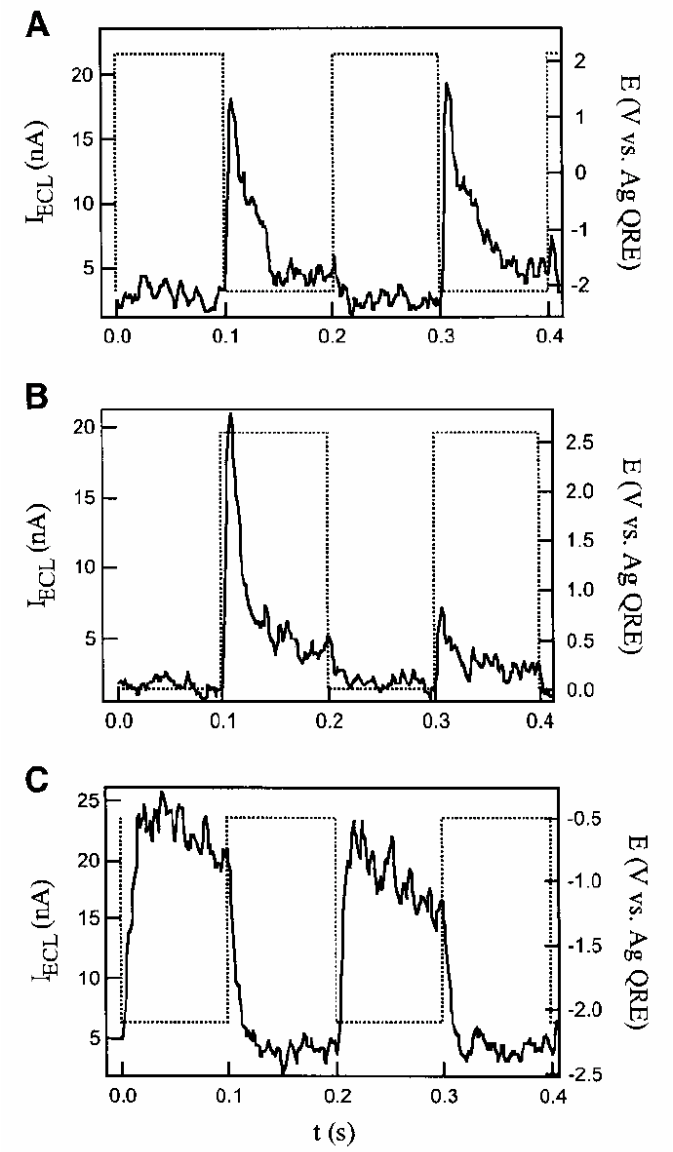

Figure 3.2 ECL transients for (A) annihilation of cation and anion radicals in 0.1 M THAP MeCN solution; (B) an oxalate coreactant system with 2.5 mM tetrabutylammonium oxalate added to the solution of (A); and (C) a persulfate coreactant system in 0.1 M THAP DMF solution with 6 mM tetrabutylammonium persulfate added. The nanoparticles are ~2 to 4 nm in diameter. Dotted curves indicate applied potential steps; solid curves indicate ECL transients. *t* , time.

$$R^{-\bullet} + R^{+\bullet} \rightarrow R^{*} + R \quad (3.1)$$

$$R^{*} \rightarrow R + h\nu \quad (3.2)$$

In this case, R^- and R^+ refer to negatively and positively charged Si NCs electrogenerated at the Pt electrode, which then react in solution to give the excited state R*. ECL was not observed through an annihilation-type mechanism 3.1 for thioglycerol-capped CdS quantum dots[7] because of the instability of electrogenerated reactants. In order for ECL to occur through mechanism 3.1, the NCs must be chemically stable and maintain their charged states long enough to transfer charge upon colliding with oppositely charged NCs in solution. The relative ECL intensity was greater in the potential region where anionic NCs are electrogenerated (Figures 3.1C and 3.2A), which may indicate that the electrogenerated oxidized forms are more stable. Light emission was not observed when the applied electrode potential was not sufficient to generate both the negatively and positively charged species. The ECL spectrum (Figure 3.3A) obtained from the annihilation (Equation 3.1) in MeCN, where the applied electrode potential was pulsed between the oxidation and reduction potentials (double potential step) in 100-ms steps,[19,20] showed a maximum at 640 nm.

Higher intensity light emission from the Si NC solution was observed when coreactants were added, which help overcome either the limited potential window of a solvent or poor radical anion or cation stability.[19] For example, by adding excess $C_2O_4^{2-}$ to the NC solution (Figure 3.2B), ECL only requires hole

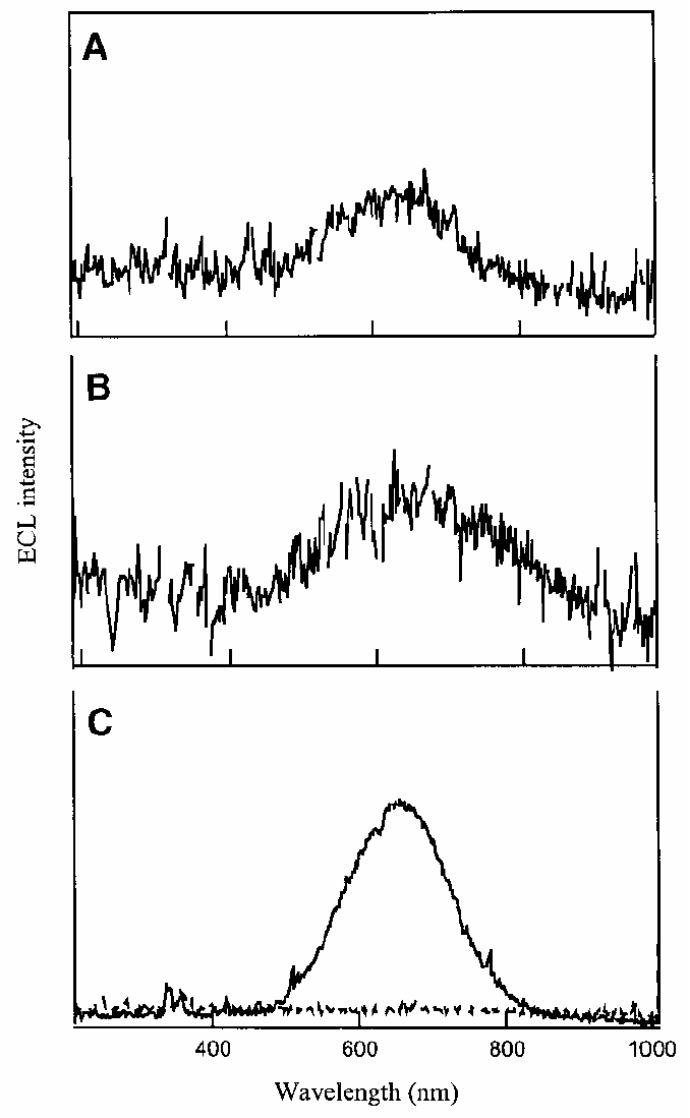

Figure 3.3 ECL spectra for (A) annihilation of cation and anion radicals generated by stepping the potential between 2.7 and –2.1 V at 10 Hz with an integration time of 30 min in the same solution as in Figure 3.2A; (B) an oxalate coreactant system, stepping the potential between 0.1 and 3 V at 10 Hz, integration time 40 min in the same solution as in Figure 3.2B; and (C) a persulfate coreactant system, stepping the potential between –0.5 and –2.5 V at 10 Hz, integration time 10 min in the same solution as in Figure 3.2C. The dotted curve in (C) is the ECL spectrum for the blank solution.

injection and can be obtained by simply oxidizing the NCs. In this case, the oxidation of oxalate produces a strong reducing agent, $CO_2^{-\bullet}$, which can inject an electron into the LUMO of an oxidized Si NC to produce an excited state that then emits light (Figures 3.2B and 3.3B).[19,21]

$$R^{+\bullet} + CO_2^{-\bullet} \rightarrow R^* + CO_2 \tag{3.3}$$

Similarly, ECL was observed in the potential region for NC reduction through the addition of excess $S_2O_8^{2-}$ to solution. Reduction of persulfate produces a strong oxidant, SO_4^-, which can then react with the negatively charged NCs by injecting a hole into the HOMO, producing an excited state (Figures 3.2C and 3.3C)[22,23]

$$R^{-\bullet} + SO_4^{-\bullet\bullet} \rightarrow R^* + SO_4^{2-} \tag{3.4}$$

A higher concentration of Si NCs was used for the persulfate measurements, which may account for the higher ECL intensity and lower decay rate apparent in Figures 3.2C and 3.3C in comparison to Figure 3.2A and B, and Figure 3.3A and B. The solvent used may also play a role. After the ECL experiments, the solutions showed the same PL as the original solution, so no bulk degradation of the Si NCs occurred.

The ECL spectra in the above three cases all show a maximum wavelength of 640 nm, which is substantially red-shifted from that in the PL spectra (Figure 3.4B). The orange ECL emission was not sensitive to NC size or the capping agent used. On the other hand, the Si NC PL is size-dependent.[10] A few important observations and conclusions can be drawn from the ECL data. First of

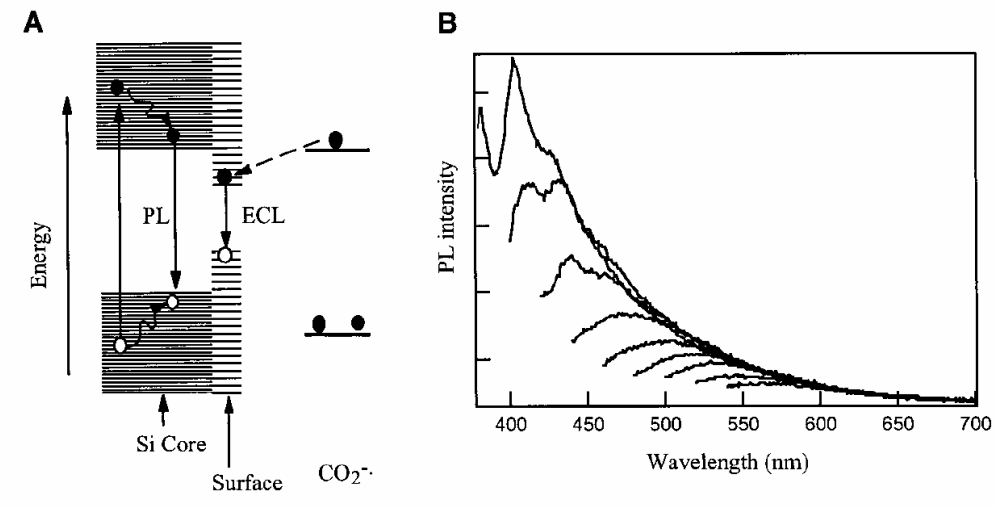

Figure 3.4 (A) Schematic mechanisms for ECL and PL of Si clusters. (B) PL spectra at different excitation energies recorded with the same solution as in Figure 3.2A. The excitation wavelength from top to bottom was between 360 and 520 nm at 20-nm intervals.

all, the electrochemical "turn-on voltage" (that is, the potential gap in Figure 3.1B and C) for radiative electron-hole annihilation between positive and negatively charged NCs exceeds the optical transition energy. This observation is consistent with electron and hole injection into separate NCs requiring greater energy than optical excitation. Second, the turn-on voltage for ECL significantly exceeds $\mu_1 - \mu_{-1}$. Although the potential difference $\mu_1 - \mu_{-1}$ enables electron and hole injection, and electron transfer between charged NCs in solution is possible, the carrier energies are not large enough to produce optically radiative electron-hole recombination. This observation is consistent with previous observations of Si NCs. Excitation energies for efficient PL significantly exceeded the absorption edge, with PL intensity that depends sensitively on excitation energy, as shown in Figure 3.4B, in which the excitation wavelength from top to bottom was between 360 and 520 nm at 20-nm intervals. The shift in peak position with excitation energy is unlikely to be caused by polydispersity, because the NCs were size-selected by column chromatography. Furthermore, the PL energy is considerably greater than the absorption edge, indicating that the lowest-lying energy levels do not result in strongly radiative transitions. Qualitatively, the ECL and DPV data are as expected for Si NCs.

Quantitatively, however, the energetic difference between the PL and ECL of approximately 0.8 eV is more difficult to understand and suggests that the emitting states are different. Previously, for Si NCs terminated with hydrogen

atoms, the indirect band gap was reported to shift from the bulk value of 1.1 eV to ~2.1 eV for nanocrystals about 2 nm in diameter, and the direct transition appeared to blue shift by 0.4 eV from its 3.4 eV bulk value over the same size range. In that case, violet PL (~365 nm) was the most intense emission and was attributed to direct electron-hole recombination, whereas other less intense PL peaks (~580 nm) were assigned to surface state and phonon-assisted recombination.[11] Undoubtedly, ECL depends more sensitively on surface chemistry and the presence of surface states. PL mainly occurs through excitation and emission within the NC core, though the electron and hole wave functions can interact strongly with the NC surface. Despite a few notable exceptions,[24,25] charge injection in a Si nanocrystal is generally assumed to occur via its surface states, given the large surface area and the possible presence of many dangling bonds. If we consider the Si NC/oxalate coreactant system (Equation 3.3) as an example, the Si cores have band gaps greater than the energy separation of the surface states. The core band gaps depend on the NC size, whereas the energy separation of the surface states is only slightly affected by the particle size[11,26] (Figure 3.4A). As the electrode potential is made more positive, holes are injected into the particle. Concurrently, oxalate is oxidized and undergoes a following chemical reaction generating the powerful reducing agent CO_2^-. This intermediate injects an electron across the particle surface (Equation 3.3) and makes emission possible through surface electron-hole recombination. The other

two ECL processes (Equations 3.1 and 3.4) are assumed to occur through a similar mechanism. The observed ECL emission insensitivity to core size and capping agent supports the surface state conjecture[11] and this proposed mechanism. Thus, the difference in light emission through PL and ECL from the same Si NCs most likely results from the greater significance of surface states for charge injection as opposed to photoinjection. Similar long-wavelength emission is found with porous Si produced by anodic etching in the presence of organic surface modifiers.[27]

3.4 Conclusions

Reversible electrochemical injection of discrete numbers of electrons into sterically stabilized silicon nanocrystals (NCs) (~ 2 to 4 nanometers in diameter) was observed by differential pulse voltammetry (DPV) in *N*,*N*'-dimethylformamide and acetonitrile. The electrochemical gap between the onset of electron injection and hole injection—related to the highest occupied and lowest unoccupied molecular orbitals—grew with decreasing nanocrystal size, and the DPV peak potentials above the onset for electron injection roughly correspond to expected Coulomb blockade or quantized double-layer charging energies. Electron transfer reactions between positively and negatively charged nanocrystals (or between charged nanocrystals and molecular redox-active coreactants) occurred that led to electron and hole annihilation, producing visible light. The electrogenerated chemiluminescence spectra exhibited a peak

maximum at 640 nanometers, a significant red shift from the photoluminescence maximum (420 nanometers) of the same silicon NC solution. These results reveal that NCs of the elemental semiconductor Si are more chemically robust than the compound semiconductor NCs studied to date. The Si NCs have the ability to store charge in solution, which can subsequently lead to light emission upon electron and/or hole transfer. This quality provides electrochemically sensitive optoelectronic properties that may find future use in new sensor technologies.

3.5 References

(1) Alivisatos, A. P. *Science* **1996**, *271*, 933-937.

(2) Iyer, S. S.; Xie, Y. H. *Science* **1993**, *260*, 40-46.

(3) Chen, S. W.; Murray, R. W.; Feldberg, S. W. *J. Phys. Chem. B* **1998**, *102*, 9898-9907.

(4) Chen, S. W.; Ingram, R. S.; Hostetler, M. J.; Pietron, J. J.; Murray, R. W.; Schaaff, T. G.; Khoury, J. T.; Alvarez, M. M.; Whetten, R. L. *Science* **1998**, *280*, 2098-2101.

(5) Hoyer, P.; Weller, H. *Chem. Phys. Lett.* **1994**, *224*, 75-80.

(6) Chen, S. W.; Truax, L. A.; Sommers, J. M. *Chem. Mat.* **2000**, *12*, 3864-3870.

(7) Haram, S. K.; Quinn, B. M.; Bard, A. J. *J. Am. Chem. Soc.* **2001**, *123*, 8860-8861.

(8) Hanna, A. E.; Tuominen, M. T.; Tinkham, M. *Phys. Rev. Lett.* **1992**, *68*, 3228-3231.

(9) Hoyer, P.; Weller, H. *J. Phys. Chem.* **1995**, *99*, 14096-14100.

(10) Holmes, J. D.; Ziegler, K. J.; Doty, R. C.; Pell, L. E.; Johnston, K. P.; Korgel, B. A. *J. Am. Chem. Soc.* **2001**, *123*, 3743-3748.

(11) Wilcoxon, J. P.; Samara, G. A.; Provencio, P. N. *Phys. Rev. B* **1999**, *60*, 2704-2714.

(12) Kovalev, D.; Heckler, H.; Ben-Chorin, M.; Polisski, G.; Schwartzkopff, M.; Koch, F. *Phys. Rev. Lett.* **1998**, *81*, 2803-2806.

(13) Nirmal, M.; Brus, L. *Accounts Chem. Res.* **1999**, *32*, 407-414.

(14) Holmes, J. D.; Johnston, K. P.; Doty, R. C.; Korgel, B. A. *Science* **2000**, *287*, 1471-1473.

(15) McCord, P.; Yau, S. L.; Bard, A. J. *Science* **1992**, *257*, 68-69.

(16) Andres, R. P.; Bein, T.; Dorogi, M.; Feng, S.; Henderson, J. I.; Kubiak, C. P.; Mahoney, W.; Osifchin, R. G.; Reifenberger, R. *Science* **1996**, *272*, 1323-1325.

(17) Fan, F. R. F.; Bard, A. J. *Science* **1997**, *277*, 1791-1793.

(18) Franceschetti, A.; Zunger, A. *Phys. Rev. B* **2000**, *62*, 2614-2623.

(19) Bard, A. J.; Faulkner, L. R. *Electrochemical Methods: Fundamentals and Applications*; 2nd ed.; Wiley: New York, 2001.

(20) Faulkner, L. R.; Bard, A. J. In *Electroanalytical Chemistry*; Bard, A. J., Rubenstein, I., Eds.; Marcel Dekker: New York, 1998; Vol. 20, pp 1-95.

(21) Richards, T. C.; Bard, A. J. *Anal. Chem.* **1995**, *67*, 3140-3147.

(22) White, H. S.; Bard, A. J. *J. Am. Chem. Soc.* **1982**, *104*, 6891-6895.

(23) Knight, A. W.; Greenway, G. M. *Analyst* **1994**, *119*, 879-890.

(24) Shim, M.; Guyot-Sionnest, P. *Nature* **2000**, *407*, 981-983.

(25) Wang, C. J.; Shim, M.; Guyot-Sionnest, P. *Science* **2001**, *291*, 2390-2392.

(26) Makimura, T.; Kunii, Y.; Ono, N.; Murakami, K. *Appl. Surf. Sci.* **1998**, *129*, 388-392.

(27) Choi, H. C.; Buriak, J. M. *Chem. Mat.* **2000**, *12*, 2151-2156.

Chapter 4: Size Tunable Visible Luminescence from Individual Organic Monolayer Stabilized Silicon Nanocrystal Quantum Dots[§]

4.1 Introduction

Due to the indirect band gap in silicon (Si), light absorption and emission occurs only when absorption or emission of a phonon, or a lattice vibration, occurs simultaneously to preserve crystal momentum.[1] This second-order process makes Si an extremely inefficient light emitter. In molecular spectroscopic terms, the lowest electronic transition in Si is dipole forbidden. Therefore, *bulk* Si—the cornerstone material in microelectronics technology—does not possess the physical properties required to play a central role in future ultra-high speed optoelectronic technologies. However, by creating Si with nanoscale dimensions, it can be coaxed to emit visible light with relatively high efficiencies.[2,3] Quantum confinement increases the energetic gap between the highest occupied and lowest unoccupied molecular orbitals (HOMO-LUMO gap), shifting the band gap from 1.1 eV in bulk Si all the way into the blue (~3.0 eV) for 2 nm structures.[4,5] The efficiency of light emission greatly increases as the loss of crystal translational symmetry relaxes the *k*-conservation rule and radiative electron-hole band-edge recombination becomes increasingly dipole allowed,[6] but the nanoscale Si band edge transition remains indirect as predicted from calculations. The porous

[§] The contents of this chapter appear in *Nano Letters* **2**(7) p. 681 **(2002)**.

silicon (por-Si) and oxide-coated Si nanocrystals studied to date have retained a significant amount of indirect character, with radiative rates, or excited state lifetimes, a few orders of magnitude slower than those expected for a typical dipole allowed transition in a direct band gap semiconductor.[5,7,8] This property is not conducive to the application of nanoscale Si in light emitting diodes and ultra-fast optical switches with 100 MHz or 1 GHz frequencies. It also limits the use of powerful spectroscopic techniques for analyzing the optical properties of individual nanocrystals, which require significantly faster radiative rates. For example, if the lifetime of the emitting state was ~500 μs, the fastest excitation frequency would be ~2 kHz, which rivals the background counts on the detector at reasonable excitation intensity. Emission from a collection of several particles would be observable, but the size-dependent PL would broaden the measured spectra as observed in Reference 9.

Our laboratory has synthesized sterically-stabilized Si nanocrystals with diameters in the range of 10 to 100 Å.[4] These particles possess excited state lifetimes on the nanosecond-scale, which are much shorter than those measured previously for nanoscale Si, allowing us to utilize scanning confocal microscopy to examine the photoluminescence (PL) spectra of *individual* Si nanocrystals of varying size.[9] Consistent with quantum confinement, the PL is size dependent. The single dot spectra exhibit line widths as narrow as 150 meV at room

temperature (approximately three times broader than room temperature PL spectra for individual CdSe nanocrystals) as well as stochastic single-step "blinking" behavior. These spectra represent the sharpest spectra for nanoscale Si observed to date.

4.2 Experimental Section

4.2.1 Nanocrystal Preparation

Sterically-stabilized Si nanocrystals are grown by arrested precipitation in solvents heated and pressurized above their critical points to temperatures ranging from 400 to 500^{o}C (above ~80 bar).[4] These temperatures are sufficient to degrade available organosilane precursors, such as diphenylsilane, to Si; to promote Si crystallization in the nanocrystal core; and to initiate surface binding of organic capping ligands that provide steric stabilization of the particles. Si nanocrystals were synthesized via thermal degradation of a silicon precursor in supercritical hexane. 1.5 mL of a stock Si precursor solution (250 mM diphenylsilane and 25 mM octanethiol in hexane) was loaded into a 10 mL cylindrical titanium reactor in a nitrogen glove box. All chemicals used for the synthesis were degassed to remove oxygen and stored in a nitrogen rich environment. The titanium reactor was sealed, removed from the glove box, wrapped with high temperature heating tape and heated to 500^{o}C. The reaction proceeded at 500^{o}C and 83 bar for 30 minutes. The reactor was then allowed to cool to room temperature over the

course of approximately 2.5 hours. The product was extracted with chloroform and precipitated in excess ethanol to remove reaction byproducts. The nanocrystals could be redispersed in a variey of organic solvents for further manipulation for later analysis.

4.2.2 Nanocrystal Surface Properties

After synthesis, the nanocrystals are readily isolated from the reactor and can be exposed to ambient conditions without noticeable decay of the optical properties. (The optical properties of the nanocrystals do not appear to change over time after exposure to air; however, oxygen and water may indeed affect the optical properties of the material and oxygen- and water-free optical experiments remain to be conducted.) The chemical passivation nearly eliminates susceptibility to environmental factors, such as humidity and oxygen, which is very important, given that the optical properties of por-Si PL are extremely sensitive to oxygen exposure.[6] The single particle PL peak energy does not shift with exposure time, although the fluorescence "blinks" on and off characteristically as do other nanocrystals and molecules (see discussion below). Time-correlated single photon counting measurements reveal that light emission from these surface-passivated nanocrystals originates with a radiative rate of $\sim 2 \times 10^7\ s^{-1}$, apparently from an *allowed* optical transition. We compare the

results of these studies with those of CdSe nanocrystals, which represent a very well studied *direct* band gap semiconductor.

4.2.3 Characterization

Single dot spectroscopy measurements were conducted using a confocal optical microscope in an epi-illumination configuration. Samples consist of Si nanoparticles dispersed on a glass coverslip by spin coating a very dilute nanoparticle suspension in chloroform. The excitation laser beam from an Ar^+ continuous wave laser was focused by an oil immersion objective (1.2 NA) to a diffraction-limited spot on the sample coverslip. A computer-controlled piezo stage scans the sample. The sample photoluminescence was collected through the same objective, filtered with a holographic notch filter to remove residual excitation light, and detected by an avalanche photodiode (APD). Alternatively, the emission spectra are obtained by directing the light output to a polychromator equipped with an intensified charged-coupled device (ICCD) to record the intensity as a function of wavelength.

In order to gain a better understanding of the nature of the light emitting state in these organic-monolayer passivated nanocrystals, PL lifetimes were measured and the radiative rate was determined. Fluorescence decays were obtained by time-correlated single photon counting (TCSPC) with 488-nm with vertically polarized excitation pulses (Δt~200 fs, repetition rate 3.8 MHz) from a

mode-locked Ti:sapphire laser system (Coherent Mira 900, Coherent Pulse Picker Model 9200, Inrad SHG/THG model 5-050). Emission was collected at 90° with respect to the incident excitation axis through a Glan-Taylor polarizer set at the "magic angle" of 54.7°. Long pass filters and/or narrow band interference filters were used to block scattered laser light. Detection electronics included a microchannel plate detector (Hamamatsu R3809U-50), constant fraction discriminators (Tennelec TC454), time-to-amplitude converter (Tennelec TC864), and multichannel analyzer (Ortec TRUMP MCB). The emission wavelength was selected using 10 nm-width bandpass filters. The emission decay curves were evaluated by an iterative nonlinear least squares fitting procedure. The decay data was fit to a sum of exponential decays convoluted with the instrument response (~50 ps FWHM). The quality of the fit was evaluated by the reduced χ^2.

4.3 Results and Discussion

4.3.1 Single Particle Spectroscopy

4.3.1.1 Measurement Criteria

In preliminary experiments, samples were prepared for scanning confocal microscopy by drop casting onto a microscope cover slip. However, this method produces particle aggregates regardless of the solvent or method used, as has been observed for CdSe nanocrystals.[10] Spin coating from a chloroform dispersion provides samples with relatively homogeneous coverage of individual particles

separated by the required 0.5 μm for single particle imaging. Nonetheless, aggregates of particles could not be altogether avoided. Therefore, a set of spectroscopic guidelines was developed to ensure that the measured PL spectra originated from individual nanocrystals and not from multiple nanocrystals, or aggregates. As has been found for many single molecule systems, and other nanocrystals such as CdSe[11] and InP,[12] the Si nanocrystals exhibit fluorescence intermittency, or "blinking", with a stochastic switching on and off of the PL signal. The "on" state can be viewed as an optically coupled ground and excited state, whereas the "off" state is an optically "dark" state. Although the mechanism for blinking in nanocrystals is not known, experimental results and simulations suggest particle charging and Auger effects may be responsible.[13-15] The nanocrystals were also found to irreversibly bleach over the course of approximately 30 seconds. The emission from a cluster of particles exhibited intensity blinking against a gradually decaying background signal as shown in Figure 4.1A. One obvious test therefore involved the inspection of the time-resolved spectra for a gradually decaying background signal. In cases with few particles, a decaying background did not appear; however, the blinking behavior exhibited multiple intensity steps. In the single particle case, the blinking spectra clearly exhibited monotonic time-dependent PL intensities. As a secondary indicator, the PL peak energy fluctuation was examined. When multiple particles produced the emission, the spectra fluctuated in energy as different sized particles

blinked on and off. Therefore, the blinking behavior and peak fluctuation were used to rigorously determine if the measured spectra were truly a result of individual nanocrystals (See Figure 4.1).

4.3.1.2 Single Particle Photoluminescence

The octanethiol-capped Si nanocrystals used for the optical experiments were spherical with well-crystallized cores, as revealed by transmission electron microscopy (TEM) (see Figure 4.2). To obtain PL spectra from individual Si nanocrystals with a range of sizes in a single experiment, octanethiol-coated Si nanocrystals were synthesized with a broad size distribution, having an average diameter of 4.65 $\pm$ 1.36 nm as determined by TEM (based on 361 dots) and 4.35 $\pm$ 2.02 nm determined by AFM height profiles of the sample (Figure 4.2A). The PL spectra obtained from the nanocrystals dispersed in chloroform were correspondingly broad. For example, the PL peak shown in Figure 4.2B shifts as a function of excitation wavelength largely due to the broad size distribution of the sample. At longer excitation wavelengths, only the larger nanocrystals with lower HOMO→LUMO energies are excited and the emission peak shifts to longer wavelengths. The absorbance spectra and the photoluminescence excitation (PLE) spectra are featureless, due in part to the indirect nature of the Si band gap, but primarily due to the broad size distribution of the nanocrystals. At the single particle level, however, the PL spectra is narrow, exhibiting peaks with FWHM of 1596 $\pm$ 502 cm^{-1} (~200 meV) (See Figure 4.1B).

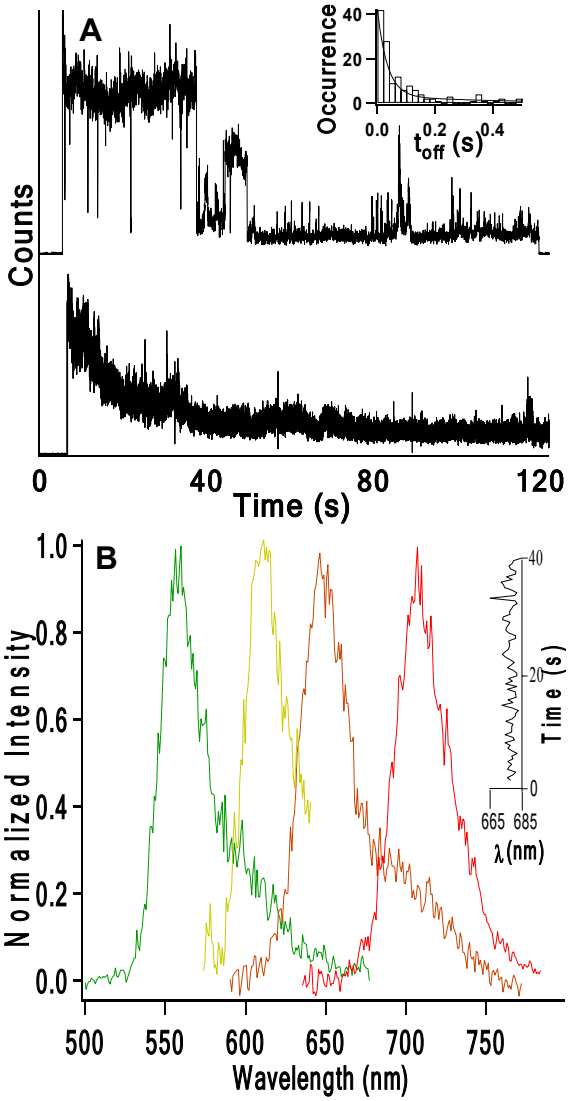

Figure 4.1 (A) Blinking—a comparison between the blinking of a single dot (top) and the blinking of a cluster (bottom); inset shows a histogram of the "off" times for the single dot blinking. (B) Four single dot PL spectra, showing the narrow line widths. Inset: Mean spectral trajectory of a single particle showing that spectral diffusion is not observable within the experimental accuracy of the instrumentation.

The spectral line widths of the single Si dot PL were as narrow as 150 meV. Although three times broader than the room temperature line widths measured for single CdSe nanocrystals,[13] these line widths represent the narrowest measured to date for Si nanostructures. The four peaks shown in Figure 4.1B represent typical narrow spectra measured from octanethiol-capped Si nanocrystals. Spectra determined to originate from individual nanocrystals did not show measurable spectral diffusion (Figure 4.1B inset), suggesting that these organic-capped Si nanocrystals are stable against degradation in air. With excitation at 488 nm, the emission peak maxima shift through the visible, from ~525 nm up to ~700 nm. Due to experimental constraints, excitation wavelengths shorter than 488 nm were not accessible, however, the ensemble spectra clearly show that blue emission results from particles on the small end of the size distribution. Silicon can be made to emit visible light across all frequencies in the visible spectrum by tuning the particle size. This is rather remarkable, given that the bulk band gap of Si is in the near-IR at 1.1 eV.

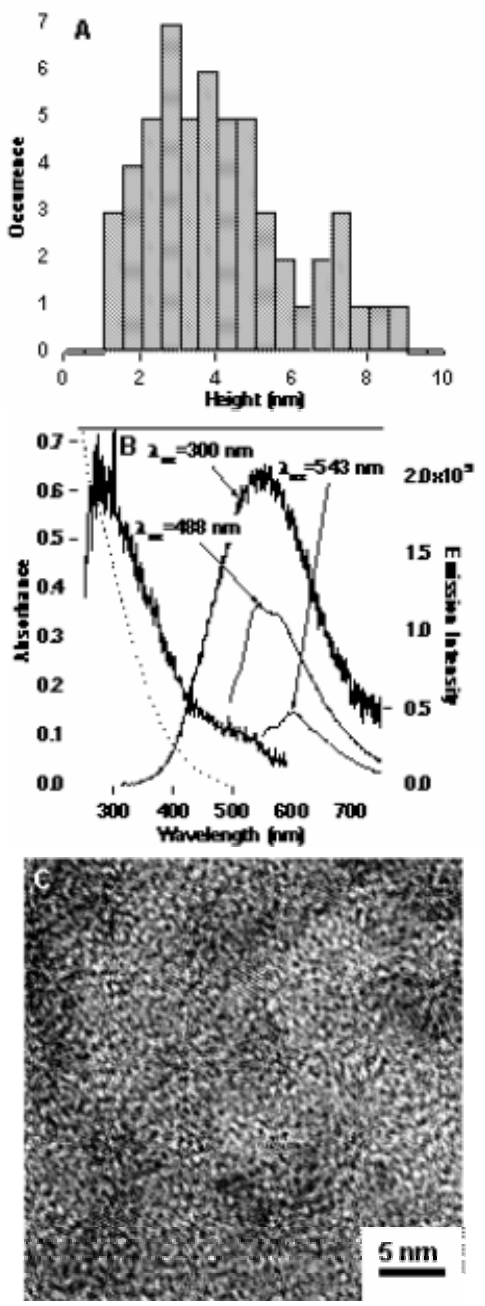

Figure 4.2 (A) AFM histogram showing the nanocrystal height distribution. (B) Room temperature absorbance, PLE and PL spectra for the ensemble. (C) TEM of silicon nanocrystals reveals the internal crystallinity of several dots.

4.3.2 Radiative Rate

4.3.2.1 Ensemble Lifetime Measurement

Microsecond scale PL lifetimes, observed previously in por-Si[5] and oxide capped Si nanocrystals,[16] were not detected in our sample using a fluorometer equipped with microsecond resolution. Approximately 98±2% of the total PL exhibit a lifetime ≤ 20 ns. Figure 4.3A shows the time-resolved decay of the PL of the Si nanocrystals dispersed in chloroform. It was necessary to implement three exponentials to fit the data:

$$I(t) = A_1 e^{-t/\tau_1} + A_2 e^{-t/\tau_2} + A_3 e^{-t/\tau_3} \qquad (4.1)$$

where $I(t)$ is the measured PL intensity as a function of time, t, after the excitation pulse. Table 4.1 lists the fitted constants, $A_1, A_2, A_3, \tau_1, \tau_2, \tau_3$, as a function of detection wavelength. The octanethiol-capped Si nanocrystals examined here exhibit characteristic lifetimes with a fast component (~300 ps), and two slow components with lifetimes ranging from 2 to 6 ns—at least 3 orders of magnitude faster than those previously found for por-Si and Si nanocrystals. Although the lifetimes of por-Si are characteristically orders of magnitude shorter than those of bulk Si (giving rise to relatively efficient PL) they are nonetheless characteristic of an indirect band gap transition.

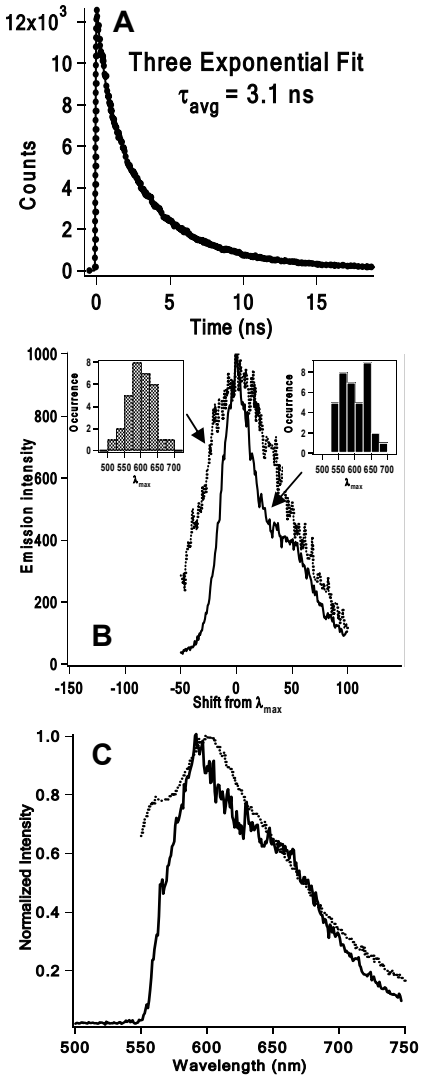

Figure 4.3 (A) Average room temperature lifetime measurement of the ensemble. (B) Observation of "molecular" (—) and "continuum" (----) like single nanocrystal spectra. Average of 37 molecular type spectra and 31 continuum type spectra from single nanoparticles excited at 488 nm. Each spectra was shifted so that its maximum was at zero before averaging. Histogram insets of spectral maxima (λ_{max}) of continuum type and molecular type spectra, respectively. (C) Comparison of the measured ensemble spectra (----) to the reconstructed ensemble spectra reconstructed from the single dot spectra (—) of 68 individual silicon nanoparticles.

Table 4.1 Summary of fluorescence lifetime measurements on Si nanocrystal dispersions. The fluorescence decay curves were fit with three exponential functions: $I(t) = A_1 e^{-t/\tau_1} + A_2 e^{-t/\tau_2} + A_3 e^{-t/\tau_3}$

Emission Wavelength (nm)	τ_1 (ns)	A_1 (%)	τ_2 (ns)	A_2 (%)	τ_3 (ns)	A_3 (%)
520	0.27	31	2.2	46	5.7	23
560	0.33	29	2.3	46	6.0	25
600	0.37	27	2.3	47	6.2	26
640	0.39	28	2.3	47	6.4	25
680	0.42	30	2.2	46	6.3	24

4.3.2.2 Quantum Yield

The measured lifetime relates to the radiative and non-radiative electron-hole recombination processes. The radiative rate, k_r, is related to the fluorescence quantum yield, ϕ, which is the number of photons emitted divided by the total photons absorbed, as $k_r = \phi/\tau$. For the nanocrystals studied by scanning confocal microscopy, ensemble measurements give $\phi = 5.5\%$. The fluorescence quantum yield of Si nanocrystals dispersed in chloroform was measured relative to Rhodamine 6G in ethanol (QY=95%) using 488 nm excitation on a fluorometer (SPEX) in a right-angle geometry. The absorbance of both Si suspension and R6G solution at 488 nm were adjusted to ~ 0.06. The fluorescence spectra were corrected for detector response.

4.3.2.3 Mechanism of Emission

As we are interested in determining the slowest radiative process in the nanocrystals for comparison with por-Si, radiatve rate can be calculated by taking an average lifetime of 4 ns: $k_r \cong 10^7\ \mathrm{s}^{-1}$. A radiative rate constant of this order suggests that emission in these Si nanocrystals originates from an optically allowed transition. The radiative rates are only about two times slower than those measured for phosphine-coated CdSe nanocrystals at room temperature, which are naturally expected to exhibit an allowed optical transition given the direct band gap in the bulk. Using the relation, $\phi = k_r/(k_r + k_{nr})$, to calculate the non-radiative rate, $k_{nr} \cong 2\times10^8\ \mathrm{s}^{-1}$, it is clear that the non-radiative rate processes in the nanocrystals are also very fast. These efficient recombination processes lead to the observed nanosecond scale PL lifetimes and result from strong coupling of excited core states with either phonons or surface states, or a combination of both (see discussion of both).

The non-radiative recombination rate in CdSe at room temperature was also found to be similar to the values measured for these Si nanocrystals. It is worth noting that the non-radiative rates in CdSe have been significantly reduced in certain cases by coating the nanocrystals with a different wider band gap semiconductor, such as CdS or ZnS, which has a small lattice mismatch and effectively eliminates dangling bonds on the nanocrystal surface.[17] This surface

coating results in enhanced PL quantum yields, but does not affect the radiative rate.

One significant difference between the single nanocrystal PL spectra of Si nanocrystals compared to CdSe nanocrystals was observed in this study. Approximately half the spectra determined to originate from individual nanocrystals exhibited vibronic-like activity at room temperature. In these spectra, the peaks are split by 1075 ± 169 cm^{-1}, which agrees reasonably well with literature values for the Si-O-Si stretching frequency.[18] The average of these vibronic-like spectra are displayed in Figure 4.3B, along with the average of the remaining spectra, which show a broader and symmetric shape with an average line width of 1596 ± 502 cm^{-1}. Perhaps this indicates that two nanocrystal subpopulations exist in these samples—one that exhibits molecular-like optical properties and the other that exhibits continuum-like properties. It is well-known that the surface chemistry can greatly affect the nature of light emission from Si nanostructures,[5] and perhaps subtle differences in surface chemistry or surface structure give rise to these observed differences in PL. The observation of an Si-O-Si vibrational feature in single dot PL suggests that the exciton is strongly coupled to this vibrational mode, implying a resonant mixing of the quantum confined core states with localized shallow surface states.[19] The internal core state can borrow oscillator strength from the dipole allowed surface states, leading to the enhancement of the band edge transition probability in the Si nanocrystal.

The local vibrational mode related to surface sites manifests itself in the light emission. An alternative explanation is that the observed nanosecond scale PL originates from emitting oxygen-related surface states which can trap excitons.

As a last check to ensure that the single nanocrystal spectra presented in this study indeed represent the ensemble, the bulk PL spectrum was reconstructed by combining the spectra of individual nanocrystals. The ensemble spectra appear very similar to the reconstructed spectra, as shown in Figure 4.3C.

4.4 Conclusions

Organic monolayer stabilized Si nanocrystals can be synthesized to yield efficient visible light emission tunable by size. Light emission originates on a time scale consistent with a dipole allowed optical transition, even in particles as large as ~65 Å in diameter. It is our assertion that the dipole allowed transition is a result of strong coupling between the core and surface states. It is anticipated that low temperature studies will determine whether the efficient light emission results from the onset of a direct gap transition. Similar to other nanocrystal materials and molecular systems, fluorescence intermittency is observed. In contrast to the direct band gap semiconductors, such as CdSe and InAs, the theoretical underpinnings of many observations presented here are not well developed. Therefore, these experiments and future examinations of Si nanocrystal optical and electronic properties will benefit greatly from future theoretical work focused on understanding the electronic structure and optical

properties of Si nanostructures. Although much synthetic and analytical work remains to be completed in order to completely understand the physical properties of nanoscale Si, the observations presented here clearly illustrate that Si has an untapped potential as a light emitter for future technological applications. Many fundamental obstacles, however, remain to be overcome. Although the photoemission from the nanocrystals was relatively stable, irreversible bleaching does occur. The non-radiative electron-hole recombination rates are very fast and reduce the fluorescence quantum yield. As for CdSe nanocrystals, continued advances in chemical preparation will bring the materials closer to Si-based optoelectronic applications.

4.5 References

(1) Iyer, S. S.; Xie, Y. H. *Science* **1993**, *260*, 40-46.

(2) Canham, L. T. *Appl. Phys. Lett.* **1990**, *57*, 1046-1048.

(3) Cullis, A. G.; Canham, L. T.; Calcott, P. D. J. *J. Appl. Phys.* **1997**, *82*, 909-965.

(4) Holmes, J. D.; Ziegler, K. J.; Doty, R. C.; Pell, L. E.; Johnston, K. P.; Korgel, B. A. *J. Am. Chem. Soc.* **2001**, *123*, 3743-3748.

(5) Wolkin, M. V.; Jorne, J.; Fauchet, P. M.; Allan, G.; Delerue, C. *Phys. Rev. Lett.* **1999**, *82*, 197-200.

(6) Kovalev, D.; Heckler, H.; Ben-Chorin, M.; Polisski, G.; Schwartzkopff, M.; Koch, F. *Phys. Rev. Lett.* **1998**, *81*, 2803-2806.

(7) Brus, L. E.; Szajowski, P. F.; Wilson, W. L.; Harris, T. D.; Schuppler, S.; Citrin, P. H. *J. Am. Chem. Soc.* **1995**, *117*, 2915-2922.

(8) Wilson, W. L.; Szajowski, P. F.; Brus, L. E. *Science* **1993**, *262*, 1242-1244.

(9) Mason, M. D.; Credo, G. M.; Weston, K. D.; Buratto, S. K. *Phys. Rev. Lett.* **1998**, *80*, 5405-5408.

(10) Ge, G. L.; Brus, L. E. *Nano Lett.* **2001**, *1*, 219-222.

(11) Nirmal, M.; Dabbousi, B. O.; Bawendi, M. G.; Macklin, J. J.; Trautman, J. K.; Harris, T. D.; Brus, L. E. *Nature* **1996**, *383*, 802-804.

(12) Kuno, M.; Fromm, D. P.; Gallagher, A.; Nesbitt, D. J.; Micic, O. I.; Nozik, A. J. *Nano Lett.* **2001**, *1*, 557-564.

(13) Banin, U.; Bruchez, M.; Alivisatos, A. P.; Ha, T.; Weiss, S.; Chemla, D. S. *J. Chem. Phys.* **1999**, *110*, 1195-1201.

(14) Efros, A. L.; Rosen, M. *Phys. Rev. Lett.* **1997**, *78*, 1110-1113.

(15) Krauss, T. D.; Brus, L. E. *Phys. Rev. Lett.* **1999**, *83*, 4840-4843.

(16) Germanenko, I. N.; Li, S. T.; El-Shall, M. S. *J. Phys. Chem. B* **2001**, *105*, 59-66.

(17) Hines, M. A.; GnyotSionnest, P. *J. Phys. Chem.* **1996**, *100*, 468-471.

(18) Dubin, V. M.; Ozanam, F.; Chazalviel, J. N. *Phys. Rev. B* **1994**, *50*, 14867-14880.

(19) Bawendi, M. G.; Carroll, P. J.; Wilson, W. L.; Brus, L. E. *J. Chem. Phys.* **1992**, *96*, 946-954.

Chapter 5: Synthesis and Crystallization of Amorphous Silicon Colloids

5.1 Introduction

Amorphous silicon has received much attention due to its potential uses in solar cells and optoelectronic devices. Hydrogenated amorphous silicon films can be deposited by CVD, hot filament CVD and RF sputtering and have excellent electrical quality and possess better transparency in the near IR and than pure amorphous silicon[1,2] which can be formed by a simpler processing step of ion irradiation of crystalline silicon; these films have greater thermal stability.[1,3] A less explored area is that of colloidal amorphous silicon. Submicron structures of pure or hydrogenated silicon could have potential uses in many areas. Incorporation of a-Si particles into polymer matrices to form a polymer nanocomposite with enhanced mechanical,[4-6] optical[4,6-8] and electrical[6,9-11] properties is one such application. An a-Si nanocomposite would have a high refractive index that could help bridge the index gap between organic/inorganic interfaces thus improving the optical-coupling efficiencies of photonic devices.[6,12] While the synthesis of submicron particles of such materials as polystyrene (PS),[13-16] SiO_2[17-19] and TiO_2[19-22] has been well reported, the refractive index of these materials is low compared with that of amorphous silicon ($n_{PS} = 1.59$; $n_{SiO2} = 1.4$; $n_{TiO2} = 2.5$; $n_{a\text{-}Si} > 3.7$).[1,6,23-25] High refractive index materials have another

very useful application which researchers have been studying intensely and that is the production of a 3D photonic crystal for control over the flow of light at visible wavelengths.[26] Such photonic crystals have been produced with a complete photonic band gap in the infrared,[27-30] but a complete photonic band gap in the visible wavelengths is desired. The material characteristics for the production of a 3D photonic crystal are quite strict such that the structure must be very porous (80%) and have a specific lattice symmetry.[31-33] The latter requirement will only be met with particles having a very small size distribution. As stated earlier, a high refractive index material is required, one with $n > 2.8$ and it must also have a negligible absorption at optical wavelengths.[31,34,35] Taking all factors into consideration, there are several high refractive index semiconductors with low absorption which include GaP, Se, GaAs, InP, Si, Ge and Te. Previous work in this area has utilized these materials in inverse opals where a low refractive index, highly monodisperse system of particles (such as polystyrene or SiO_2) formed a colloidal crystal.[26,31,36-38] A high refractive index material was deposited/inserted into the interstitial spaces of the colloidal crystal by sintering,[26,39,40] electrodeposition,[37] chemical vapor deposition[36,41] or oxide reduction.[38] The low refractive index material was subsequently removed leaving a porous matrix (inverse opal structure) of high refractive index material. These techniques, while innovative, are challenging to yield complete infiltration of the semiconductor into the matrix.[31]

The use of high refractive index materials as opals in the search for a 3D photonic crystal has not been explored due to the unavailability of colloidal dispersions of high refractive index materials. A novel synthesis of a high refractive index material is now reported. Amorphous silicon colloids can be formed via the decomposition of trisilane in supercritical hexane. Four factors were varied in the synthesis of these colloids: precursor concentration, temperature, pressure and time. Particles sizes range from 60-450 nm with dispersities between 10-30%.

5.2 Experimental Section

5.2.1 Particle Formation

Trisilane and anhydrous hexane were obtained from Voltaix, Inc. (North Branch, NJ) and Aldrich Chemical Co. (St. Louis, MO), respectively and were stored in a nitrogen glove box. Amorphous silicon particles were prepared by thermally degrading trisilane in the presence of supercritical hexane (T_c=235°C; P_c=30 bar) in a high pressure titanium batch reactor (inner volume 10 mL). Concentration, temperature, pressure and reaction length were studied through a design of experiments (see Section 5.3) to determine their effects on particle formation and size. Reaction temperature was reached by insertion of the titanium reactor into a brass block heated by cartridge heaters. Upon reaction completion, the titanium reactor was cooled in an ice bath and the product was

then extracted with hexane. The extract was centrifuged at 9000 rpm for 10 minutes and the cleaned precipitate was collected for analysis. Upon mild sonication, the precipitate redispersed in hexane or chloroform to form a cloudy solution.

5.2.2 Characterization

Amorphous silicon particles were characterized using various techniques. High-resolution scanning electron microscopy (HRSEM) was performed using a LEO 1530 operating at 7 kV. High-resolution transmission electron microscopy (HRTEM) images were obtained using a JEOL 2010F electron microscope operating at 200 kV. HRTEM samples were prepared by drop casting hexane or chloroform dispersed particles on carbon-coated 200 mesh Cu grids (Electron Microscope Sciences). X-ray diffraction (XRD) spectra were collected with a Bruker-Nonius D8 Advance Theta-2Theta Powder Diffractometer, with Cu Kα radiation and a scintillation detector. Thermal analysis of the particles was performed on a Perkin-Elmer Series 7 differential thermal analyzer (DTA). The sample was contained in an alumina crucible and heating occurred under a 20 mL/min nitrogen purge. FTIR spectra were collected on a Nicolet Magna-IR Spectrometer 550; amorphous silicon was characterized in a KBr pellet against a blank. Annealing experiments were performed using a Denton Vacuum Chamber Evaporator (DV-502A) between 2-4 x 10^{-6} torr. Amorphous silicon samples were

drop cast into flat bottomed molybdenum boats (0.005" thick) (purchased from Midwest Tungsten Service) and subjected to currents between 50 and 100 amperes. The relationship between substrate temperature and applied current was determined using an IRCON Series R Infrared thermometer. Temperature measurements were made on a pure aluminum standard in the molybdenum boat at 5 amp intervals from 40 - 100 amps; emissivity was set at 0.35. HRSEM and XRD were performed on the annealed samples in the molybdenum boats, while HRTEM was performed on the redispersed particles.

5.3 Results and Discussion

5.3.1 Mechanism

The gaseous decomposition of silanes can optimally be described by the reaction

$$Si_nH_{2n+2} \rightarrow nSi + (n+1)H_2 \qquad (5.1)$$

This reaction generally does not go to completion due to experimental conditions. The solid product formed by the pyrolysis of silanes is increasingly hydrogenated with decreasing reaction temperature.[42] Pyrolysis at low pressures is dominated by heterogeneous reaction stages[43,44] while at high pressure the homogeneous elementary reactions prevail resulting in aerosol particles.[42,45] The stages of aerosol formation in the pyrolysis of silanes are nucleation, growth of particles by condensation and coagulation and agglomerate formation comprised of individual

particles.[42] Based upon silane, disilane and trisilane heterogeneous decomposition rates, a scheme for aerosol particle formation has been proposed as

$$SiH_4 \rightarrow \overset{polysilanes}{Si_nH_{2n+2}} \rightarrow \overset{aerosol\cdot precursors}{Si_nH_{\alpha n}} \rightarrow aerosol \cdot particles \qquad (5.2)$$

where $\alpha \leq 2$. The decrease in hydrogen content in the particles with increasing silane conversion is related to hydrogen evolution from aerosol particles. Additionally, at long reaction times the main contribution to growth is from hydrogen depleted intermediates.[43] The mechanism of aerosol formation via homogeneous nucleation has been proposed as

$$Si_{m+l}H_{2(n+k)} \leftrightarrow Si_mH_{2n} + Si_lH_{2k} \qquad (5.3)$$

where the forward reaction is the decay of larger clusters and the reverse reaction describes the agglomeration of clusters. Decomposition is small for clusters of m>10 which are regarded as particles. The rate of formation of clusters m>10 is equated to the rate of nucleation.[46] The rate of particle growth is primarily determined by coagulation.[47] Aerosol particles formed via pyrolysis of silanes at low temperatures (550-727°C) are amorphous while particles formed at temperatures greater than 927°C are crystalline.[43] Under supercritical fluid decomposition however, trisilane decomposes to form amorphous silicon via a contrasting mechanism: the heterogeneous insertion of trisilane at the H-terminated silicon surface. Figure 5.1A shows a TEM image of amorphous silicon particles formed in supercritical hexane under the following conditions:

[Si_3H_8] 10 mM; 276 bar; 500°C; 10 min. Calculation of product yield is dependent on the degree of hydrogenation. FTIR spectra exhibit a very small Si-H stretch at 2100 cm^{-1} indicating a residual amount of hydrogen (Figure 5.1B); therefore, yields of 93.7 and 91.9% are reported for 0 and 20% hydrogenation, respectively.

5.3.2 Design of Experiments

Concentration (a), temperature (b), pressure (c) and reaction length (d) were varied in the synthesis of amorphous silicon particles. These four factors were investigated at two levels making a 2^4 factorial experiment. Concentration was studied at 1 mM and 10 mM, temperature at 400°C and 500°C, pressure at 276 bar and 345 bar and reaction length at 10 and 20 minutes. Sixteen total experiments were run and analyzed quantitatively against particle diameter and subjectively against particle formation. Samples were rated 1-4 (poor-excellent) on particle formation based on spherical shape and good particle to particle separation, thus subjectively converting the qualitative formation characteristic into a quantitative response. Table 5.1 lists the experiments preformed, their design of experiments (DOE) identification and their diameter and formation values. The DOE identification is used to delineate whether the factors were used at a high or low level. For instance, sample VII is identified as ***ac*** which indicates a high level of concentration (10 mM) and pressure (345 bar) and a low level of temperature (400°C) and reaction length (10 min) to describe this reaction.

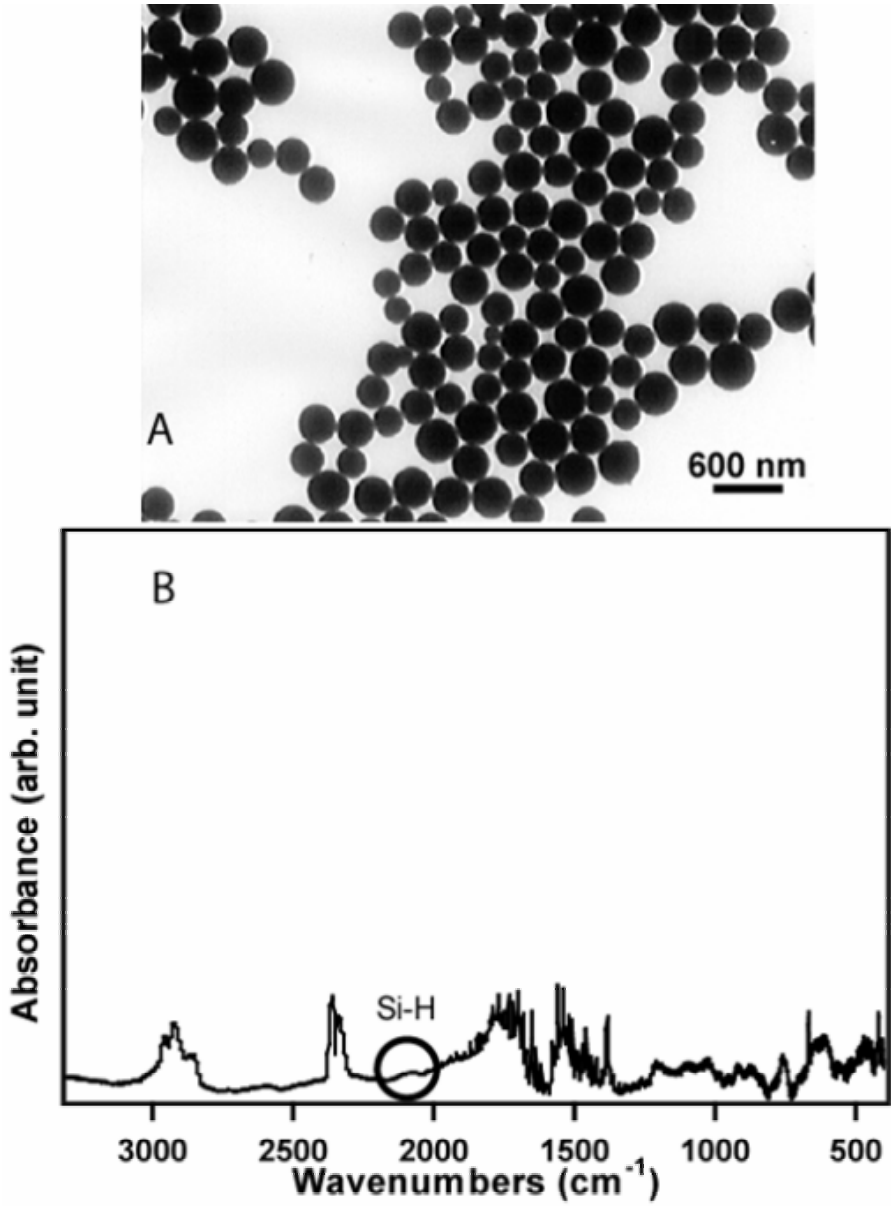

Figure 5.1 (A) Sample VII of amorphous silicon particles formed via trisilane decomposition in supercritical hexane. Experimental conditions: [Si3H8] 10 mM; 276 bar; 500°C; 10 min. (B) FTIR of sample VII exhibiting a small Si-H stretch.

Table 5.1 Design of Experiments Identification and Variables

Sample	DOE Identifier	Diameter (nm)	Formation
I	1	84	1
II	a	194	2
III	b	172.6	1
IV	c	58.8	4
V	d	51.9	1
VI	ab	167.4	3
VII	ac	257.3	4
VIII	ad	197	3
IX	bc	430	3
X	bd	134.2	1
XI	cd	74.4	4
XII	abc	334.6	4
XIII	abd	177	2
XIV	acd	285	3
XV	bcd	160.7	2
XVI	abcd	265.5	3

The following is a brief background on terminology and design of experiments. Variables (y) are the measured response such as yield or in this case, diameter and formation. Factors, usually labeled A, B, C…, are what affect the variables. A *main effect* is a factor considered alone while an *interaction* is a combination of factors. Degrees of freedom (DF) for a set of experiments is defined as *n-1,* where *n* is the number of independent variables. In our case of a full factorial where 16 experiments were run out of a possible 16 experiments, *n*=16. Degrees of freedom for a main effect (A) is defined as *a-1* where *a* is the number of levels considered for effect A. For interaction AB the degrees of freedom is *(a-1)(b-1).* For simplicity, the following terms are defined for a 2 factor experiment. The sum of squares (SS) for factor A and B are

$$SS_A = \frac{1}{bn}\sum_{i=1}^{a} y_{i..}^2 - \frac{y_{...}^2}{abn} \tag{5.4}$$

$$SS_B = \frac{1}{an}\sum_{j=1}^{b} y_{.j.}^2 - \frac{y_{...}^2}{abn} \tag{5.5}$$

The sum of squares for the AB interaction, total sum of squares and sum of squares for error are

$$SS_{AB} = \left[\frac{1}{n}\sum_{i=1}^{a}\ \sum_{j=1}^{b} y_{ij.}^2 - \frac{y_{...}^2}{abn}\right] - SS_A - SS_B \tag{5.6}$$

$$SS_T = \sum_{i=1}^{a}\sum_{j=1}^{b}\sum_{k=1}^{n} y_{ijk}^2 - \frac{y_{...}^2}{abn} \tag{5.7}$$

$$SS_E = SS_T - SS_A - SS_B - SS_{AB} \tag{5.8}$$

The mean square (MS) for the factors, interactions and error are their individual sum of squares over their degree of freedom. For example, the mean square for effect A is:

$$MS_A = \frac{SS_A}{DF_A} \tag{5.9}$$

F is a sampling distribution based on 2 independent chi-square random variables with *u* and *v* degrees of freedom for the effect and error, respectively:

$$F_{u,v} = \frac{\mathrm{X}_u^2 / u}{\mathrm{X}_v^2 / v} \tag{5.10}$$

F values are tabulated for various distributions. $F_{0.05,u,v}$ returns values of *F* in the 5% of the upper tail of the distribution. Comparison of experimental *F* values to tabulated values determines the significance of effects and interactions. Experimental values greater than tabulated values indicate that the effect is significant to the responses (variables), while experimental values less than tabulated values cannot be considered significant as they do not fall outside the error of the experiment.[48]

Tables 5.2 and 5.3 lists the results of the 2^4 factorial experiment. As all the factors have 1 degree of freedom and the error has 5 degrees of freedom, the *F* values are compared to $F_{0.05,1,5}$ = 6.61. The results of the DOE indicate that

particle diameter is most greatly influenced by the main effects of concentration, temperature and pressure and the two factor interaction of conc*pres. Particle formation is primarily influenced by the main effect of temperature and secondarily by concentration.

Table 5.2 Design of Experiments Results for Diameter

Effect	**DF**	**SS**	**MS**	**F**
conc (A)	1	31612.8	31612.8	9.475
temp (B)	1	29601.2	29601.2	8.872
pres (C)	1	25568.0	25568.0	7.663
time (D)	1	7788.1	7788.1	2.334
conc*temp (AB)	1	989.1	989.1	0.296
conc*pres (AC)	1	23808.5	23808.5	7.136
conc*time (AD)	1	5453.8	5453.8	1.635
temp*pres (BC)	1	9555.1	9555.1	2.864
temp*time (BD)	1	3516.5	3516.5	1.054
pres*time (CD)	1	9091.6	9091.6	2.725
error	5	16681.8	3336.4	

Table 5.3 Design of Experiments Results for Formation

Effect	DF	SS	MS	F
conc (A)	1	3.063	3.063	11.667
temp (B)	1	10.563	10.563	40.238
pres (C)	1	0.563	0.563	2.143
time (D)	1	0.563	0.563	2.143
conc*temp (AB)	1	1.563	1.563	5.952
conc*pres (AC)	1	0.563	0.563	2.143
conc*time (AD)	1	0.063	0.063	0.238
temp*pres (BC)	1	0.563	0.563	2.143
temp*time (BD)	1	0.563	0.563	2.143
pres*time (CD)	1	0.563	0.563	2.143
error	5	1.313	0.263	

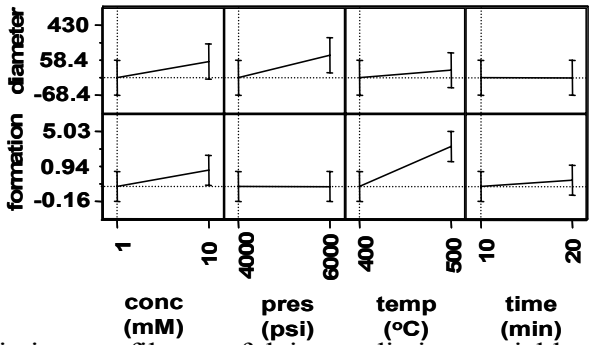

Figure 5.2 Prediction profiler useful in predicting variable responses to factor changes.

From the prediction profiler (Figure 5.2), diameter can be maximized by increasing concentration and pressure or minimized by decreasing concentration and pressure while temperature and time have little effect. Formation is maximized primarily by temperature and secondarily by concentration while pressure and time have little effect. If large, well formed particles are desired, clearly high concentration, pressure and temperature are required. If small, well formed particles are desired, high temperature and pressure and needed but the concentration required is not as clear. Smaller, ill formed particles are favored with lower concentration while larger, well formed particles are favored with higher concentration. There are competing forces in the optimization of size and shape. In order to synthesize small, well formed particles, there must be a trade off with concentration. Another representation of the factor effects on diameter and formation are seen through regression models of the data.

$$X_A = \frac{conc - 5.5}{4.5}; X_B = \frac{temp - 450}{50}; X_C = \frac{pres - 4500}{500}; X_D = \frac{time - 15}{5} \tag{5.11}$$

$$diameter = 190.275 + 44.45X_A + 43.01X_B + 39.975X_C - 22.06X_D + 7.86X_AX_B - 38.575X_AX_C + 18.46X_AX_D + 24.44X_BX_C - 14.825X_BX_D - 23.84X_CX_D \tag{5.12}$$

$$formation = 2.5625 + 0.4375X_A + 0.8125X_B - 0.1875X_C - 0.1875X_D - 0.3125X_AX_B + 0.1875X_AX_C - 0.0625X_AX_D - 0.1875X_BX_C - 0.1875X_BX_D - 0.1875X_CX_D \tag{5.13}$$

5.3.3 Annealing Experiments

Sample XIV, see Table 5.1, was formed under the following conditions: [Si_3H_8] 10 mM; 276 bar; 500°C; 20 min. The product was cleaned as described above; the precipitate was resuspended in chloroform and drop cast into 7 separate molybdenum boats. Sample XIV-a was not subjected to annealing and serves as the control for this experiment. XIV-b through XIV-g were placed in a vacuum evaporator (2-4 10^{-6} torr) and subjected to currents from 50-100 amperes for 1 minute after a 15 second stabilization period. These currents correspond to temperatures of ~ 220-740°C (see Table 5.4).

Table 5.4 Sample XIV Annealing Experiments

Sample	Current (amp)	Temp (°C)	FWHM (degree)	Domain Size (nm)
XIV-a	**0**	**25**	**---**	**---**
XIV-b	**50**	**226**	**---**	**---**
XIV-c	**60**	**482**	**---**	**---**
XIV-d	**70**	**589**	**---**	**---**
XIV-e	**80**	**648**	**0.516**	**17.6**
XIV-f	**90**	**703**	**0.435**	**20.9**
XIV-g	**100**	**743**	**0.212**	**42.9**

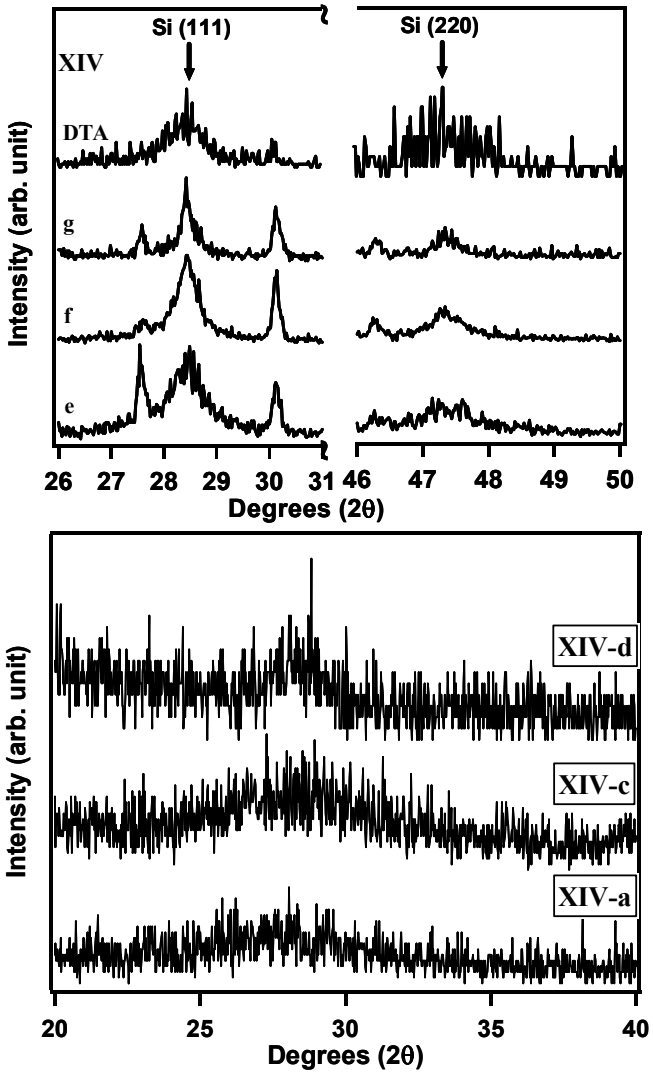

Figure 5.3 XRD spectrum of a-Si samples XIVa,c-g annealed at various temperatures, on a molybdenum substrate, in a vacuum evaporator. Cubic silicon crystalline peaks from XIVe-f are indicated. Unlabeled peaks correspond to the molybdenum substrate and the molybdenum silicon alloy formed during annealling.

Post annealing, the flat bottom of the molybdenum boats was cut out and XRD was performed on the samples directly on the molybdenum substrate. Figure 5.3A displays the selected XRD data for the XIV samples; XIV-b,c,d, annealed at temperatures up to 590°C, show little or no deviation from the amorphous character displayed by the control sample, XIV-a. Rescaling the data for XIV-a and XIV-d in Figure 5.3B exhibits a degree of peak narrowing for the annealed sample which is the beginning of crystallization of the amorphous silicon. XIV-e,f,g, annealed at temperatures between ~650-750°C, exhibit the crystal structure for silicon at 2θ = 28.4° and 47.3° which correspond to Si (111) and (220), respectively. As annealing temperature is increased, there is a distinct narrowing of the Si peaks as shown in Table 5.4. The Si (111) peak narrows from 0.516 to 0.212 degrees over the aforementioned temperature range, corresponding to a large increase in domain size from 25.4 to 168.6 nm. The unlabeled peaks reflected in the Figure 5.3 correspond to the molybdenum substrate and the molybdenum silicon alloy formed during annealing.

Post annealing SEM was performed directly on the molybdenum substrate as well; selected SEM images are shown in Figure 5.4. Figure 5.4A and B show the original sample (drop cast on Mo substrate) and XIV-d (annealed at 590°C) are not dissimilar as is to be expected owing to the amorphous character exhibited by both samples in Figure 5.3. The particles in Figure 5.4A and B appear to be uniform in shape (spherical) and color contrast on the HRSEM.

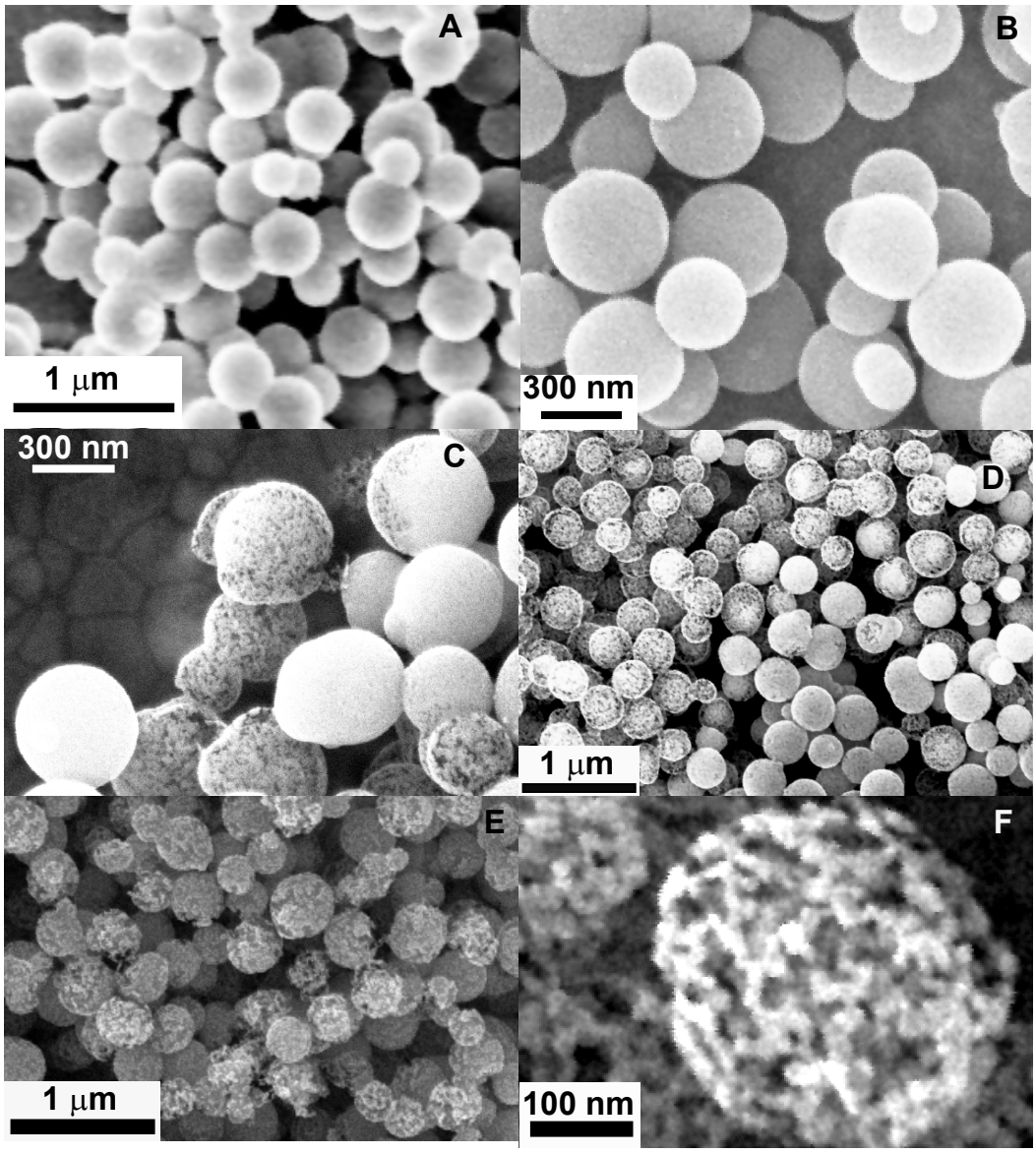

Figure 5.4 HRSEM images of annealed sample XIV. (A) original amorphous sample (XIV-a); (B) amorphous XIV-d annealed at 590°C; (C) XIV-e annealed at 650°C; (D) XIV-f annealed at 700°C; (E) XIV-g annealed at 750°C; (F) XIV-g "broken" particle.

Figure 5.4C and D display particles annealed at 650 and 700°C, respectively; these samples are in an intermediate state where some of the a-Si particles have crystallized while others appear to have retained some amorphous character. The crystalline particles are easily distinguished from amorphous ones by their internal contrast variation. In Figure 5.4C a particle that is one third crystallized can be used to compare the visual difference between crystallized and amorphous silicon. Additionally, in the background of Figure 5.4C, the molybdenum silicon alloy is visible in the shape of molybdenum silicon islands. These structures are not visible in Figure 5.4B which shows only a-Si and the pure molybdenum substrate. XIV-g, annealed at ~750°C, is imaged in Figure 5.4E and F and it can be seen that all the unalloyed silicon has now crystallized. At this temperature, some of the annealed particles fail to retain their original spherical shape and break apart into individual domains as seen in Figure 5.4F.

HRTEM verified that which was observed from XRD and HRSEM; samples XIV-a,b,c,d were comprised solely of amorphous silicon. No crystalline structure was observed in these samples. The indexed lattice structure of samples XIV-e,f,g has shown these samples to also be in agreement with the XRD data; these samples contain crystalline silicon (111) and (220) (the measured d-spacings were 3.13Å and 1.91Å compared with the standard values 3.135Å and 1.92Å). Figure 5.5A,C exhibit the crystalline structure of samples annealed at ~650 and 700°C, respectively. A lower magnification image of the crystallized silicon is

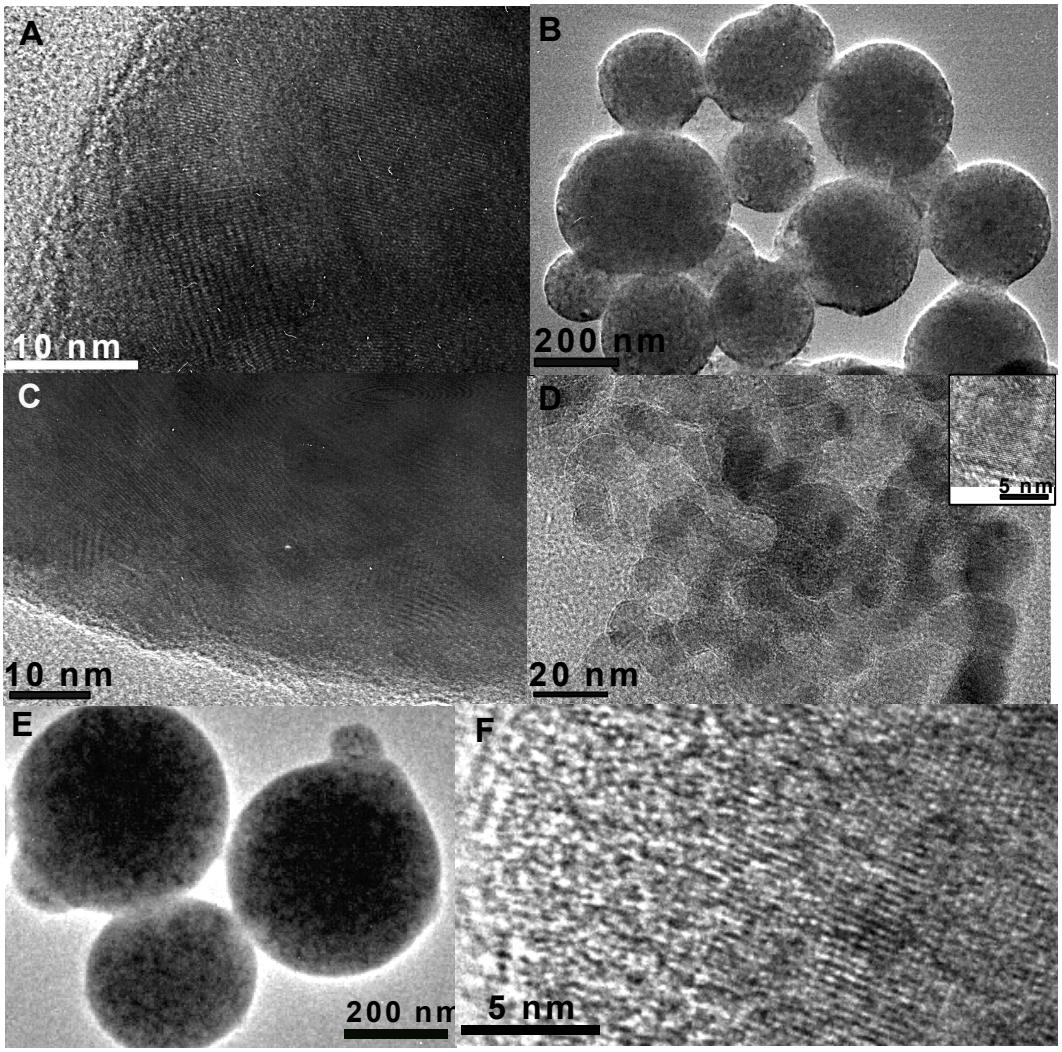

Figure 5.5 HRTEM of annealed XIV. Cubic silicon crystal structure [Si (111) and (220)] is present in XIVe-f and XIV examined by DTA. (A) XIV-e annealed at 650°C; (B),(C) XIV-f annealed at 700°C; (D) "broken" particle from XIV-g annealed at 750°C; (E),(F) XIV annealed in differential thermal analyzer reaching temperatures over 1000°C.

shown in Figure 5.5B. As with the HRSEM images of crystallized silicon, the contrast variation (indicative of crystallinity) can be observed in the HRTEM image. An example of a broken particle, annealed at 750°C, is shown in Figure 5.5D. It should be noted that HRTEM samples were made by washing silicon particles from the molybdenum substrate and drop casting on carbon coated copper grids. HRTEM samples did not contain any molybdenum or molybdenum silicon alloy.

Differential thermal analysis was performed on sample XIV to determine the transition temperature at which the amorphous silicon particles crystallize. The sample was heated under nitrogen purge from room temperature to ~1100°C at a rate of 10 degrees/min. In Figure 5.6 the onset of crystallization occurs at 885°C which is consistent with the approximate temperature of crystallization reported for annealing at short times. Amorphous silicon films annealed in a tube furnace crystallized at 600, 650, 700, 750 and 950°C when annealing times were 6 hr, 1 hr, 10 min, 2 min and 20 sec, respectively[49] and the transition to crystalline form in a-Si whiskers (as measured by DTA) begins at 850°C.[50] HRSEM images of sample XIV annealed in the DTA were similar to the amorphous samples XIVa-d. The particles imaged did not show any contrast variation observed in the aforementioned crystalline samples. However, low magnification TEM images did display the contrast variation (Figure 5.5E) and high resolution images confirmed the crystalline quality of the annealed particles. The particle edge

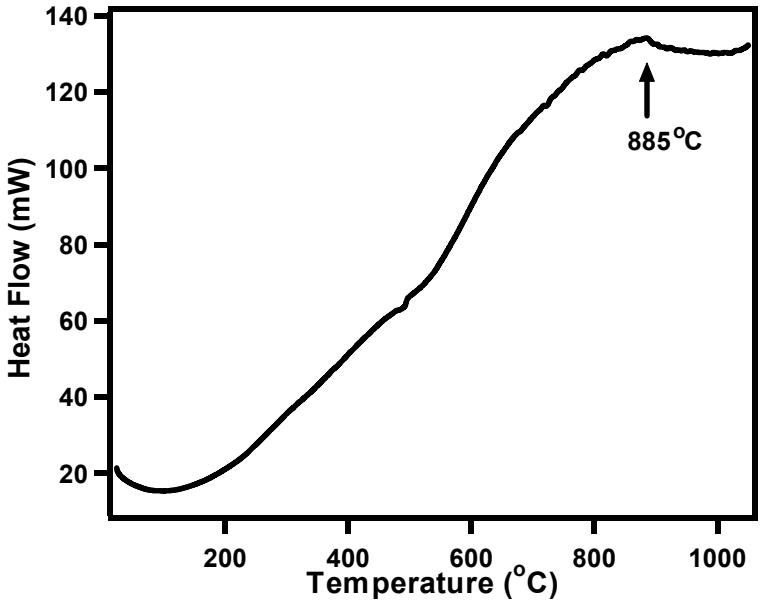

Figure 5.6 Differential thermal analysis scan of XIV sample cycled from 25-1050°C at 10 degrees/min. Transition at 885°C is consistent with crystallization temperature of silicon.

shown in Figure 5.5F was indexed to 3.15Å and 1.92Å corresponding to the (111) and (220) lattice planes of cubic silicon. Also visible in Figure 5.5F is that the edge of the particle appears to be protected by an amorphous layer which may be an oxide layer. Although the sample was annealed under a nitrogen purge, the presence of oxygen cannot be excluded. Compared with the samples annealed in a vacuum evaporator, we see that the DTA product is visually similar, except with regard to the "broken" particles observed in XIV-g which are not present in the DTA annealed sample. One explanation for their presence in XIV-g could be attributed to the sample being under vacuum. If the samples were hydrogenated to some degree and that hydrogen was being aggressively liberated during annealing under vacuum, a "broken" sample could result. Another possible explanation for the effect seen during vacuum annealing could be due to the temperature ramp. The sample was heated in the DTA at a rate of 10 degrees/min while in the vacuum evaporator the sample ramps from room temperature to 750°C in ~ 15 seconds. The sample is not only heated but undergoes a phase transition in this period which may cause the "broken" particle phenomenon.

The crystallization temperature was more than 200°C lower when the sample was annealed on a molybdenum boat rather than in an alumina crucible which is not unexpected. Low temperature crystallization of amorphous silicon can occur in the presence of certain metals. This metal induced crystallization has been reported for Ni,[51,52] Pd,[53] Ge[54] and Al[55] with crystallization temperatures of

$T_{crys,Ni}$ = 650-750°C; $T_{crys,Pd}$ = 550°C; $T_{crys,Ge}$ <500°C; $T_{crys,Al}$ = 350°C. Metal induced crystallization is thought to occur because the metal induces nucleation sites on the silicon surface.

5.4 Conclusions

The first supercritical fluid synthesis of amorphous silicon colloids was presented. Analysis of experimental conditions determined that concentration, temperature and pressure all affect the size of particles formed via the decomposition of trisilane in supercritical hexane. Particle formation, that is shape and separation, is affected primarily by temperature and secondarily by concentration. The crystallization temperature of these particles, as determined by DTA, is 885°C, but the crystallization temperature can be decreased to 650°C by annealing particles on a metal substrate (molybdenum).

5.5 References

(1) de Dood, M. J. A.; Polman, A.; Zijlstra, T.; van der Drift, E. *Journal of Applied Physics* **2002**, *92*, 649-653.

(2) Cocorullo, G.; Corte, F. G. D.; Rendina, I.; Rubino, A.; Terzini, E. *Ieee Photonics Technology Letters* **1996**, *8*, 900-902.

(3) Williamson, D. L.; Roorda, S.; Chicoine, M.; Tabti, R.; Stolk, P. A.; Acco, S.; Saris, F. W. *Applied Physics Letters* **1995**, *67*, 226-228.

(4) Schmidt, H. K. *Macromolecular Symposia* **1996**, *101*, 333-342.

(5) Otooni, M. A. *Materials Research Society Symposium Proceedings* **1995**, *362*, 49-59.

(6) Papadimitrakopoulos, F.; Wisniecki, P.; Bhagwagar, D. E. *Chemistry of Materials* **1997**, *9*, 2928-2933.

(7) Levy, D.; Esquivias, L. *Advanced Materials* **1995**, *7*, 120-129.

(8) Ogawa, T.; Kanemitsu, Y.; Editors *Optical Properties of Low-Dimensional Materials*, 1995.

(9) Clement, R. *ACS Symposium Series* **1995**, *585*, 29-42.

(10) Kanatzidis, M. G.; Wu, C. G.; Marcy, H. O.; Kannewurf, C. R. *Journal of the American Chemical Society* **1989**, *111*, 4139-4141.

(11) Kanatzidis, M. G.; Wu, C. G.; Marcy, H. O.; Degroot, D. C.; Kannewurf, C. R. *Chemistry of Materials* **1990**, *2*, 222-224.

(12) Kitai, A. H.; Editor *Solid State Luminescence: Theory, Materials and Devices*, 1993.

(13) Wang, L. Y.; Lin, Y.-J.; Chiu, W.-Y. *Synthetic Metals* **2001**, *119*, 155-156.

(14) Konno, M.; Motegi, T. *Kemikaru Enjiniyaringu* **1998**, *43*, 914-919.

(15) Paulke, B.-R.; Buske, N.; Winoto-Morbach, S. *Scientific and Clinical Applications of Magnetic Carriers, Proceedings of the International Conference on Scientific and Clinical Applications of Magnetic Carriers, 1st, Rostock, Germany, Sept. 5-7, 1996* **1997**, 69-76.

(16) Margel, S.; Gura, S.; Bamnolker, H.; Nitzan, B.; Tennenbaum, T.; Bar-Toov, B.; Hinz, M.; Seliger, H. *Scientific and Clinical Applications of Magnetic Carriers, Proceedings of the International Conference on Scientific and Clinical Applications of Magnetic Carriers, 1st, Rostock, Germany, Sept. 5-7, 1996* **1997**, 37-51.

(17) Kust, P. R.; Hendel, R. A.; Markowitz, M. A.; Schoen, P. E.; Gaber, B. P. *Colloids and Surfaces, A: Physicochemical and Engineering Aspects* **2000**, *168*, 207-214.

(18) Philipse, A. P. *Colloids and Surfaces, A: Physicochemical and Engineering Aspects* **1993**, *80*, 203-210.

(19) Wang, S. *Huaqiao Daxue Xuebao, Ziran Kexueban* **2002**, *23*, 129-132.

(20) Liu, H.; Yang, W.; Ma, Y.; Cao, Y.; Yao, J.; Zhang, J.; Hu, T. *Langmuir* **2003**, *19*, 3001-3005.

(21) Wang, C.-y.; Liu, C.-y.; Zheng, X.; Chen, J.; Shen, T. *Colloids and Surfaces, A: Physicochemical and Engineering Aspects* **1998**, *131*, 271-280.

(22) Tan, X.; Huang, S.; Zhou, M.; Wang, M. *Gongneng Cailiao Yu Qijian Xuebao* **1998**, *4*, 34-40.

(23) Li, Q. Y.; Dong, P. *Journal of Colloid and Interface Science* **2003**, *261*, 325-329.

(24) Ohata, K.; Yoshihara, T. In *Jpn. Kokai Tokkyo Koho*; (Toppan Printing Co., Ltd., Japan). Jp, 2002, p 9 pp.

(25) Kanai, T.; Sawada, T.; Kitamura, K. *Langmuir* **2003**, *19*, 1984-1986.

(26) Vlasov, Y. A.; Yao, N.; Norris, D. J. *Advanced Materials* **1999**, *11*, 165-169.

(27) Aoki, K.; Miyazaki, H. T.; Hirayama, H.; Inoshita, K.; Baba, T.; Sakoda, K.; Shinya, N.; Aoyagi, Y. *Nature Materials* **2003**, *2*, 117-121.

(28) Hillebrand, R.; Senz, S.; Hergert, W.; Gosele, U. *Journal of Applied Physics* **2003**, *94*, 2758-2760.

(29) Ye, Y.-H.; Mayer, T. S.; Khoo, I.-C.; Divliansky, I. B.; Abrams, N.; Mallouk, T. E. *Journal of Materials Chemistry* **2002**, *12*, 3637-3639.

(30) Bottger, G.; Liguda, C.; Schmidt, M.; Eich, M. *Applied Physics Letters* **2002**, *81*, 2517-2519.

(31) Norris, D. J.; Vlasov, Y. A. *Advanced Materials* **2001**, *13*, 371-376.

(32) Yablonovitch, E. *Physical Review Letters* **1987**, *58*, 2059-2062.

(33) John, S. *Physical Review Letters* **1987**, *58*, 2486-2489.

(34) Busch, K.; John, S. *Physical Review E* **1998**, *58*, 3896-3908.

(35) Sozuer, H. S.; Haus, J. W.; Inguva, R. *Physical Review B* **1992**, *45*, 13962-13972.

(36) Blanco, A.; Chomski, E.; Grabtchak, S.; Ibisate, M.; John, S.; Leonard, S. W.; Lopez, C.; Meseguer, F.; Miguez, H.; Mondia, J. P.; Ozin, G. A.; Toader, O.; van Driel, H. M. *Nature* **2000**, *405*, 437-440.

(37) Braun, P. V.; Wiltzius, P. *Nature* **1999**, *402*, 603-604.

(38) Miguez, H.; Meseguer, F.; Lopez, C.; Holgado, M.; Andreasen, G.; Mifsud, A.; Fornes, V. *Langmuir* **2000**, *16*, 4405-4408.

(39) Velev, O. D.; Tessier, P. M.; Lenhoff, A. M.; Kaler, E. W. *Nature* **1999**, *401*, 548-548.

(40) Velev, O. D.; Kaler, E. W. *Advanced Materials* **2000**, *12*, 531-534.

(41) Chomski, E.; Ozin, G. A. *Advanced Materials* **2000**, *12*, 1071-1078.

(42) Onischuk, A. A.; Panfilov, V. N. *Uspekhi Khimii* **2001**, *70*, 368-381.

(43) Onischuk, A. A.; Strunin, V. P.; Ushakova, M. A.; Panfilov, V. N. *Journal of Aerosol Science* **1997**, *28*, 207-222.

(44) Scott, B. A.; Estes, R. D.; Jasinski, J. M. *Journal of Chemical Physics* **1988**, *89*, 2544-2549.

(45) Slootman, F.; Parent, J. C. *Journal of Aerosol Science* **1994**, *25*, 15-21.

(46) Swihart, M. T.; Girshick, S. L. *Journal of Physical Chemistry B* **1999**, *103*, 64-76.

(47) Onischuk, A. A.; Levykin, A. I.; Strunin, V. P.; Ushakova, M. A.; Samoilova, R. I.; Sabelfeld, K. K.; Panfilov, V. N. *Journal of Aerosol Science* **2000**, *31*, 879-906.

(48) Montgomery, D. C. *Design and Analysis of Experiments*; 4th ed.; John Wiley & Sons, Inc.: New York, 1997.

(49) Wu, M.; Wagner, S. *Applied Surface Science* **2001**, *175-176*, 753-758.

(50) Tatsumi, Y.; Hirata, M.; Yamada, K. *Journal of the Physical Society of Japan* **1981**, *50*, 2288-2294.

(51) Choi, J. H.; Kim, D. Y.; Park, S. J.; Choo, B. K.; Jang, J. *Thin Solid Films* **2003**, *427*, 289-293.

(52) Joshi, A. R.; Saraswat, K. C. *Journal of the Electrochemical Society* **2003**, *150*, G443-G449.

(53) Hu, G.-R.; Huang, T. J.; Wu, Y. S. *Japanese Journal of Applied Physics, Part 2: Letters* **2003**, *42*, L895-L897.

(54) Derakhshandeh, J.; Golshani, N.; Mohajerzadeh, S.; Asl Soleimani, E. *Thin Solid Films* **2003**, *427*, 324-329.

(55) Al-Dhafiri, A. M. *Journal of Saudi Chemical Society* **2002**, *6*, 365-376.

Chapter 6: 2D Reverse Brazil Nut Effect: Long Range Order in Polydisperse Amorphous Silicon Colloids

6.1 Particle Formation and Characterization

Trisilane and anhydrous hexane were obtained from Voltaix, Inc. (North Branch, NJ) and Aldrich Chemical Co. (St. Louis, MO), respectively and were stored in a nitrogen glove box. Amorphous silicon particles were prepared by thermally degrading trisilane (1 mM) in the presence of supercritical hexane (T_c=235°C; P_c=30 bar) in a high pressure titanium batch reactor (inner volume 10 mL). Reaction temperature and pressure (500°C; 276 bar) were reached by insertion of the titanium reactor into a brass block heated via cartridge heaters. Upon reaction completion, the titanium reactor was cooled in an ice bath and the product was then extracted with chloroform. The extract was centrifuged at 9000 rpm for 10 minutes to precipitate any impurities and the supernatant solution was collected for analysis. Amorphous silicon particles were characterized using a high-resolution transmission electron microscopy (HRTEM). Images were obtained using a JEOL 2010F electron microscope operating at 200 kV. HRTEM samples were prepared by drop casting chloroform dispersed particles on carbon-coated 200 mesh Cu grids (Electron Microscope Sciences). Measurement of over 2000 particles resulted in an average diameter of 54 nm and a distribution very similar to that shown in Figure 6.2D.

6.2 Long Range Order

Surface structure can be evaluated using two correlation functions: translational [pair distribution, $g(r)$] and orientational [$g_6(r)$]. The translational correlation function illustrates surface lattice structure by representing particle density as a function of distance, r, from a reference particle. Gray *et al.* simulate 2D random sequential adsorption of tethered hard spheres of varying polydispersity and demonstrate an evolution from disorder to order (hexatic or crystal) with increasing monodispersity through calculation of the translational and orientational correlation functions.[1,2] The Kosterlitz-Thouless-Halperin-Nelson-Young (KTHNY) theory of phase transitions[3-6] was adapted by Gray *et al.* for their symmetrical system of tethered hard spheres with periodic boundary conditions.

For the systems described in this paper (pictured in Figure 6.1), the pair distribution function indicates a disordered lattice which is to be expected for polydisperse systems and therefore it is not shown. One would also expect the orientational correlation function for a polydisperse system to indicate a disordered lattice, but for the systems described herein long range orientational order is observed. The polydisperse formations presented here have size distributions not easily characterized by Gaussian, log normal or Weibull distributions; therefore, histograms of the size distribution for the formations are

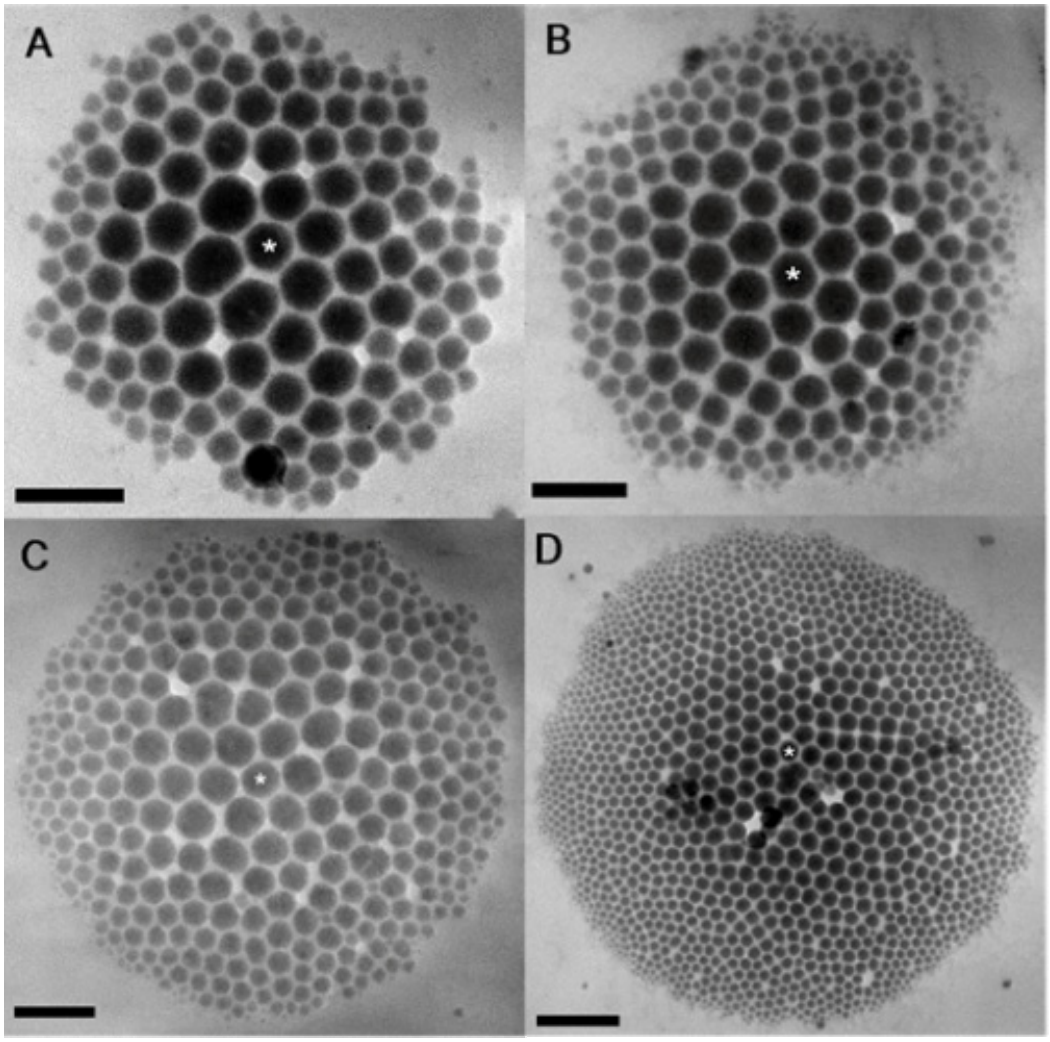

Figure 6.1 HRTEM of ordered amorphous silicon formations. (A), (B), (C) and (D) contain 135, 202, 330 and 1247 particles, respectively. Average particle diameter for formation (A), (B), (C) and (D) are 59.9, 52.4, 50.7 and 53.2 nm, respectively. The asterisk indicates the central reference particle for each formation. Scale bars for (A), (B) and (C) are 200 nm and the scale bar for (D) is 400 nm.

shown in Figure 6.2. These polydisperse formations differ from those presented in simulations by Gray *et al.* in that the formations are of a discrete size (no periodic boundary conditions), the particle mobility is not confined by tethers and the particles are attracted to one another by van der Waals forces. Therefore, the orientational correlation function for the discrete formations presented herein is defined as

$$g_6(r) = \left| \Psi_6{}^*(0)\Psi_6(r) \right| \tag{6.1}$$

which is used to quantify two dimensional surface structure. A complex order parameter, Ψ_6, illustrates the orientation of each particle by measuring its 6-fold symmetry and is multiplied by the complex conjugate of the order parameter (*) for the reference particle (*0*). The modulus of this complex expression yields the orientational order parameter for every particle with respect to one or more reference particles.

$$\Psi_6{}^{(j)} = \frac{1}{z}\sum_k e^{6i\phi_{jk}} \tag{6.2}$$

where z is the number of nearest neighbors for reference particle j and ϕ_{jk} is the orientation angle of the line connecting the center of reference particle j to its

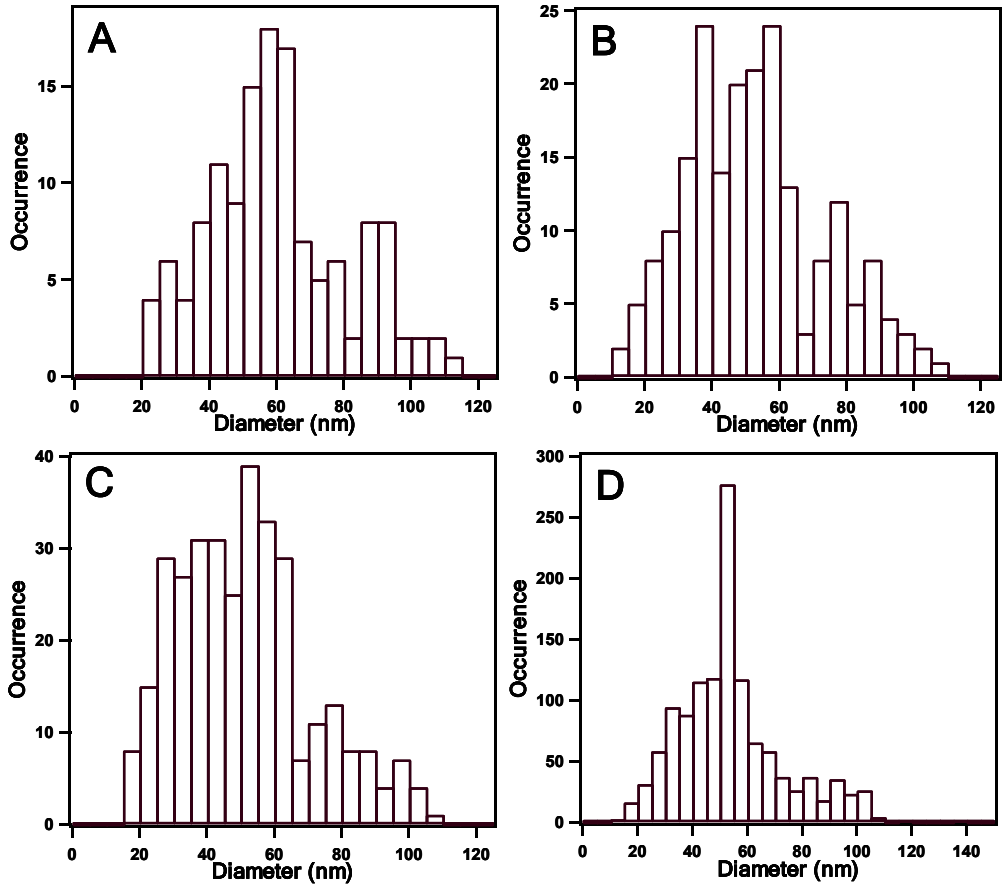

Figure 6.2 Histogram of size distributions for the formations. The polydispersity of the formations do not follow a Gaussian, log normal or Weibull distribution. The distribution for the 2000 plus particles measured for particle sizing is very similar to that found in Figure 2D.

nearest neighbors labeled *k*; a maximum value $\Psi_6 = 1$ occurs when a particle has 6 nearest neighbors each separated by 60°. The complex order parameter can be expressed as

$$\Psi_6^{(j)} = \frac{1}{z}\sum_k \left(\cos 6\phi_{jk} - i\sin 6\phi_{jk}\right) \tag{6.3}$$

and its complex conjugate at reference particle *0* as

$$\Psi_6(0) = \frac{1}{z}\sum_k \left(\cos 6\phi_{0k} + i\sin 6\phi_{0k}\right) \tag{6.4}$$

The orientational correlation function was calculated for the formations in Figure 6.1 through the collection of data such as particle sizes and relative positions. Nearest neighbors could not be explicitly defined as interparticle spacing increased with decreasing diameter due to weakening attractive forces. The average nearest neighbor distance was 3-4 nm; if a potential nearest neighbor candidate was more than double the distance of the particle's other nearest neighbors, the candidate was not included in the calculation. Previously, the orientational correlation function was plotted against r/R_0 where r is some distance expanded radially from the reference particle and R_0 is the average particle diameter.[1] This representation of the orientational correlation function does not make sense for our samples which have such high polydispersity. For the formations discussed herein, the orientational correlation functions (Figure 6.3) are plotted against the center to center distance from the reference particle(s)

to every other particle in the formation. Additionally, $g_6(r)$ was computed using 7 reference particles for formations A, B and C and 1 reference particle for formation D. The central reference particles are indicated in Figure 6.1 by an asterisk and for formations A, B and C the central reference particles 6 nearest neighbors are also considered as reference particles. For a discrete system only the centrally located particles should be used as reference particles because $g_6(r)$ depends on a radial expansion around the reference particles. Particles off center or near an edge would skew results of the orientational correlation function.

The absence of translational order generally implies a lack of orientational order,[1,2] but on inspection the polydisperse formations appear to preserve hexagonal close packing whenever possible even as the particle size decreases radially from the center. Figure 6.3 shows that $g_6(r) \sim$ constant which indicates long range orientational order even in the absence of translational order. The orientational order ends with the discrete boundary of the formation; if an infinitely large size distribution of particles were available, infinite long range orientational is expected.

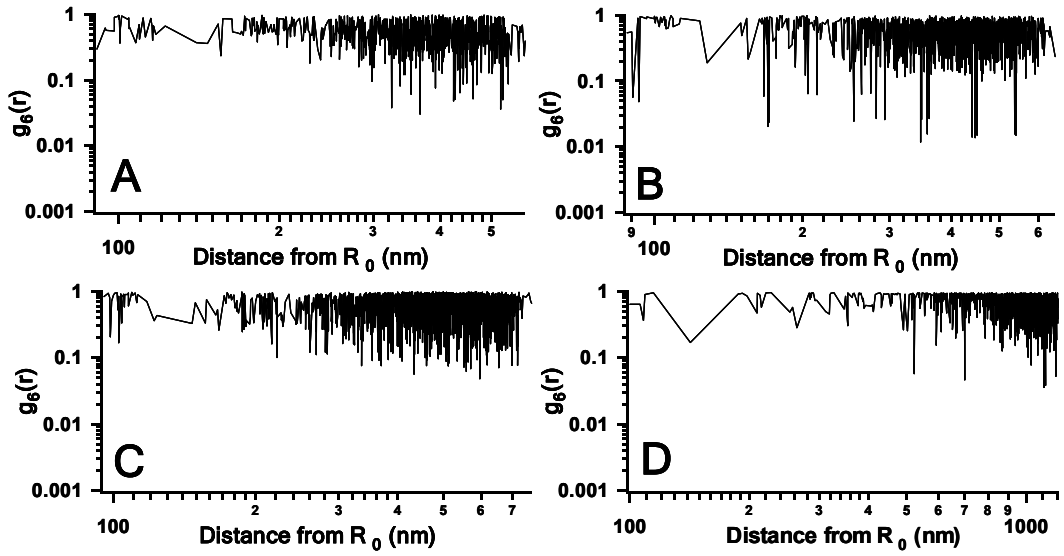

Figure 6.3 Orientational correlation functions for formations. $g_6(r)$ for (A), (B), (C) and (D) were calculated using the central particle indicated by an asterisk (*) and for (A), (B) and (C) the central particle's 6 nearest neighbors were also used as references. The size of formation (D) did not warrant calculations using multiple reference particles. The orientational correlation function is plotted against the distance from the center of the reference particle to the centers of all other particles in the system.

6.3 Particle Arrangement

6.3.1 Diffusion Effects

Particle arrangement during the evaporation of solvent is explored as a function of diffusivity, self-assembly and density (through the Brazil Nut Effect). The mobility of the particles due to diffusion was determined by the Stokes-Einstein equation:

$$D_{AB} = kT / \mu_B 6\pi R_A \tag{6.5}$$

where k is Boltzmann's constant, T is solvent temperature, μ_B is solvent viscosity and R_A is the particle radius. In the polydisperse formations, the particle diameters range from 13 to 136 nm and the diffusion coefficient ranges from 5.86 E-11 to 5.86 E-12 m^2/s, respectively. The lower limit time characteristic for a 200 nm thick film (slightly thicker than the largest particle diameter) to evaporate can be estimated assuming no convection occurs in the gas phase by

$$\tau = \rho l \Delta x / D_{AB} \Delta c \tag{6.6}$$

where ρ is the solvent density, l is the stagnant diffusion film thickness (~0.2 μm), D_{AB} is the diffusion coefficient of solvent in air and Δc is the concentration gradient in the gas phase (9.4 E-4 g/cm^3). The mean square displacement traveled by the particles can be estimated from

$$x = \left(4\pi D_{AB} \tau\right)^{1/2} \tag{6.7}$$

where D_{AB} is the particle diffusion coefficient. For τ = 3.15 E-6 seconds, the mean square displacement is 48 nm and 15 nm for the smallest and largest particles, respectively.[7] The polydisperse formations range in size from 880 – 1950 nm in diameter; therefore, particle mobility cannot solely be explained by diffusion.

6.3.2 Surface Tension and Solvent Flux

Self-assembly of spherical particles in wetting films has been heavily studied in the past two decades.[8-22] For 2D particle assembly in evaporating films there is a two step mechanism consisting of nucleus formation and crystal growth. Ordered assembly in bimodal systems has also been studied. Capillary immersion forces account for nucleus formation; as solvent evaporates from the film, menisci form around the larger particles and the vertical component of the surface tension force presses the particles to the substrate. The larger particles are pushed together to form an ordered nucleus (zone) due to a pressure effect caused by the liquid pressure being lower than the gas phase pressure. The larger particles are immobilized due to friction with the surface while smaller particles remain in the liquid layer. In the crystal growth phase smaller particles are carried toward the nucleus by convection and as the film thickness decreases (due to evaporation) the smaller particles behave similarly to the larger particles in that the surface tension forces press them to the substrate and the smaller particles order themselves

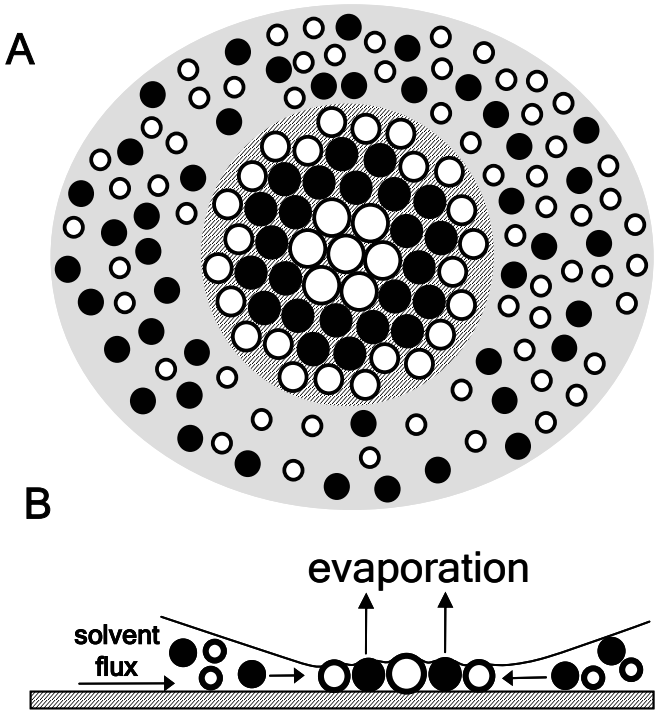

Figure 6.4 Diagram of particle assembly. (A) Top down look at polydisperse order formation. Middle area contains larger particles in hexagonal close packing and hashed area underneath indicates no solvent above the substrate. Gray area is evaporating solvent with smaller particles still floating; as solvent evaporates particles drawn into the nucleus for packing. (B) Side view of particle packing in polydisperse system. Adapted from Langmuir **8**(12) 1992 p.3183.

around the larger particles.[10,14] The same principles apply for polydisperse systems as the previously studied monodisperse or bimodal systems. See Figure 6.4A and B for a cartoon of polydisperse ordering from a top down and side view, respectively.

6.3.3 The Brazil Nut Effect

In the 2D polydisperse formations the larger particles are concentrated in center of the formation at the nucleus and the particle diameter decreases as one moves radially from the nucleus. These formations can be compared to the 3D Brazil nut effect (BNE) where binary mixtures of hard spheres (type A and B) reorganize under agitation. BNE is said to occur when the larger spheres organize at the top and the smaller spheres at the bottom of the box while the reverse Brazil nut effect (RBNE) occurs when the larger spheres organize at the bottom while the smaller spheres organize at the top of the box. Under the appropriate conditions one sphere type condenses while the other sphere type fluidizes. These conditions depend on the critical temperature for A and B sphere types which is calculated as

$$T_c = mgd\mu/\mu_o \tag{6.8}$$

where m is the particle mass, g is gravitational acceleration, d is particle diameter, μ is initial filling height and μ_o is a constant that depends on the spatial dimension and underlying packing structure.[12,23,24] The critical temperature for the sphere

types [$T_c(A)$, $T_c(B)$] is compared to the granular temperature which is proportional to particle velocity by

$$T \propto \frac{1}{N}\sum_i \frac{m_i}{2}\left(v_i - \langle v\rangle\right)^2 \;;\; \langle v\rangle = \frac{1}{N}\sum_i v_i \tag{6.9}$$

where N is the total number of particles, m_i is the mass of the ith particle and v_i is the velocity of the ith particle. If T falls between $T_c(A)$ and $T_c(B)$ then the sphere type whose critical temperature is below T will condense while the sphere type whose critical temperature is above T will remain fluidized.[24] This is referred to as the crossover condition and occurs when the T_c ratio equals the volume ratio for the sphere types which leads to a size versus density relationship applicable to our polydisperse system:

$$\frac{d_l}{d_s} \approx \left(\frac{\rho_l}{\rho_s}\right)^{-1} \tag{6.10}$$

where d_l, d_s, ρ_l and ρ_s are the diameter and mass density of the large and small spheres respectively. BNE is observed when the diameter ratio is smaller than the inverse density ratio, thus the small spheres condense first. RBNE is observed when the diameter ratio is larger, thus the large sphere condense first.[23] For the polydisperse system of amorphous silicon particles the diameter ratio will always be larger than the inverse density ratio as the density ratio will always be unity; therefore, it follows that the larger particles condense first during evaporation. The binary system can be expanded to include many subsets of particle sizes and

in each case the largest particles will condense first followed by the next largest and so forth.

6.4 Conclusions

Long range orientational order in the absence of translational order has been shown for several polydisperse systems of amorphous silicon nanoparticles. These ordered formations can be described as exhibiting a 2D reverse Brazil nut effect whose self assembly is driven by diffusion, density and capillary forces.

6.5 References

(1) Gray, J. J.; Klein, D. H.; Korgel, B. A.; Bonnecaze, R. T. Langmuir 2001, 17, 2317-2328.

(2) Gray, J. J.; Klein, D. H.; Bonnecaze, R. T.; Korgel, B. A. Physical Review Letters 2000, 85, 4430-4433.

(3) Halperin, B. I.; Nelson, D. R. Physical Review Letters 1978, 41, 121-124.

(4) Weber, H.; Marx, D.; Binder, K. Physical Review B 1995, 51, 14636-14651.

(5) Kosterlitz, J. M.; Thouless, D. J. Journal of Physics C: Solid State Physics 1973, 6, 1181-1203.

(6) Young, A. P. Physical Review B 1979, 19, 1855-1866.

(7) Stowell, C.; Korgel, B. A. Nano Letters 2001, 1, 595-600.

(8) Adachi, E.; Dimitrov, A. S.; Nagayama, K. Langmuir 1995, 11, 1057-1060.

(9) Deegan, R. D. Physical Review E 2000, 61, 475-485.

(10) Denkov, N. D.; Velev, O. D.; Kralchevsky, P. A.; Ivanov, I. B.; Yoshimura, H.; Nagayama, K. Langmuir 1992, 8, 3183-3190.

(11) Elbaum, M.; Lipson, S. G. Physical Review Letters 1994, 72, 3562-3565.

(12) Hong, D. C. Physica A 1999, 271, 192-199.

(13) Kralchevsky, P. A.; Paunov, V. N.; Denkov, N. D.; Ivanov, I. B.; Nagayama, K. Journal of Colloid and Interface Science 1993, 155, 420-437.

(14) Kralchevsky, P. A.; Denkov, N. D. Current Opinion in Colloid & Interface Science 2001, 6, 383-401.

(15) Maenosono, S.; Dushkin, C. D.; Saita, S.; Yamaguchi, Y. Langmuir 1999, 15, 957-965.

(16) Nicodemi, M.; Fierro, A.; Coniglio, A. Europhysics Letters 2002, 60, 684-690.

(17) Ohara, P. C.; Heath, J. R.; Gelbart, W. M. Angewandte Chemie-International Edition in English 1997, 36, 1078-&.

(18) Paunov, V. N.; Kralchevsky, P. A.; Denkov, N. D.; Nagayama, K. Journal of Colloid and Interface Science 1993, 157, 100-112.

(19) Petkov, J. T.; Denkov, N. D.; Danov, K. D.; Velev, O. D.; Aust, R.; Durst, F. Journal of Colloid and Interface Science 1995, 172, 147-154.

(20) Thiele, U.; Mertig, M.; Pompe, W. Physical Review Letters 1998, 80, 2869-2872.

(21) Yamaki, M.; Higo, J.; Nagayama, K. Langmuir 1995, 11, 2975-2978.

(22) Velikov, K. P.; Durst, F.; Velev, O. D. Langmuir 1998, 14, 1148-1155.

(23) Breu, A. P. J.; Ensner, H. M.; Kruelle, C. A.; Rehberg, I. Physical Review Letters 2003, 90.

(24) Hong, D. C.; Quinn, P. V.; Luding, S. Physical Review Letters 2001, 86, 3423-3426.

Chapter 7: Conclusions and Recommendations

7.1 Conclusions

7.1.1 Electrochemistry and Electrogenerated Chemiluminescence from Silicon Nanocrystal Quantum Dots

Reversible electrochemical injection of discrete numbers of electrons into sterically stabilized silicon nanocrystals (NCs) (~ 2 to 4 nanometers in diameter) was observed by differential pulse voltammetry (DPV) in *N*,*N*'-dimethylformamide and acetonitrile. The electrochemical gap between the onset of electron injection and hole injection—related to the highest occupied and lowest unoccupied molecular orbitals—grew with decreasing nanocrystal size, and the DPV peak potentials above the onset for electron injection roughly correspond to expected Coulomb blockade or quantized double-layer charging energies.[1] Electron transfer reactions between positively and negatively charged nanocrystals (or between charged nanocrystals and molecular redox-active coreactants) occurred that led to electron and hole annihilation, producing visible light. The electrogenerated chemiluminescence spectra exhibited a peak maximum at 640 nanometers, a significant red shift from the photoluminescence maximum (420 nanometers) of the same silicon NC solution. These results demonstrate that the chemical stability of silicon NCs could enable their use as

redox-active macromolecular species with the combined optical and charging properties of semiconductor quantum dots.

7.1.2 Size Tunable Visible Luminescence from Individual Organic Monolayer Stabilized Silicon Nanocrystal Quantum Dots

Quantum confinement in nanostructured silicon can lead to efficient light emission. However, the photoluminescence (PL) lifetimes in nanostructured silicon are typically very long —approximately three orders of magnitude longer than those of direct band gap semiconductors. It was shown in Chapter 4 that organic monolayer coated silicon nanocrystals ranging from 1 to 10 nm in diameter emit with nanosecond-scale lifetimes and high quantum yields, making it possible to measure the PL spectra of single Si quantum dots. The Si quantum dots demonstrate stochastic single-step "blinking" behavior and size-dependent PL spectra with line widths approximately only three times greater than those measured for CdSe nanocrystals at room temperature.

Although much synthetic and analytical work remains to be completed in order to completely understand the physical properties of nanoscale Si, the observations presented here illustrate that Si has an untapped potential as a light emitter for future technological applications. Many fundamental obstacles, however, remain to be overcome. Although the photoemission from the nanocrystals was relatively stable, irreversible bleaching does occur.

Additionally, the non-radiative electron-hole recombination rates are very fast and reduce the fluorescence quantum yield.

7.1.3 Synthesis and Crystallization of Amorphous Silicon Colloids

A novel synthesis of colloidal amorphous silicon was reported in Chapter5. Submicron amorphous silicon particles were synthesized in high yield (> 90%) via the decomposition of trisilane in supercritical hexane. A thorough analysis of the synthesis was performed using a design of experiments to determine that concentration, temperature and pressure are important effects in the resulting particle size. In the correct proportions these factors can be combined to control particle size, shape and separation. Crystallization of the amorphous silicon particles was carried on molybdenum boats in a vacuum evaporator, at temperatures as low as 650°C. Extensive XRD, SEM and TEM characterized the amorphous and crystalline samples.

7.1.4 2D Reverse Brazil Nut Effect: Long Range Order in Polydisperse Amorphous Silicon Colloids

Self assembly of amorphous silicon colloids produced 2D polydisperse formations exhibiting long range orientational order even in the absence of translational order. Long range order was verified by the hand calculation of the orientational correlation function. Arrangement of particles in the ordered array can be explained primarily by capillary forces and minimally by diffusion.

Additionally, the 2D formations can be compared to the 3D reverse Brazil nut effect.

7.2 Recommendations

7.2.1 Silicon Halide Synthesis Modifications

7.2.1.1 Dual Reactor Apparatus

The synthesis of nanocrystals via the silicon halide synthesis (Chapter 2) is very promising, but is complicated by the corrosive properties of the silicon precursor. This method of nanocrystal fabrication could be significantly improved by two apparatus modifications. To reiterate the issues here, the synthesis needs to be performed in an anhydrous environment and the silicon precursor needs to be injected into the supercritical fluid. One modification that would allow for both of these conditions is a 2-reactor system connected by a 2-way valve (see Figure 7.1). In this design, each reactor would have its own heating element (either brass block or heating tape) and each reactor would contain enough hexane to achieve supercritical conditions at elevated temperatures. One reactor would contain lithium aluminum hydride and the other would contain the silicon halide. Initially the 2-way valve would be closed and once the reactors reached the desired temperature/pressure, the valve would be opened and the contents allowed to mix/react. As the reactors will be filled in the glove box, their contents will not come in contact with air prior to reaction. If the

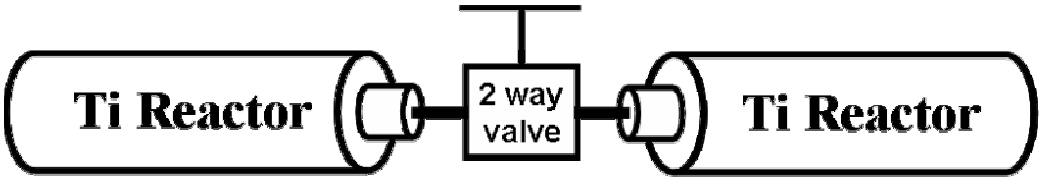

Figure 7.1 Two reactor system connected by a 2-way valve. Apparatus modification for silicon halide synthesis.

reaction is run with excess lithium aluminum hydride the reactors and tubing will be free of corrosion.

7.2.1.2 Nitrogen Box for Injection

Alternatively, the silicon halide synthesis could be improved by a custom nitrogen box or bag built around the 6-way injection valve (see Figure 2.2). If the 6-way valve were encased in an inert environment, the tubing would not corrode upon injection. If a box were built to house the 6-way valve, it would require an inlet gas line and an outlet gas line equipped with a one-way valve such that gas would be expelled above a certain pressure. Additionally, inlet and outlet ports for the high pressure tubing would be required. The tubing in question is 1/16 inch stainless steel; therefore, well secured septa could be used to feed the tubing in and out of the box. As the intention of this modification is to prevent air exposure to the precursor during injection, the injection port must be enclosed in the nitrogen box. Access to the injection port could also be through a septum. If

done correctly, this modification should prevent corrosion by eliminating precursor exposure to air during injection.

7.2.2 Sonochemistry

The chemical effects of ultrasound include improvements in stoichiometric and catalytic reactions and can increase reactivities by almost a million-fold through the process of acoustic cavitation. This formation, growth and implosive collapse of bubbles in a liquid causes localized hot spots with temperatures in the range of 5000°C, pressures approaching 500 atmospheres, lifetimes of a few microseconds, and heating and cooling rates greater than 10^9 K/s.[2]

Sonochemistry syntheses of nanocrystals such as CdSe, CdS, Fe, Ge and Si have received some attention in the last five years.[3-8] Use of an ultrasonic probe allows for low temperature, bench top syntheses while the reaction takes place in the high temperature, high pressure bubbles caused by cavitation. Our laboratory attempts to reproduce the bench top Fe and Si nanocrystal sonochemistry syntheses have failed to yield crystalline particles. The syntheses appear to be very sensitive to sonication conditions and it is believed that intermediate gases, produced during sonication, escaped before crystal formation.

Although bench top, ultrasonic syntheses have not been fruitful, supercritical ultrasonication holds much promise. The supercritical reactions discussed in Chapter 2 suffer from disadvantages which differ by precursor. The

diphenylsilane synthesis produces particles in low yield while the monophenylsilane and trisilane reactions produce amorphous silicon particles. The silicon halide reaction yields bulk silicon when run as a batch reaction. Coupling a flanged ultrasonic horn with supercritical fluid batch titanium reactor may improve upon the silicon nanocrystal syntheses described in Chapter 2. Sonication could improve the yield from the diphenylsilane reaction and it could provide enough additional energy to break up the bulk silicon formed in the silicon halide reaction and crystallize the amorphous particles produced by the monophenylsilane and trisilane reactions. Figure 7.2 depicts how the flanged probe would fit into the batch reactor. The flange would be screw mounted to the outer shell of the reactor and O-rings will help form the high pressure seal. The probe below the flange will be secured in the reactor while the top of the probe will be connected to the power supply.

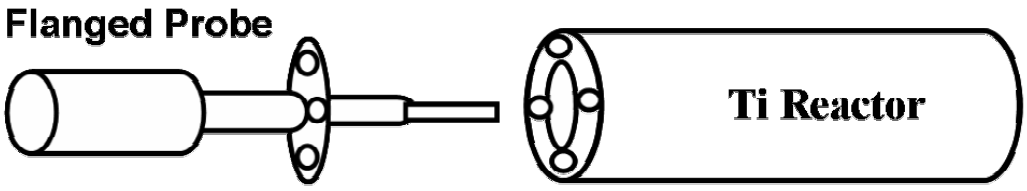

Figure 7.2 Flanged Probe with custom titanium reactor for supercritical sonochemistry.

7.2.3 Amorphous silicon nanoparticle synthesis and crystallization

Metal induced crystallization of large amorphous silicon particles was demonstrated in Chapter 5; therefore, the same crystallization method should be applicable to amorphous silicon nanoparticles. Synthesis of amorphous silicon particles was also described in Chapter 5 and it would be advantageous to extend this research to the synthesis of smaller silicon particles (under 10 nm) with unique optical properties. Some preliminary work has been completed to investigate the effects of adding a stearic stabilizer to the trisilane synthesis and while ligand incorporation does not allow for size distribution focusing it does decrease the average particle size.

Two control experiments were conducted; control #1 was a batch reaction of 1 mM trisilane heated to 500°C, 4000 psi for 10 minutes in the brass block apparatus. Control #2 started as a batch reaction under the same conditions as control #1 and after the 10 minutes of heating an additional 1 mM solution of trisilane was injected at 350°C, 4500 psi and heated for 20 minutes. The ill formed particles from control #2 had an average diameter of 225 nm; the well formed particles from control #1 had an average diameter of 60 nm and can be seen in Figure 7.3A. In an effort to control size the next experiment involved the use of octanol as a stearic stabilizer. The conditions of control #1 were repeated and after the 10 minutes of heating an injection of octanol (64 mM) occurred at 350°C, 4500 psi. After an additional 20 minutes of heating the reactor was cooled

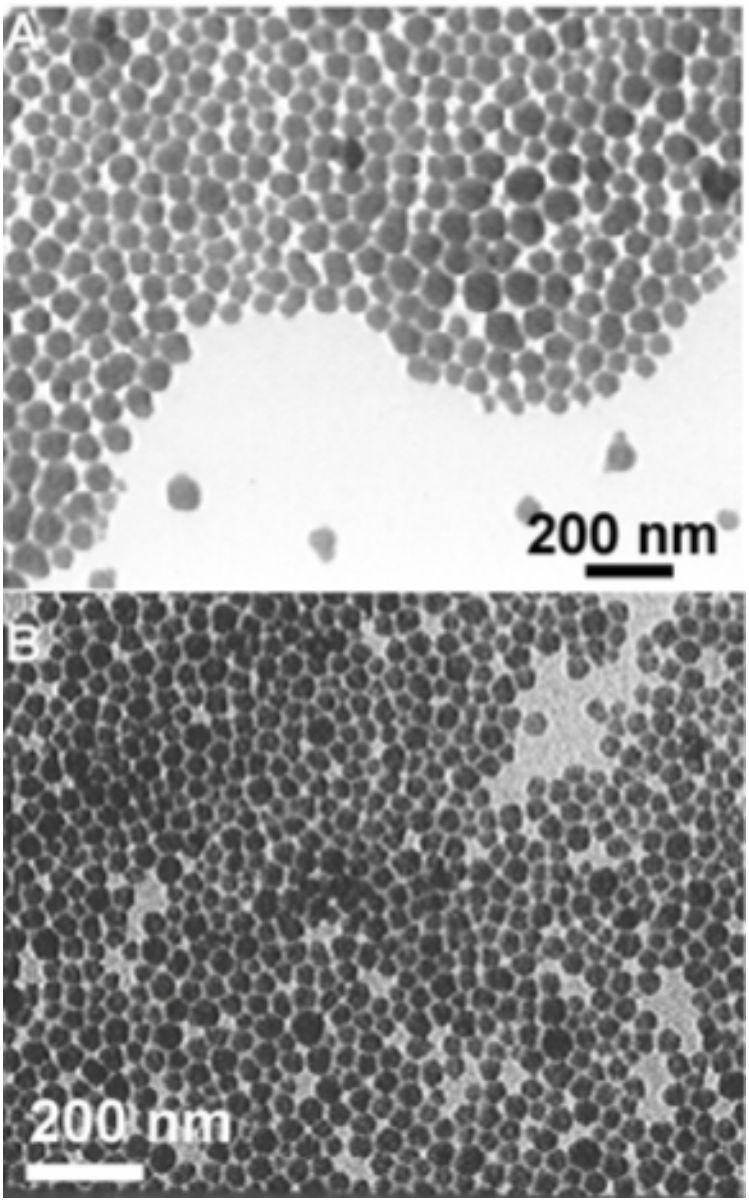

Figure 7.3 (A) Amorphous silicon particles formed in control #1; average particle size 60 nm. (B) Octanol stabilized silicon particles with average size of 32 nm.

and the particles extracted for cleaning. The average particle diameter of the octanol stabilized particles was 32 nm and in an effort to separate the particles by size, size selective precipitation produced particles as small as 16 nm. However, size selective precipitation did not produce ordered particles. An image of the octanol capped particles can be seen in Figure 7.3B. Additional work on the stabilization of amorphous silicon particles is required to drive the average size of the particles into the optically interesting region. These particles could then be crystallized by the method described in Chapter 5.

7.3 References

(1) Chen, S. W.; Ingram, R. S.; Hostetler, M. J.; Pietron, J. J.; Murray, R. W.; Schaaff, T. G.; Khoury, J. T.; Alvarez, M. M.; Whetten, R. L. *Science* **1998**, *280*, 2098-2101.

(2) Sonics & Materials; *Ultrasonic Equipment for Sonochemistry*; http://www.sonicsandmaterials.com/Sonochemistry/sonochemistry.html; **2003**.

(3) Li, H. L.; Zhu, Y. C.; Chen, S. G.; Palchik, O.; Xiong, J. P.; Koltypin, Y.; Gofer, Y.; Gedanken, A. *Journal of Solid State Chemistry* **2003**, *172*, 102-110.

(4) Cho, W. J.; Lee, S. *Journal of the Korean Physical Society* **2003**, *42*, S629-S632.

(5) Watanabe, A.; Unno, M.; Hojo, F.; Miwa, T. *Journal of Materials Science Letters* **2001**, *20*, 491-493.

(6) Suslick, K. S.; Price, G. J. *Annual Review of Materials Science* **1999**, *29*, 295-326.

(7) Suslick, K. S.; Fang, M. M.; Hyeon, T. *Journal of the American Chemical Society* **1996**, *118*, 11960-11961.

(8) Suslick, K. S.; Hyeon, T. W.; Fang, M. M. *Chemistry of Materials* **1996**, *8*, 2172-2179.

Appendix A: Refractive Index Measurement Attempts on Amorphous Silicon Colloids

A.1 Introduction

Knowledge of the refractive index of the amorphous silicon colloids described in Chapters 5 and 6 would be useful information in the characterization of the material. Significant resources have been put into the research of high refractive index materials for the purposes of 3D photonic crystals[1] and polymer nanocomposites with enhanced mechanical,[2-4] optical[2,4-6] and electrical[4,7-9] properties. The refractive index of materials is commonly measured via ellipsometry when materials are available as thin films on a substrate. The refractive index measurement of amorphous silicon colloids presented an interesting and difficult challenge because the particles have arbitrary shape and polydisperse size. Three methods were used in attempts to measure the refractive index of this material. The refractive index of amorphous silicon is expected to have values > 4 in the visible wavelength spectrum. Figure A.1 depicts previously published amorphous silicon refractive index as a function of wavelength. This amorphous silicon film was formed via Xe irradiation of a crystalline silicon wafer.[10]

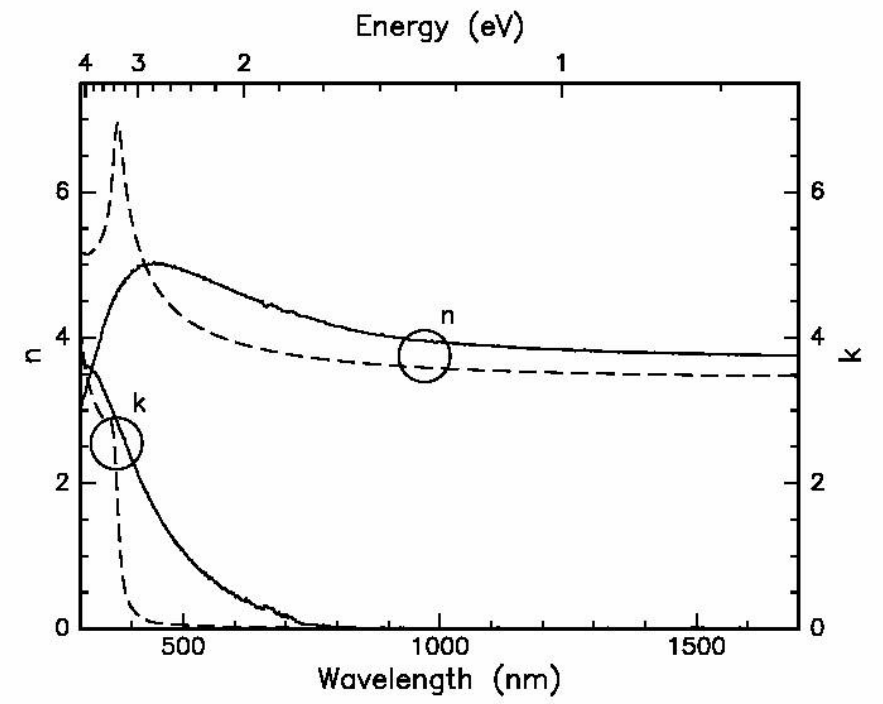

Figure A.1 Refractive index, real (n) and imaginary (k), of amorphous silicon (solid) and crystalline silicon (dashed) measured by ellipsometry. Amorphous silicon was formed by Xe irradiation of a silicon wafer.[10]

A.2 Ellipsometry

Spectroscopic ellipsometry was the first method attempted in the refractive index determination and several variations were explored. Si wafers with a native oxide layer were used as substrates; pure amorphous silicon particles were spun coat; particle/PMMA solutions were spun coat and particles were spun coat on top of a pure PMMA film. Also, particles were centrifuged out of solution onto a silicon wafer with a 300 nm oxide layer. Measurements were made with a J.A. Woollam M-2000, spectroscopic ellispometer with a wavelength range of 190-980 nm set at a 70° angle. WVASE32 software was used to analyze the ellipsometric data.

The refractive index was calculated from the Cauchy parameters as a function of wavelength:

$$n = A + \frac{B}{\lambda^2} + \frac{C}{\lambda^4} \tag{A.1}$$

The Cauchy model is commonly used in the analysis of ellipsometric data, but is only valid in wavelength regions where the imaginary index of refraction is close to zero (transparent regions). For amorphous silicon, this model is expected to be valid above ~ 600 nm. Particles in sample A1 and A2 have average diameters of 285 $\pm$ 65 nm and 177 $\pm$ 57 nm, respectively. Sample A1 was used as the pure sample and the PMMA/particle solution sample; Sample A2 was used as the pure sample on 300 nm oxide and the pure sample spun on top of a PMMA film. The

Cauchy parameters for these experiments can be found in Table A.1. The refractive index as a function of wavelength, calculated from the Cauchy parameters, for samples A1.1, A1.2 and A2.1 are shown in Figure A.2.

Table A.1 Cauchy Parameters from Ellipsometer Measurements

Sample Label	**Sample Description**	**Thickness (nm)**	**A**	**B**	**C**
A1.1	A1: native oxide wafer #1	53.502	2.943	4.102E-01	-2.079E-02
A1.2	A1: native oxide wafer #2	25.410	3.108	1.142E-01	3.214E-02
A1.P	A1: pure PMMA	429.070	1.477	3.425E-03	1.231E-04
A1.P1	A1: PMMA/Si 0.09%	383.070	1.482	2.611E-03	2.503E-04
A1.P2	A1: PMMA/Si 0.17%	394.040	1.481	2.589E-03	2.550E-04
A2.1	A2: 300 nm oxide wafer	231.330	1.510	-1.558E-02	2.554E-03

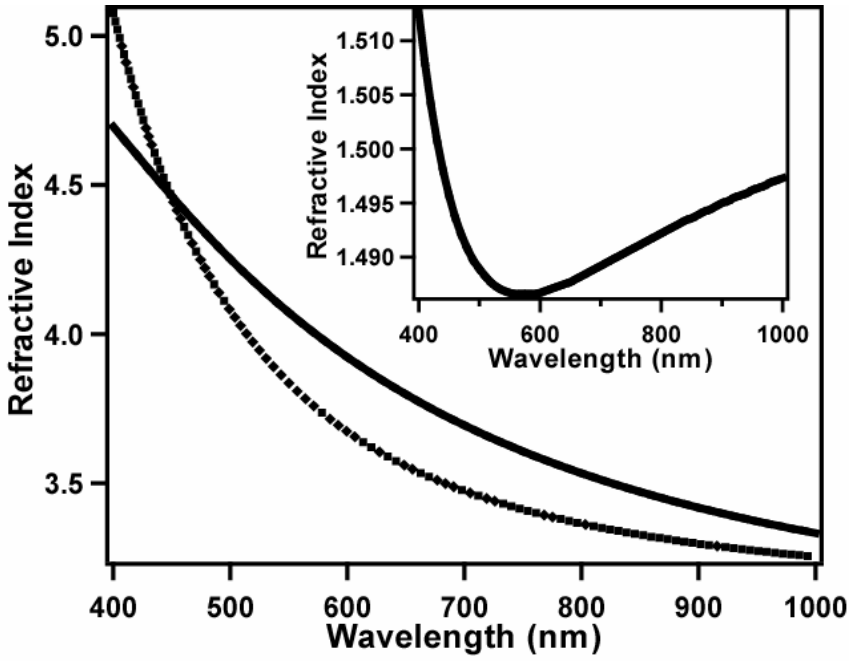

Figure A.2 Refractive Index Curves for three samples of pure a-Si particles on wafers. Solid curve (A1.1); Dashed curve (A1.2); Inset figure (A2.1)

Comparison of particle diameter with the measured thickness of films A1.1, A1.2 and A2.1 show that the measured thicknesses samples A1.1 and A1.2 are an order of magnitude smaller than their average particle diameter. This indicates that there is either less than a monolayer of particles in the film, or that the Cauchy model cannot accurately describe the film made by these amorphous silicon particles. This is unfortunate as the calculated refractive index is in the right numerical range and it follows the same trend published in Figure A.1 from 500-1000 nm. Although sample A2.1 has a realistic thickness compared with particle diameter, its refractive index values appear to be too low. Additionally, sample A2.1 exhibits a trend that is the opposite of what is physically possible. These results were not altogether unexpected as the particles did not form a good film when spun cast on a native oxide wafer. The particles formed a better film when centrifuged onto a 300 nm oxide layer silicon wafer; however, this film was not uniform enough for accurate ellipsometry measurements.

Since the particles were not adhereing to the substrate to form a good film; the next experiment involved spin coating the particles from a toluene solution onto a previously spun film of PMMA. The purpose of the PMMA film was to increase adhesion of the particles to the substrate. The PMMA film was spun cast from a dichloromethane solution and baked at 115°C to remove any residual solvent. The particles were cast from a solution which should not have redispersed any of the PMMA film. This method did increase adhesion of

amorphous silicon to the substrate and formed a good film; however there was some dissolution of the PMMA. The thickness of the PMMA film was larger before the particles were added, which should not have been the case, thereby making a refractive index measurement on the pure particle film impossible.

The last experiment attempted using the ellipsometer was the refractive index measurement of films cast from a solution of PMMA and particles in chloroform. The goal was to create a uniform dispersion of a-Si particles in a geometry (thin film) compatible with spectroscopic ellipsometry. Since the refractive index of one component (PMMA) can be measured *a priori*, it may be possible to extract the index of refraction of the a-Si component of the composite film. Four films were cast: pure PMMA, PMMA/Si (0.090 wt.% Si), PMMA/Si (0.174 wt.% Si) and PMMA/Si (0.346 wt.% Si). The Cauchy parameters for the first 3 samples, A1.P, A1.P1 and A1.P2 can be found in Table A.1. The 0.346 wt.% Si sample did not form a good film (probably due to phase separation at higher concentration) and could not be included in the experiment. The refractive index of the three good films was determined at 13 wavelengths between 400-1000 nm and plotted against weight fraction of silicon. Trendlines were fit to the data at the wavelengths of interest and the refractive index of pure amorphous silicon was extrapolated from the data. Figure A.3 shows the extrapolated refractive index values as a function of wavelength. The refractive index values appear to be reasonable as do the measured thicknesses of the films compared to

particle diameter; however, the trend of the refractive index is the same as seen in sample A2.1 which is the opposite of the physically expected dispersion trend in a transparent wavelength region. Additionally, it is unreasonable to make an extrapolation to 100% silicon from a linear curve which only covers 0-0.174% silicon.

Analysis of the data using the Cauchy model is not valid when k is greater than zero. Figure A.1 depicts k=0 at wavelengths > 700 nm; therefore, if the amorphous silicon of the samples from Table A.1 possess similar optical properties the Cauchy model will not allow for the accurate determination of the index of refraction. Thus, it is difficult to report the absolute values of the index of refraction in this case with a reasonable degree of certainty.

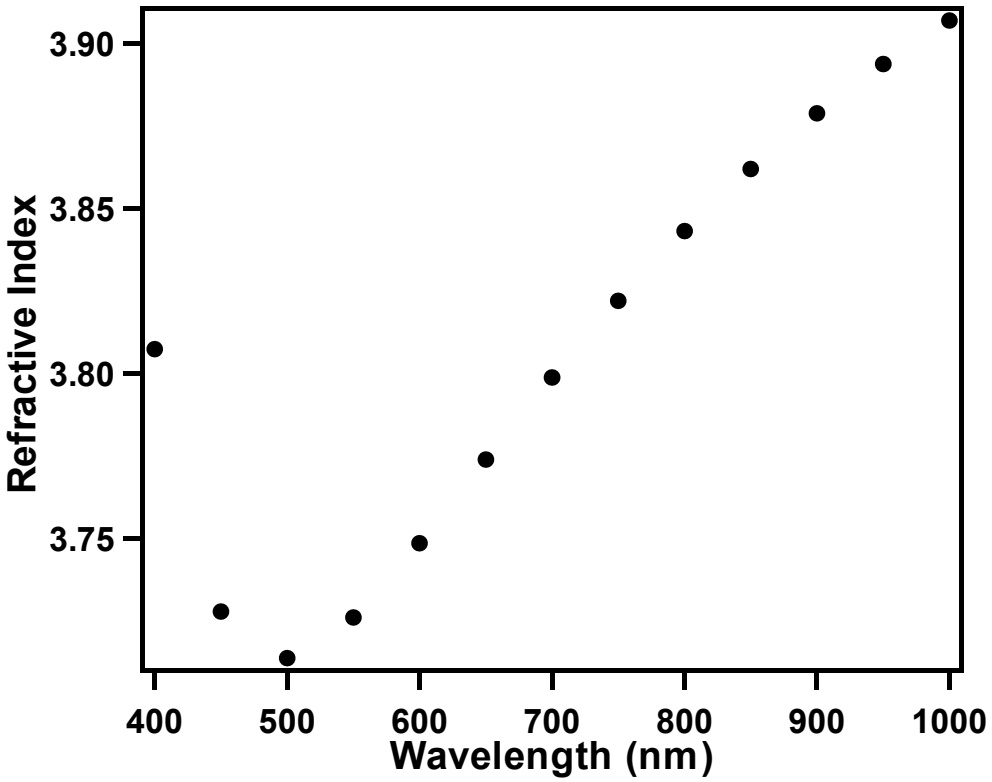

Figure A.3 Extrapolated refractive index values for amorphous silicon. Ellipsometer measurements taken of PMMA/Si films.

A.3 Electron Energy Loss Spectroscopy (EELS)

Electron Energy Loss Spectroscopy can be used to investigate electronic structure near the band gap and to examine the dielectric function of a material in the low loss region of the EELS spectrum. The latter is of concern to us as a Kramers-Kronig analysis of the low loss region can theoretically allow for the determination of the refractive index of a material. A JEOL 2010F operated at 200 kV was used for EELS measurements. The spatially resolved EELS studies were carried out with the microscope operating in scanning mode with a probe size of 0.5 nm and a beam current of approximately 0.2 nA. The electron energy loss spectra were collected with a Gatan DigiPEELS at 0.05 eV/channel energy dispersion for plasmon losses.

Figure A.4 shows an EELS spectrum for a 254 nm particle; the zero loss peak is adjusted to 0 eV and after background subtraction, the plasmon peak position is determined to be 16.55 eV with a FWHM of 5.1 eV. The third peak above 30 eV is the second plasmon peak; multiple plasmon peaks can be observed in thick samples.[12] For particles ranging in diameter from 100 - 400 nm the plasmon peak position ranged from 16.4-16.9 eV compared to 16.7 eV for bulk silicon. The plasmon peak position can be represented as $\hbar\omega_p$ and the FWHM as $\hbar\Gamma$. The real and imaginary parts of the dielectric function can then be calculated as

$$\varepsilon_1 = 1 - \left(\frac{\omega_p^2}{\omega^2 + \Gamma^2} \right) \tag{A.2}$$

$$\varepsilon_2 = \left(\frac{\Gamma \omega_p^2}{(\omega^2 + \Gamma^2)\omega} \right), \tag{A.3}$$

respectively. The plasmon loss peak can then be recreated by the loss function given as

$$\mathrm{Im}\left[\frac{-1}{\varepsilon(\omega)} \right] = \frac{\varepsilon_2}{\varepsilon_1^2 + \varepsilon_2^2} \tag{A.4}$$

Good agreement between the loss function and the plasmon loss peak helps validate the EELS measurement. Lastly, the refractive index can be calculated from the real and the imaginary parts of the dielectric function as[11]

$$n = \left[\frac{1}{2} \left(\varepsilon_1 + \sqrt{\varepsilon_1^2 + \varepsilon_2^2} \right) \right]^{1/2} \tag{A.5}$$

Figure A.5 displays a portion of the refractive index of the 254 nm diameter particle as a function of wavelength. The refractive index was determined by Kramers-Kronig analysis of the EELS spectrum. The Kramers-Kronig analysis is extrapolated to predict the index from 0.1 to 43 eV (12,400 – 28 nm) however it only accurately predicts the index near the plasmon loss peak; therefore, the refractive indices predicted at wavelengths greater than 100 nm are not reliable.

The trend of Figure A.5 is in keeping with this analysis as well as an attempt to recreate the plasmon loss peak from previously published refractive index data for amorphous silicon. Refractive index values were extracted from Figure A.1 from 400-1000 nm and attempts were made to fit the dielectric function to the index values by altering the plasmon peak position and the FWHM. The dielectric function could only be fit to the extracted index values one wavelength at a time as exhibited by Figure A.6; additionally, the plasmon peak positions were unrealistic (> 30 eV) when compared to bulk silicon (16.7 eV). Therefore, the Kramers-Kronig analysis for the determination of the refractive index is not valid for the visible wavelengths.

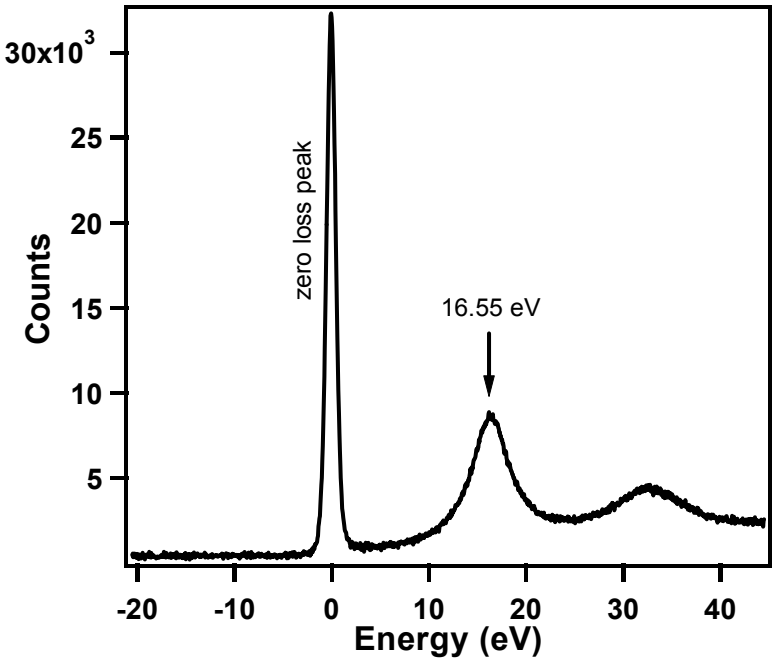

Figure A.4 EELS spectrum for a 254 nm amorphous silicon particle.

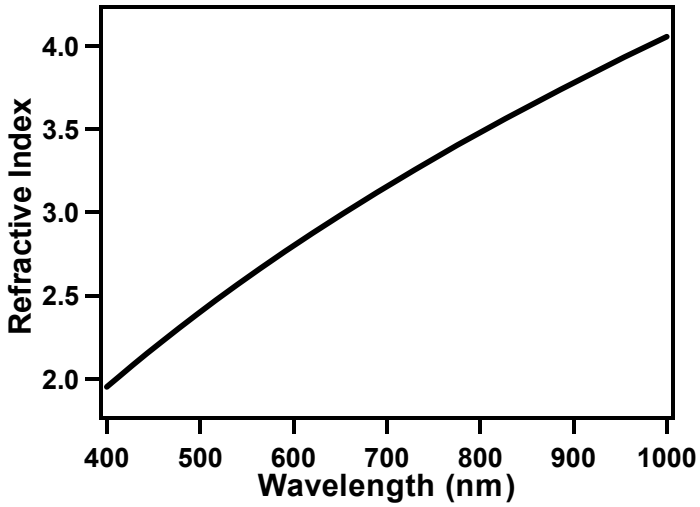

Figure A.5 A portion of the refractive index of a 254 nm amorphous silicon particle as calculated from an EELS spectrum and Kramers-Kronig analysis.

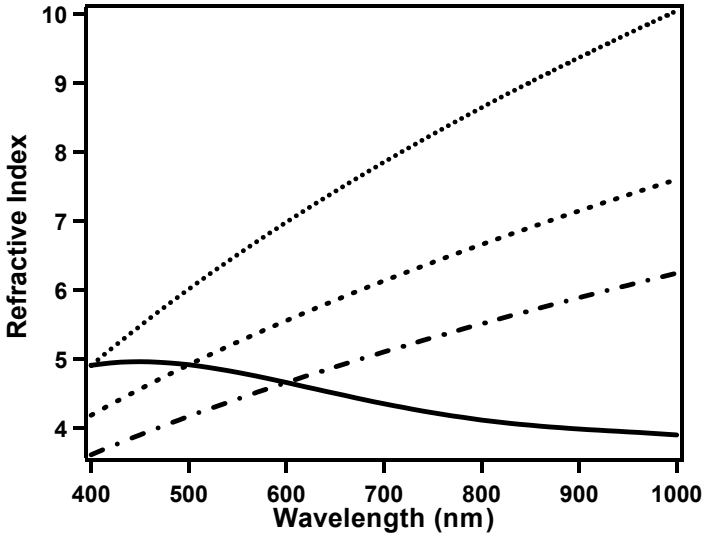

Figure A.6 Extracted refractive index data (solid) from Figure A.1 plotted against the refractive index data from the dielectric function being fit to the extracted data. (…), (---), (-.-.-.) represent data from the Kramers-Kronig analysis where the plasmon peaks were set at 42.9, 39.4 and 36.6 eV, respectively and the FWHM at 5.65, 9.5 and 12.5 respectively.

A.4 Reflectance

Some of the same problems experienced in the ellipometer experiments were faced again while attempting reflectance measurements. There are a few ways to utilize the information collected using a reflectance sphere. First, one could use the absorption coefficient, α, (determined from the absorbance) to find the imaginary part of the refractive index, *k*, which can be coupled with the reflectance, *R*, (as a function of wavelength) in order to determine the real part of the refractive index, *n*. These relationships are defined by[13]

$$I = I_O e^{-z\alpha} \tag{A.6}$$

$$\alpha = \frac{4\pi k}{\lambda} \tag{A.7}$$

$$R = \frac{(n-1)^2 + k^2}{(n+1)^2 + k^2} \tag{A.8}$$

The absorbance could be measured as a thin film of particles or the particles dispersed in a liquid; however, in order to calculate the absorption coefficient, the film thickness or the particle concentration would have to be known. If a uniform film of particles was possible, then ellipsometry could be used. As for a solution of particles, it would be very difficult to determine a molar concentration of particles as the molecular weight of the amorphous silicon particles is unknown. Even if the molecular weight of the particles could be

accurately estimated, the reflectance measurements cannot currently be performed on liquid samples with available equipment.

Varian, Inc. has available ADL downloadable programs to supplement the Spectroscopy programs which accompany their instruments.[14] A Cary 500 UV-Vis NIR Spectrophotometer was used for absorbance measurements and a Labsphere DRA-CA-5500 Reflectance Sphere attachment was used for reflectance measurements. The Thin Film Calculation ADL program was used in attempts to calculate the refractive index solely from the reflectance and knowledge of the film thickness. The reflectance of sample A2.1 was recorded from 300-1000 nm and is shown in Figure A.7. The sample was not large enough to fill the reflectance receptacle; therefore, an aluminum mask with a ½ inch diameter aperture was constructed to fill the sample port. For the baseline curve the aluminum mask and a blank 300 nm oxide wafer were used. The blank wafer was replaced with sample A2.1 for the reflectance scan. At some wavelengths the reflectance is over 100% which indicates that the sample is more reflective than the background. Using the sample thickness of 231 nm, as measured with an ellipsometer, the refractive index of sample A2.1 was determined to be 154 in the visible range. The refractive index value was not observed to change as a function of wavelength. The magnitude of the fitted index and its dispersion behavior with changing wavelength make this method very questionable.

Next, amorphous silicon particles were deposited on filter paper (a less reflective substrate than a silicon wafer) and the reflectance measurement repeated. Three samples were prepared with varying concentrations; the observed reflectance decreased with increasing particle concentration as shown in Figure A.8. This last experiment confirmed that with increasing concentration more light was absorbed by the particles. While this did not lead to a refractive index measurement (due to the questionable concentration/thickness of the sample) it does inspire confidence in this method as a future source for refractive index measurement.

A.5 Conclusions

While ellipsometry, electron energy loss spectroscopy and reflectance methods did not ultimately lead to a refractive index measurement for the amorphous silicon particles there was much to be learned in the attempts. Ellipsometry and reflectance measurements hold the greatest promise for a future refractive index measurement if a high concentration liquid or composite film could be formed from these particles.

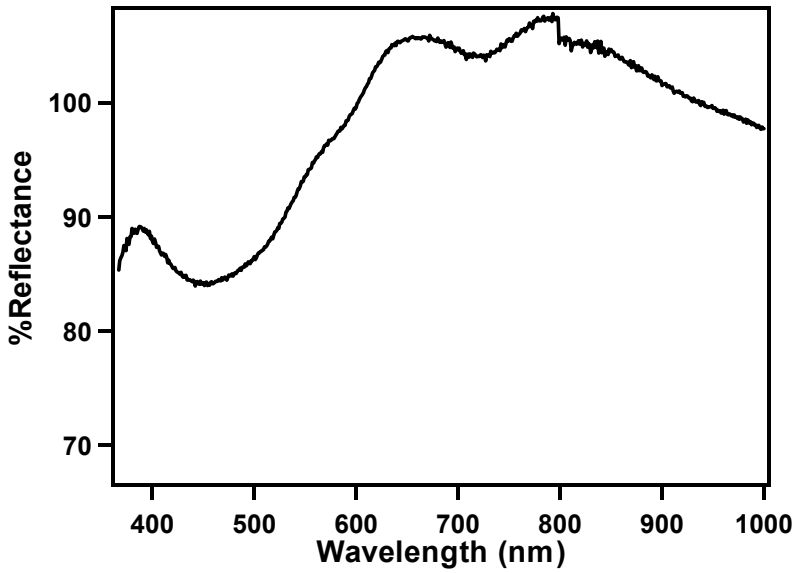

Figure A.7 Reflectance of amorphous silicon particles centrifuged onto a 300 nm oxide wafer (sample A2.1).

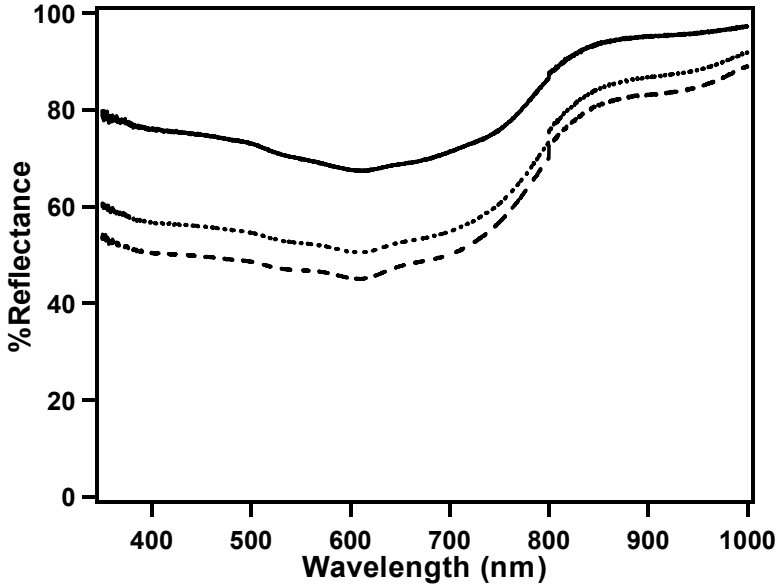

Figure A.8 Reflectance of amorphous silicon particles deposited on filter paper. Least concentrated (solid); middle concentration (dotted); most concentrated (dashed).

A.6 References

(1) Vlasov, Y. A.; Yao, N.; Norris, D. J. *Advanced Materials* **1999**, *11*, 165-169.

(2) Schmidt, H. K. *Macromolecular Symposia* **1996**, *101*, 333-342.

(3) Otooni, M. A. *Materials Research Society Symposium Proceedings* **1995**, *362*, 49-59.

(4) Papadimitrakopoulos, F.; Wisniecki, P.; Bhagwagar, D. E. *Chemistry of Materials* **1997**, *9*, 2928-2933.

(5) Levy, D.; Esquivias, L. *Advanced Materials* **1995**, *7*, 120-129.

(6) Ogawa, T.; Kanemitsu, Y.; Editors *Optical Properties of Low-Dimensional Materials*, 1995.

(7) Clement, R. *ACS Symposium Series* **1995**, *585*, 29-42.

(8) Kanatzidis, M. G.; Wu, C. G.; Marcy, H. O.; Kannewurf, C. R. *Journal of the American Chemical Society* **1989**, *111*, 4139-4141.

(9) Kanatzidis, M. G.; Wu, C. G.; Marcy, H. O.; Degroot, D. C.; Kannewurf, C. R. *Chemistry of Materials* **1990**, *2*, 222-224.

(10) de Dood, M. J. A.; Polman, A.; Zijlstra, T.; van der Drift, E. *Journal of Applied Physics* **2002**, *92*, 649-653.

(11) Daniels, J.; Festenberg, C. v.; Raether, H.; Zeppenfeld, K. In *Springer Tracts in Modern Physics*; Hohler, G., Ed.; Springer: New York, 1970; Vol. 54, pp 78-97.

(12) Williams, D. B.; Carter, C. B. In *Transmission Electron Microscopy*; Plenum Press: New York, 1996; Vol. IV, pp 697-699.

(13) Bohren, C. F.; Huffman, D. R. *Absorption and Scattering of Light by Small Particles*; John Wiley & Sons: New York, 1983.

(14) *Cary WinUV ADL programs*; http://www.varianinc.com/cgi-bin/nav?products/spectr/uv/adl/index&cid=LPOIPQFO; **2003**.

Appendix B: Quantum Confinement in Nanomaterials Explored Via Particle in a Box Theory[§]

B.1 Introduction

In the study of nanomaterials, the concept of quantum confinement is often used to describe the anomalous behavior of the properties of nanomaterials compared to their bulk properties. Quantum confinement effects arise from the shrinking of the dimensions of a material such that the magnitude of the dimensions drives the quantized energy separations into discrete levels instead of virtually continuous levels. One anomalous behavior exhibited by nanomaterials is an increased quantum yield.[1] Light can be elicited from many systems of nanocrystals (Si, Ge, CdS, CdSe) whose bulk systems exhibit little or no luminescence. Detailed theoretical work has been published in this area by Efros and Rosen,[2] Steigerwald and Brus,[3] and Lippens and Lannoo,[4] but for the purposes of my own understanding and satisfaction, I will explore quantum confinement through the derivation of a particle in a 1-D, 3-D and spherical box to explain why the material properties change with decreasing dimensions.

[§]Contents of Appendix B written for PHY 392T; Physics of Nanostructures 2002.

B.2 Particle in a Box

A nanocrystal cannot be described as a 1-D box, but the simplest case will be examined first, followed by a 3-D box (cube) to approximate a nanocrystal, and finally the spherical case. The box will represent the nanocrystal and the particle will represent the electron-hole pair with effective mass m^* (1-D and 3-D case) and μ (spherical case).[5]

B 2.1 Derivation of Energy States for Particle in a 1-D Box:

Assume there is a particle confined to a 1-D box (Figure B.1); the particle can move along the x-axis between *0* and *a,* but no matter its kinetic energy it cannot escape the box. The potential energy then must be zero within the box and infinite outside the box, yielding the boundary conditions:

$$\Psi(x,t) = 0 \; ; \; x < 0 \text{ and } x > a \tag{B.1}$$

Now to derive an expression in which to make use of the boundary conditions one must start with the case of a particle with a nonzero potential energy:

$$E = \frac{p^2}{2m^*} + V(x) . \tag{B.2}$$

The dispersion relation follows as:

$$\omega = \frac{\hbar k^2}{2m^*} + \frac{V(x)}{\hbar} . \tag{B.3}$$

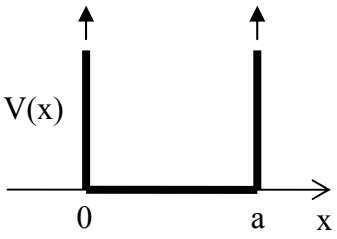

Figure B.1. Potential Energy of 1-D box

The 1-D time-dependent Schrödinger equation can be derived as:

$$i\hbar\left[\frac{\partial\Psi(x,t)}{\partial t}\right]_x = -\frac{\hbar^2}{2m^*}\left[\frac{\partial^2\Psi(x,t)}{\partial x^2}\right]_t + V(x)\Psi(x,t)\,. \tag{B.4}$$

Since the potential energy is zero inside the box the wave function can be described as:

$$i\hbar\left[\frac{\partial\Psi(x,t)}{\partial t}\right] = -\frac{\hbar^2}{2m^*}\left[\frac{\partial^2\Psi(x,t)}{\partial x^2}\right]. \tag{B.5}$$

Then separating the spatial dependence of the wave function from the time dependence, the time-independent Schrödinger equation can be derived:

$$-\frac{\hbar^2}{2m^*}\frac{d^2\psi(x)}{dx^2} = [E - V(x)]\psi(x)\,. \tag{B.6}$$

The potential energy can be discarded for the region within the box yielding:

$$\frac{d^2\psi(x)}{dx^2} = -\frac{2m^*E}{\hbar^2}\psi(x)\,. \tag{B.7}$$

Applying the boundary conditions from Equation B.1 gives the following solution for the quantized energy of a particle in a box.

$$E_n = \frac{n^2 \pi^2 \hbar^2}{2m^* a^2} \; ; \quad (\text{n} = 1, 2, 3\ldots). \tag{B.8}$$

For the 3-D scenario Equation B.8 becomes:

$$E_{n_1 n_2 n_3} = \frac{\pi^2 \hbar^2}{2m^*}\left(\frac{n_1^{\,2}}{a^2} + \frac{n_2^{\,2}}{b^2} + \frac{n_3^{\,2}}{c^2}\right); \quad (\text{n}_1, \text{n}_2, \text{n}_3 = 1, 2, 3\ldots). \tag{B.9}$$

Treating a nanocrystal as a cube turns Equation B.9 into:

$$E_n = \frac{\pi^2 \hbar^2}{2m^*}\left(\frac{3n^2}{a^2}\right); \quad (\text{n} = 1, 2, 3\ldots); \text{ a = diameter of nanocrystal.} \tag{B.10}$$

Examining a particle in a sphere, the kinetic energy becomes:

$$T = \frac{1}{2\mu}\left(p_r^{\,2} + \frac{p_\theta^{\,2}}{r^2} + \frac{p_\phi^{\,2}}{r^2 \sin^2\theta}\right) \tag{B.11}$$

where the classical radial momentum, the angular momentum corresponding to rotation in the plane formed by **r** and the z-axis, and the angular momentum around the z-axis are given as:

$$p_r \equiv \mu \frac{dr}{dt}; \tag{B.12}$$

$$p_\theta \equiv \mu r^2 \frac{d\theta}{dt}; \tag{B.13}$$

$$p_\phi \equiv \mu (r \sin\theta)^2 \frac{d\phi}{dt}; \tag{B.14}$$

respectively. The angular momentum around the origin can be defined as

$$\mathbf{L} \equiv \mathbf{r} \times \mathbf{p}. \tag{B.15}$$

Thus the kinetic energy may be written

$$T = \frac{p_r^{\,2}}{2\mu} + \frac{L^2}{2I} \tag{B.16}$$

where $I \equiv \mu r^2$.

Concentrating on the z-axis and applying the same boundary conditions adapted for the spherical case, the quantum expression for the centrifugal energy can be derived as

$$T = \frac{l\left(l+1\right)\hbar^2\right)}{2\mu r^2} \quad (l = 0, 1, 2\ldots). \tag{B.17}$$

This expression[5] is similar to what has been reported elsewhere[2,4] as:

$$E_n = \frac{2n^2\pi^2\hbar^2}{d^2 m^*}. \tag{B.18}$$

It is not clear to me how the π^2 term gets dropped from the spherical energy derivation, but for the purposes of our theoretical calculations Equation B.18 will be used. The effective mass of the electron-hole pair will be calculated as

$$\frac{1}{m^*} = \frac{1}{m_e^{\,*}} + \frac{1}{m_h^{\,*}} \tag{B.19}$$

where $m_e^{\,*}$ is the effective mass of the electron and $m_h^{\,*}$ is the effective mass of the hole.[4]

Before calculating the energy due to quantum confinement one other factor must be taken into account – the Coulombic attraction between the electron and hole. This factor will tend to shrink the energy difference rather than increase the gap; therefore, this factor will be negative:

$$E_c = -\frac{3.572e^2}{\varepsilon \cdot d} \tag{B.20}$$

where e is the charge on an electron, ε is the dielectric constant and d is the diameter of the crystal.[4] For our theoretical calculations we will be looking at the case of n = 1. Taking into account the kinetic energy of the electron-hole pair and their Coulombic attraction, Equations B.8, B.10 and B.18 become:

$$E = \frac{\pi^2\hbar^2}{2m^* d^2} - \frac{3.572e^2}{\varepsilon \cdot d}\text{; 1-D case} \tag{B.21}$$

$$E = \frac{\pi^2\hbar^2}{2m^*}\left(\frac{3}{d^2}\right) - \frac{3.572e^2}{\varepsilon \cdot d}\text{; 3-D case} \tag{B.22}$$

$$E = \frac{2\pi^2\hbar^2}{d^2 m^*} - \frac{3.572e^2}{\varepsilon \cdot d}\text{; spherical case.} \tag{B.23}$$

These energies should correspond to the increase in the band gap of a material due to quantum confinement. The energies calculated above must be added to the band gap energy of the bulk material to find the band gap due to quantum confinement.

B.3 Results and Discussion

Let us test Equations B.21-23 derived above for the case of quantum confined cadmium sulfide using the following values of $0.20m_o$, $0.70m_o$,[6] 5.071 and 2.02eV[7] for the effective mass of an electron, hole, dielectric constant and the bulk band gap energy, respectively.

For the cases above, when the calculated Coulombic attraction surpassed the kinetic energy of the electron-hole pair, the total *extra* energy (Equations B.21-23) becomes negative. This is indicative that a maximum diameter has been reached such that the bulk band gap and the quantum confined band gap are equal. As there will not be a net negative extra energy contribution to the band gap, a value of zero has been entered. The calculated data can be found in Table B.1 and a comparison of the theoretical values to those experimentally measured for CdS nanocrystal[8] can be seen in Figure B.2.

One can see that the theoretical methods for calculating the bang gap of a nanocrystal follow the experimental trend down to a 2 nm CdS crystal. At diameters smaller than this a 1-D particle in a box more closely approximates the band gap. It is not necessarily unexpected that the spherical model becomes unreliable at small diameters.[4] The effective masses and the dielectric constant vary more in this region and the spherical model deviates from experimental values. The fact that the 1-D model works so well is more surprising, but perhaps this can be attributed to the fact that semiconductor nanomaterials are often

Table B.1 Theoretical values of quantum confined band gap

	1-D	3-D	spherical	1-D	3-D	spherical
Diameter (nm)	**E (eV) from Eqns B.21-23**			**Q.C. Band Gap (eV)**		
1	0.960	5.801	8.222	2.980	7.821	10.242
2	0	1.085	1.690	2.020	3.105	3.710
3	0	0.320	0.589	2.020	2.340	2.609
4	0	0.089	0.240	2.020	2.109	2.260
5	0	0	0.095	2.020	2.020	2.115
6	0	0	0.026	2.020	2.020	2.046
7	0	0	0	2.020	2.020	2.020
8	0	0	0	2.020	2.020	2.020
9	0	0	0	2.020	2.020	2.020
10	0	0	0	2.020	2.020	2.020
1000	0	0	0	2.020	2.020	2.020

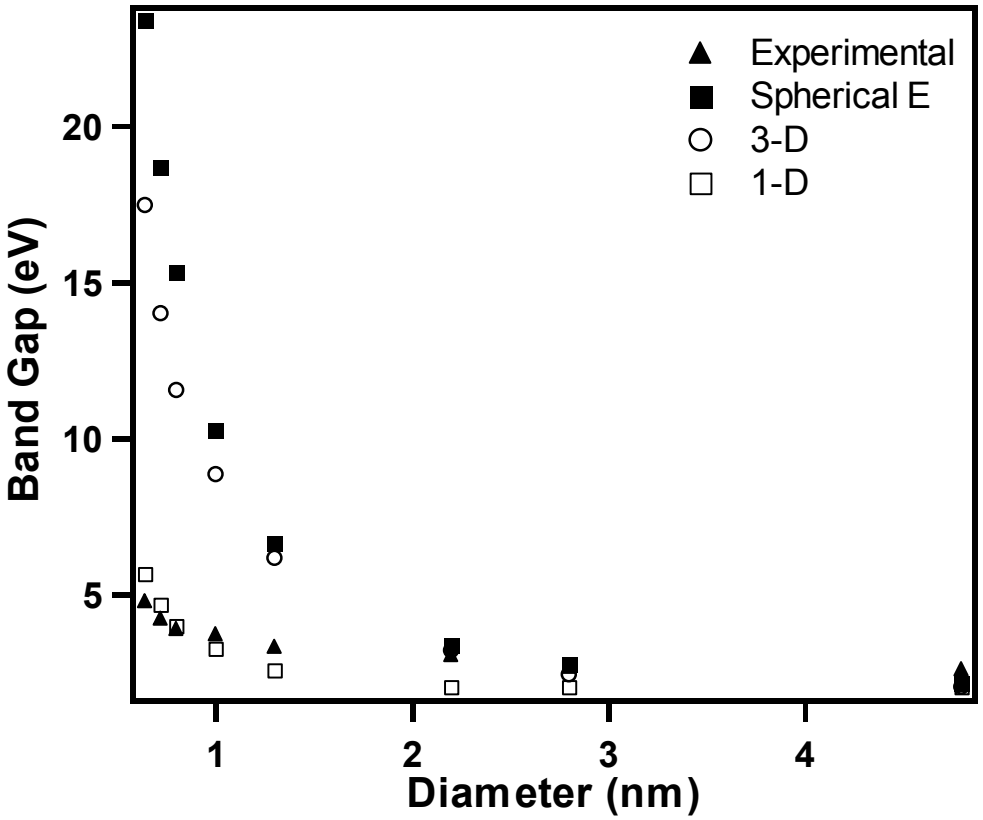

Figure B.2 Experimentally calculated band gap of small CdS nanocrystals plotted against theoretically calculated values of the band gap for a 1-D, 3-D and spherical particle in a box.

described as being 0-D and 1-D materials in reference to the density of states and quantized energy.[1]

The theory presented here is by no means comprehensive to the point of incorporating all factors at play in the widening of the band gap of nanoscale semiconductor materials. All the work completed for this paper was for

individual understanding and comprehension of the effects of quantum confinement on the band gap of materials which influences optical and electronic properties.

B.4 References

(1) Alivisatos, A. P. *Science* **1996**, *271*, 933.

(2) Efros, A. L.; Rosen, M. *Annual Review of Materials Science* **2000**, *30*.

(3) Steigerwald, M. L.; Brus, L. E. *Annual Review of Materials Science* **1989**, *19*, 471-495.

(4) Lippens, P. E.; Lannoo, M. *Physical Review B* **1989**, *39*, 10935.

(5) Berry, R. S.; Rice, S. A.; Ross, J. *Physical Chemistry*; John Wiley & Sons, Inc.: New York, 1980.

(6) Trindade, T.; O'Brien, P.; Picket, N. L. *Chemistry of Materials* **2001**, *13*, 3843-3858.

(7) Xu, Y.-N.; Ching, W. Y. *Physical Review B* **1993**, *48*, 4335-4351.

(8) Vossmeyer, T.; Katsikas, L.; Giersig, M.; Popovic, I. G.; Diesner, K.; Chemseddine, A.; Eychmuller, A.; Weller, H. *The Journal of Physical Chemistry* **1994**, *98*, 7665-7673.

Bibliography

E. Adachi, A. S. Dimitrov and K. Nagayama *Langmuir* **1995**, *11*, 1057-1060.

A. M. Al-Dhafiri *Journal of Saudi Chemical Society* **2002**, *6*, 365-376.

A. P. Alivisatos *Science* **1996**, *271*, 933-937.

M. b. Amjoud, A. Reynes, R. Morancho and R. Carles *Journal of Materials Chemistry* **1992**, *2*, 1205-1208.

R. P. Andres, T. Bein, M. Dorogi, S. Feng, J. I. Henderson, C. P. Kubiak, W. Mahoney, R. G. Osifchin and R. Reifenberger *Science* **1996**, *272*, 1323-1325.

M. Antonietti, J. Hartmann, M. Neese and U. Seifert *Langmuir* **2000**, *16*, 7634-7639.

K. Aoki, H. T. Miyazaki, H. Hirayama, K. Inoshita, T. Baba, K. Sakoda, N. Shinya and Y. Aoyagi *Nature Materials* **2003**, *2*, 117-121.

U. Banin, M. Bruchez, A. P. Alivisatos, T. Ha, S. Weiss and D. S. Chemla *J. Chem. Phys.* **1999**, *110*, 1195-1201.

A. J. Bard, J. D. Debad, J. K. Leland, G. B. Sigal, J. L. Wilbur and J. N. Wohlstadter In *Encyclopedia of Analytical Chemistry: Applications, Theory and Instrumentation*; R. A. Meyers, Ed.; John Wiley & Sons: New York, 2000; Vol. 11, p 9842.

A. J. Bard and L. R. Faulkner *Electrochemical Methods: Fundamentals and Applications*; 2nd ed.; Wiley: New York, 2001.

M. G. Bawendi, P. J. Carroll, W. L. Wilson and L. E. Brus *J. Chem. Phys.* **1992**, *96*, 946-954.

A. F. Beardon and K. Stephenson *Indiana Univ. Math. J.* **1990**, *39*, 1383-1425.

R. S. Berry, S. A. Rice and J. Ross *Physical Chemistry*; John Wiley & Sons, Inc.: New York, 1980.

A. Blanco, E. Chomski, S. Grabtchak, M. Ibisate, S. John, S. W. Leonard, C. Lopez, F. Meseguer, H. Miguez, J. P. Mondia, G. A. Ozin, O. Toader and H. M. van Driel *Nature* **2000**, *405*, 437-440.

C. F. Bohren and D. R. Huffman *Absorption and Scattering of Light by Small Particles*; John Wiley & Sons: New York, 1983.

G. Bottger, C. Liguda, M. Schmidt and M. Eich *Applied Physics Letters* **2002**, *81*, 2517-2519.

P. L. Bowers and K. Stephenson *Math. Proc. Camb. Philos. Soc.* **1992**, *111*, 487-513.

P. V. Braun and P. Wiltzius *Nature* **1999**, *402*, 603-604.

A. P. J. Breu, H. M. Ensner, C. A. Kruelle and I. Rehberg *Physical Review Letters* **2003**, *90*.

L. E. Brus, P. F. Szajowski, W. L. Wilson, T. D. Harris, S. Schuppler and P. H. Citrin *J. Am. Chem. Soc.* **1995**, *117*, 2915-2922.

M. Brust, J. Fink, D. Bethell, D. J. Shiffrin and C. Kiely *Journal of Chemistry Society, Chemical Communications* **1995**, 1655.

K. Busch and S. John *Physical Review E* **1998**, *58*, 3896-3908.

S. A. Campbell *The Science and Engineering of Microelectronic Fabrication*; 2nd ed.; Oxford University Press, Inc.: New York, 2001.

L. T. Canham *Appl. Phys. Lett.* **1990**, *57*, 1046-1048.

T. Cassagneau, J. H. Fendler, S. A. Johnson and T. E. Mallouk *Advanced Materials (Weinheim, Germany)* **2000**, *12*, 1363-1366.

S. Chen, R. S. Ingram, M. J. Hostetler, J. J. Pietron, R. W. Murray, T. G. Schaaff, J. T. Khoury, M. M. Alvarez and R. L. Whetten *Science* **1998**, *280*, 2098.

S. Chen, R. W. Murray and S. W. Feldberg *Journal of Physical Chemistry B* **1998**, *102*, 9898-9907.

S. Chen, L. A. Truax and J. M. Sommers *Chemistry of Materials* **2000**, *12*, 3864-3870.

S. W. Chen, R. S. Ingram, M. J. Hostetler, J. J. Pietron, R. W. Murray, T. G. Schaaff, J. T. Khoury, M. M. Alvarez and R. L. Whetten *Science* **1998**, *280*, 2098-2101.

W. J. Cho and S. Lee *Journal of the Korean Physical Society* **2003**, *42*, S629-S632.

H. C. Choi and J. M. Buriak *Chem. Mat.* **2000**, *12*, 2151-2156.

J. H. Choi, D. Y. Kim, S. J. Park, B. K. Choo and J. Jang *Thin Solid Films* **2003**, *427*, 289-293.

E. Chomski and G. A. Ozin *Advanced Materials* **2000**, *12*, 1071-1078.

R. Clement *ACS Symposium Series* **1995**, *585*, 29-42.

G. Cocorullo, F. G. D. Corte, I. Rendina, A. Rubino and E. Terzini *Ieee Photonics Technology Letters* **1996**, *8*, 900-902.

C. P. Collier, T. Vossmeyer and J. R. Heath *Annual Review of Physical Chemistry* **1998**, *49*, 371-404.

C. R. Collins and K. Stephenson *Comput. Geom.-Theory Appl.* **2003**, *25*, 233-256.

J. A. Connor, R. N. Haszeldine, G. J. Leigh and R. D. Sedgwick *J. Chem. Soc. (A)* **1967**, *5*, 768-771.

R. W. Coutant and A. Levy "A Kinetic Study of the Thermal Decomposition of Selected Cyclohexyl and Phenylsilanes," Aerospace Research Laboratories, 1969.

A. G. Cullis, L. T. Canham and P. D. J. Calcott *J. Appl. Phys.* **1997**, *82*, 909-965.

J. Daniels, C. v. Festenberg, H. Raether and K. Zeppenfeld In *Springer Tracts in Modern Physics*; G. Hohler, Ed.; Springer: New York, 1970; Vol. 54, pp 78-97.

I. M. T. Davidson and A. B. Howard *J. Chem. Soc., Chem. Commun.* **1973**, *9*, 323-324.

M. J. A. de Dood, A. Polman, T. Zijlstra and E. van der Drift *Journal of Applied Physics* **2002**, *92*, 649-653.

R. D. Deegan *Physical Review E* **2000**, *61*, 475-485.

N. D. Denkov, O. D. Velev, P. A. Kralchevsky, I. B. Ivanov, H. Yoshimura and K. Nagayama *Langmuir* **1992**, *8*, 3183-3190.

J. Derakhshandeh, N. Golshani, S. Mohajerzadeh and E. Asl Soleimani *Thin Solid Films* **2003**, *427*, 324-329.

T. Dubejko and K. Stephenson *Mich. Math. J.* **1995**, *42*, 211-234.

T. Dubejko and K. Stephenson In *Experimental Mathematics*; Jones and Bartlett Publishers: Boston, 1995; Vol. 4, pp 307-348.

V. M. Dubin, F. Ozanam and J. N. Chazalviel *Phys. Rev. B* **1994**, *50*, 14867-14880.

A. L. Efros and M. Rosen *Annual Review of Materials Science* **2000**, *30*.

A. L. Efros and M. Rosen *Phys. Rev. Lett.* **1997**, *78*, 1110-1113.

M. Elbaum and S. G. Lipson *Physical Review Letters* **1994**, *72*, 3562-3565.

F. R. F. Fan and A. J. Bard *Science* **1997**, *277*, 1791-1793.

L. R. Faulkner and A. J. Bard *Electroanalytical Chemistry*; Marcel Dekker: New York, 1977; Vol. 10.

L. R. Faulkner and A. J. Bard In *Electroanalytical Chemistry*; A. J. Bard and I. Rubenstein, Eds.; Marcel Dekker: New York, 1998; Vol. 20, pp 1-95.

Cary WinUV ADL programs; http://www.varianinc.com/cgi-bin/nav?products/spectr/uv/adl/index&cid=LPOIPQFO; **2003**.

A. Franceschetti and A. Zunger *Phys. Rev. B* **2000**, *62*, 2614-2623.

S. Gall, M. Muske, I. Sieber, O. Nast and W. Fuhs *Journal of Non-Crystalline Solids* **2002**, *299*, 741-745.

G. L. Ge and L. E. Brus *Nano Lett.* **2001**, *1*, 219-222.

I. N. Germanenko, S. T. Li and M. S. El-Shall *J. Phys. Chem. B* **2001**, *105*, 59-66.

J. J. Gray, D. H. Klein, R. T. Bonnecaze and B. A. Korgel *Physical Review Letters* **2000**, *85*, 4430-4433.

J. J. Gray, D. H. Klein, B. A. Korgel and R. T. Bonnecaze *Langmuir* **2001**, *17*, 2317-2328.

B. I. Halperin and D. R. Nelson *Physical Review Letters* **1978**, *41*, 121-124.

A. E. Hanna, M. T. Tuominen and M. Tinkham *Phys. Rev. Lett.* **1992**, *68*, 3228-3231.

T. Hanrath and B. A. Korgel *Advanced Materials (Weinheim, Germany)* **2003**, *15*, 437-440.

S. Haram, K., B. M. Quinn and A. J. Bard *Journal of the American Chemical Society* **2001**, *123*, 8860-8861.

R. Hillebrand, S. Senz, W. Hergert and U. Gosele *Journal of Applied Physics* **2003**, *94*, 2758-2760.

M. A. Hines and P. GnyotSionnest *J. Phys. Chem.* **1996**, *100*, 468-471.

J. D. Holmes, K. P. Johnston, R. C. Doty and B. A. Korgel *Science* **2000**, *287*, 1471-1473.

J. D. Holmes, K. J. Ziegler, R. C. Doty, L. E. Pell, K. P. Johnston and B. A. Korgel *J. Am. Chem. Soc.* **2001**, *123*, 3743-3748.

D. C. Hong *Physica A* **1999**, *271*, 192-199.

D. C. Hong, P. V. Quinn and S. Luding *Physical Review Letters* **2001**, *86*, 3423-3426.

M. J. Hostetler, J. J. Stokes and R. W. Murray *Langmuir* **1996**, *12*, 3604-3612.

P. Hoyer and H. Weller *Chem. Phys. Lett.* **1994**, *224*, 75-80.

P. Hoyer and H. Weller *J. Phys. Chem.* **1995**, *99*, 14096-14100.

G.-R. Hu, T. J. Huang and Y. S. Wu *Japanese Journal of Applied Physics, Part 2: Letters* **2003**, *42*, L895-L897.

M. Itoh, K. Inoue, J. Ishikawa and K. Iwata *Journal of Organometallic Chemistry* **2001**, *629*, 1-6.

S. S. Iyer and Y. H. Xie *Science* **1993**, *260*, 40-46.

M. Johannsen *Journal of Chromatography, A* **2001**, *937*, 135-138.

S. John *Physical Review Letters* **1987**, *58*, 2486-2489.

A. R. Joshi and K. C. Saraswat *Journal of the Electrochemical Society* **2003**, *150*, G443-G449.

T. Kanai, T. Sawada and K. Kitamura *Langmuir* **2003**, *19*, 1984-1986.

M. G. Kanatzidis, C. G. Wu, H. O. Marcy, D. C. Degroot and C. R. Kannewurf *Chemistry of Materials* **1990**, *2*, 222-224.

M. G. Kanatzidis, C. G. Wu, H. O. Marcy and C. R. Kannewurf *Journal of the American Chemical Society* **1989**, *111*, 4139-4141.

H. Kasai, Y. Komai, S. Okazaki, S. Okada, H. Oikawa, T. Adschiri, K. Arai and H. Nakanishi *Kobunshi Ronbunshu* **2001**, *58*, 650-660.

A. H. Kitai and Editor *Solid State Luminescence: Theory, Materials and Devices*, 1993.

A. W. Knight and G. M. Greenway *Analyst* **1994**, *119*, 879-890.

D. Knittel, W. Saus and E. Schollmeyer *J. Text. Inst.* **1993**, *84*, 534-552.

M. Konno and T. Motegi *Kemikaru Enjiniyaringu* **1998**, *43*, 914-919.

B. A. Korgel and H. G. Monbouquette *J. Phys. Chem.* **1996**, *100*, 346-351.

J. M. Kosterlitz and D. J. Thouless *Journal of Physics C: Solid State Physics* **1973**, *6*, 1181-1203.

D. Kovalev, H. Heckler, M. Ben-Chorin, G. Polisski, M. Schwartzkopff and F. Koch *Phys. Rev. Lett.* **1998**, *81*, 2803-2806.

P. A. Kralchevsky and N. D. Denkov *Current Opinion in Colloid & Interface Science* **2001**, *6*, 383-401.

P. A. Kralchevsky, V. N. Paunov, N. D. Denkov, I. B. Ivanov and K. Nagayama *Journal of Colloid and Interface Science* **1993**, *155*, 420-437.

T. D. Krauss and L. E. Brus *Phys. Rev. Lett.* **1999**, *83*, 4840-4843.

M. Kuno, D. P. Fromm, A. Gallagher, D. J. Nesbitt, O. I. Micic and A. J. Nozik *Nano Lett.* **2001**, *1*, 557-564.

M. Kuno, D. P. Fromm, H. F. Hamann, A. Gallagher and D. J. Nesbitt *Journal of Chemical Physics* **2001**, *115*, 1028.

P. R. Kust, R. A. Hendel, M. A. Markowitz, P. E. Schoen and B. P. Gaber *Colloids and Surfaces, A: Physicochemical and Engineering Aspects* **2000**, *168*, 207-214.

Q. Lang, I. F. Cheng, C. M. Wai, A. Paszczynski, R. L. Crawford, B. Barnes, T. J. Anderson, R. Wells, G. Corti, L. Allenbach, D. P. Erwin, T. Assefi and M. Mojarradi *Analytical Biochemistry* **2002**, *301*, 225-234.

Y. L. Lee and J. M. Sanchez *Journal of Crystal Growth* **1997**, *178*, 513-517.

A. Levy, R. W. Coutant, E. L. Merryman and D. E. Trent "The Thermal Stability of Some Arylsilanes," Aerospace Research Laboratories, 1965.

D. Levy and L. Esquivias *Advanced Materials* **1995**, *7*, 120-129.

H. L. Li, Y. C. Zhu, S. G. Chen, O. Palchik, J. P. Xiong, Y. Koltypin, Y. Gofer and A. Gedanken *Journal of Solid State Chemistry* **2003**, *172*, 102-110.

Q. Y. Li and P. Dong *Journal of Colloid and Interface Science* **2003**, *261*, 325-329.

P. E. Lippens and M. Lannoo *Physical Review B* **1989**, *39*, 10935.

H. Liu, W. Yang, Y. Ma, Y. Cao, J. Yao, J. Zhang and T. Hu *Langmuir* **2003**, *19*, 3001-3005.

X. Lu, T. Hanrath, K. P. Johnston and B. A. Korgel *Nano Lett.* **2003**, *3*, 93-99.

W. D. Luedtke and U. Landman *J. Phys. Chem.* **1996**, *100*, 13323-13329.

J. J. Macklin, J. K. Trautman, T. D. Harris and L. E. Brus *Science* **1996**, *272*, 255-258.

S. Maenosono, C. D. Dushkin, S. Saita and Y. Yamaguchi *Langmuir* **1999**, *15*, 957-965.

T. Makimura, Y. Kunii, N. Ono and K. Murakami *Appl. Surf. Sci.* **1998**, *129*, 388-392.

S. Margel, S. Gura, H. Bamnolker, B. Nitzan, T. Tennenbaum, B. Bar-Toov, M. Hinz and H. Seliger *Scientific and Clinical Applications of Magnetic Carriers, Proceedings of the International Conference on Scientific and Clinical Applications of Magnetic Carriers, 1st, Rostock, Germany, Sept. 5-7, 1996* **1997**, 37-51.

M. D. Mason, G. M. Credo, K. D. Weston and S. K. Buratto *Phys. Rev. Lett.* **1998**, *80*, 5405-5408.

P. McCord, S. L. Yau and A. J. Bard *Science* **1992**, *257*, 68-69.

H. Miguez, F. Meseguer, C. Lopez, M. Holgado, G. Andreasen, A. Mifsud and V. Fornes *Langmuir* **2000**, *16*, 4405-4408.

D. C. Montgomery *Design and Analysis of Experiments*; 4th ed.; John Wiley & Sons, Inc.: New York, 1997.

A. M. Morales and C. M. Lieber *Science* **2000**, *279*, 5348.

C. B. Murray, C. R. Kagan and M. G. Bawendi *Annual Review of Materials Science* **2000**, *30*, Future.

N. Myung, Z. Ding and A. J. Bard *Nano Letters* **2002**, *2*, 1315-1319.

M. Nicodemi, A. Fierro and A. Coniglio *Europhysics Letters* **2002**, *60*, 684-690.

M. Nirmal and L. Brus *Accounts Chem. Res.* **1999**, *32*, 407-414.

M. Nirmal, B. O. Dabbousi, M. G. Bawendi, J. J. Macklin, J. K. Trautman, T. D. Harris and L. E. Brus *Nature* **1996**, *383*, 802-804.

D. J. Norris and Y. A. Vlasov *Advanced Materials* **2001**, *13*, 371-376.

T. Ogawa, Y. Kanemitsu and Editors *Optical Properties of Low-Dimensional Materials*, 1995.

P. C. Ohara, J. R. Heath and W. M. Gelbart *Angewandte Chemie-International Edition in English* **1997**, *36*, 1078-&.

P. C. Ohara, D. V. Leff, J. R. Heath and W. M. Gelbart *Phys. Rev. Lett.* **1995**, *75*, 3466-3469.

K. Ohata and T. Yoshihara In *Jpn. Kokai Tokkyo Koho*; (Toppan Printing Co., Ltd., Japan). Jp, 2002, p 9 pp.

A. A. Onischuk, A. I. Levykin, V. P. Strunin, M. A. Ushakova, R. I. Samoilova, K. K. Sabelfeld and V. N. Panfilov *Journal of Aerosol Science* **2000**, *31*, 879-906.

A. A. Onischuk and V. N. Panfilov *Uspekhi Khimii* **2001**, *70*, 368-381.

A. A. Onischuk, V. P. Strunin, M. A. Ushakova and V. N. Panfilov *Journal of Aerosol Science* **1997**, *28*, 207-222.

M. A. Otooni *Materials Research Society Symposium Proceedings* **1995**, *362*, 49-59.

F. Papadimitrakopoulos, P. Wisniecki and D. E. Bhagwagar *Chemistry of Materials* **1997**, *9*, 2928-2933.

B.-R. Paulke, N. Buske and S. Winoto-Morbach *Scientific and Clinical Applications of Magnetic Carriers, Proceedings of the International Conference on Scientific and Clinical Applications of Magnetic Carriers, 1st, Rostock, Germany, Sept. 5-7, 1996* **1997**, 69-76.

V. N. Paunov, P. A. Kralchevsky, N. D. Denkov and K. Nagayama *Journal of Colloid and Interface Science* **1993**, *157*, 100-112.

L. E. Pell "Quantum Confinement in Nanomaterials Explored Via Particle in a Box Theory," University of Texas at Austin, 2002.

L. E. Pell, Z. Yu, D. S. English, D. O'Connor, P. F. Barbara and B. A. Korgel In *Materials Research Society Symposium*; R. K. Singh, M. P. M., M. Senna and H. Hofmann, Eds.: Boston, MA, 2001; Vol. 704.

Z. A. Peng and X. G. Peng *Journal of the American Chemical Society* **2002**, *124*, 3343-3353.

Z. A. Peng and P. X. *Journal of the American Chemical Society* **2001**, *123*, 1389-1395.

J. T. Petkov, N. D. Denkov, K. D. Danov, O. D. Velev, R. Aust and F. Durst *Journal of Colloid and Interface Science* **1995**, *172*, 147-154.

A. P. Philipse *Colloids and Surfaces, A: Physicochemical and Engineering Aspects* **1993**, *80*, 203-210.

M. Pinnow, R. Wiacek and C. G. Willson, For fruitful discussions about silane chemistry.

T. M. Reith and J. D. Schick *Applied Physics Letters* **1974**, *25*, 524-526.

T. C. Richards and A. J. Bard *Anal. Chem.* **1995**, *67*, 3140-3147.

K. F. Roenigk, K. F. Jensen and R. W. Carr *J. Phys. Chem.* **1987**, *91*, 5732-5739.

G. Santa-Maria Blanco, G. Reglero Rada, J. Tabera Galvan, G. P. Blanch Manzano and J. Pastor Pastor In *Span.*; (Consejo Superior de Investigaciones Cientificas, Spain). Es, 2001, p 6 pp.

J. D. Saunderson and R. Swanepoel *Solar Energy Materials and Solar Cells* **1998**, *53*, 329-332.

P. E. Savage, S. Gopalan, T. I. Mizan, C. J. Martino and E. E. Brock *AIChE J.* **1995**, *41*, 1723-1778.

H. K. Schmidt *Macromolecular Symposia* **1996**, *101*, 333-342.

B. A. Scott, R. D. Estes and J. M. Jasinski *Journal of Chemical Physics* **1988**, *89*, 2544-2549.

P. S. Shah, J. D. Holmes, K. P. Johnston and B. A. Korgel *Journal of Physical Chemistry B* **2002**, *106*, 2545-2551.

P. S. Shah, S. Husain, K. P. Johnston and B. A. Korgel *Journal of Physical Chemistry B* **2001**, *105*, 9433-9440.

P. S. Shah, S. Husain, K. P. Johnston and B. A. Korgel *Journal of Physical Chemistry B* **2002**, *106*, 12178-12185.

M. Shim and P. Guyot-Sionnest *Nature* **2000**, *407*, 981-983.

K. T. Shimizu, R. G. Neuhausser, C. A. Leatherdale, S. A. Empedocles, W. K. Woo and M. G. Bawendi *Physical Review B* **2001**, *63*, 205316.

F. Slootman and J. C. Parent *Journal of Aerosol Science* **1994**, *25*, 15-21.

Sonics & Materials; *Ultrasonic Equipment for Sonochemistry*; http://www.sonicsandmaterials.com/Sonochemistry/sonochemistry.html; **2003**.

H. S. Sozuer, J. W. Haus and R. Inguva *Physical Review B* **1992**, *45*, 13962-13972.

J. L. Speier, Jr. and R. E. Zimmerman *Journal of the American Chemical Society* **1955**, *77*, 6395-6396.

M. L. Steigerwald and L. E. Brus *Annual Review of Materials Science* **1989**, *19*, 471-495.

C. Stowell and B. A. Korgel *Nano Letters* **2001**, *1*, 595-600.

S. H. Sun and C. B. Murray *J. Appl. Phys.* **1999**, *85*, 4325-4330.

K. S. Suslick, M. M. Fang and T. Hyeon *Journal of the American Chemical Society* **1996**, *118*, 11960-11961.

K. S. Suslick, T. W. Hyeon and M. M. Fang *Chemistry of Materials* **1996**, *8*, 2172-2179.

K. S. Suslick and G. J. Price *Annual Review of Materials Science* **1999**, *29*, 295-326.

M. T. Swihart and S. L. Girshick *Journal of Physical Chemistry B* **1999**, *103*, 64-76.

X. Tan, S. Huang, M. Zhou and M. Wang *Gongneng Cailiao Yu Qijian Xuebao* **1998**, *4*, 34-40.

Y. Tatsumi, M. Hirata and K. Yamada *Journal of the Physical Society of Japan* **1981**, *50*, 2288-2294.

U. Thiele, M. Mertig and W. Pompe *Physical Review Letters* **1998**, *80*, 2869-2872.

T. Trindade, P. O'Brien and N. L. Picket *Chemistry of Materials* **2001**, *13*, 3843-3858.

W. van Sark, P. Frederix, D. J. Van den Heuvel, H. C. Gerritsen, A. A. Bol, J. N. J. van Lingen, C. D. Donega and A. Meijerink *Journal of Physical Chemistry B* **2001**, *105*, 8281-8284.

O. D. Velev and E. W. Kaler *Advanced Materials* **2000**, *12*, 531-534.

O. D. Velev, P. M. Tessier, A. M. Lenhoff and E. W. Kaler *Nature* **1999**, *401*, 548-548.

K. P. Velikov, F. Durst and O. D. Velev *Langmuir* **1998**, *14*, 1148-1155.

Y. A. Vlasov, N. Yao and D. J. Norris *Advanced Materials* **1999**, *11*, 165-169.

T. Vossmeyer, L. Katsikas, M. Giersig, I. G. Popovic, K. Diesner, A. Chemseddine, A. Eychmuller and H. Weller *The Journal of Physical Chemistry* **1994**, *98*, 7665-7673.

S. P. Walch and C. E. Dateo *Journal of Physical Chemistry A* **2001**, *105*, 2015-2022.

C. J. Wang, M. Shim and P. Guyot-Sionnest *Science* **2001**, *291*, 2390-2392.

C.-y. Wang, C.-y. Liu, X. Zheng, J. Chen and T. Shen *Colloids and Surfaces, A: Physicochemical and Engineering Aspects* **1998**, *131*, 271-280.

L. Y. Wang, Y.-J. Lin and W.-Y. Chiu *Synthetic Metals* **2001**, *119*, 155-156.

S. Wang *Huaqiao Daxue Xuebao, Ziran Kexueban* **2002**, *23*, 129-132.

A. Watanabe, M. Unno, F. Hojo and T. Miwa *Journal of Materials Science Letters* **2001**, *20*, 491-493.

H. Weber, D. Marx and K. Binder *Physical Review B* **1995**, *51*, 14636-14651.

H. S. White and A. J. Bard *J. Am. Chem. Soc.* **1982**, *104*, 6891-6895.

J. P. Wilcoxon, G. A. Samara and P. N. Provencio *Phys. Rev. B* **1999**, *60*, 2704-2714.

D. B. Williams and C. B. Carter In *Transmission Electron Microscopy*; Plenum Press: New York, 1996; Vol. IV, pp 697-699.

D. L. Williamson, S. Roorda, M. Chicoine, R. Tabti, P. A. Stolk, S. Acco and F. W. Saris *Applied Physics Letters* **1995**, *67*, 226-228.

W. L. Wilson, P. F. Szajowski and L. E. Brus *Science* **1993**, *262*, 1242-1244.

M. V. Wolkin, J. Jorne, P. M. Fauchet, G. Allan and C. Delerue *Phys. Rev. Lett.* **1999**, *82*, 197-200.

M. Wu and S. Wagner *Applied Surface Science* **2001**, *175-176*, 753-758.

Y.-N. Xu and W. Y. Ching *Physical Review B* **1993**, *48*, 4335-4351.

E. Yablonovitch *Physical Review Letters* **1987**, *58*, 2059-2062.

M. Yamaki, J. Higo and K. Nagayama *Langmuir* **1995**, *11*, 2975-2978.

C.-S. Yang, R. A. Bley, S. M. Kauzlarich, H. W. H. Lee and G. R. Delgado *Journal of the American Chemical Society* **1999**, *121*, 5191-5195.

S. Yang *Zhongguo Zhongyao Zazhi* **2001**, *26*, 755-757.

Y.-H. Ye, T. S. Mayer, I.-C. Khoo, I. B. Divliansky, N. Abrams and T. E. Mallouk *Journal of Materials Chemistry* **2002**, *12*, 3637-3639.

A. P. Young *Physical Review B* **1979**, *19*, 1855-1866.

K. J. Ziegler, R. C. Doty, K. P. Johnston and B. A. Korgel *Journal of the American Chemical Society* **2001**, *123*, 7797-7803.

Vita

Lindsay Erin Pell, the only child of Robert and P. Kimberly Pell, was born May 17, 1976 near Annapolis, Maryland. After graduating from South River High School in 1994, she entered the Georgia Institute of Technology in Atlanta, Georgia. In June 1998 Lindsay graduate with High Honor with a Bachelor of Science in Chemical Engineering and a Certificate in Industrial/Organizational Psychology. Lindsay worked as an environmental engineer for Cytec Industries, Inc. until 1999 when she entered graduate school at the University of Texas at Austin in the Department of Chemical Engineering. She joined Brian Korgel's research group and spent four and half years researching the synthesis and characterization of silicon nanocrystals.

Permanent Address: 3444 South River Terrace; Edgewater, MD 21037

This dissertation was typed by the author.